Surface wave-induced Eulerian-mean flows in the open ocean

Christopher John Higgins

Keble College

University of Oxford

A thesis submitted for the degree of

Doctor of Philosophy

Michaelmas 2020

Abstract

This thesis examines Lagrangian-mean flows induced by surface gravity waves, with particular emphasis on the displacements associated with these flows. Stokes drift, the small Lagrangian-mean velocity accompanying the orbital motion of particles beneath surface waves, has been well-studied, and is proven to play a role in ocean transport. However, Eulerian-mean flows induced by slow variation of the wave field (divergence-driven), viscous effects, or geophysical effects such as density stratification and planetary rotation, have received less attention. It is the aim of this thesis to study these wave-induced Eulerian-mean flows, which must be superimposed on the Stokes drift to obtain the correct Lagrangian-mean (or mass transport) velocity induced by surface gravity waves. In Chapter 2, the effects of wave directional spread and density stratification on the mean flow induced by a surface gravity wavepacket in deep water are studied, and the corresponding displacements are derived. Chapter 3 examines 'Ekman–Stokes' dynamics driven by the Stokes drift and Coriolis force within the turbulent upper ocean boundary layer, and uses buoy data to explore the impact these dynamics have on the drift of a floating particle. Finally, in Chapter 4 I combine the insights of the two previous chapters to develop an analytical model capable of describing both divergence-driven and geophysically-driven Eulerian-mean flows induced by surface waves.

Acknowledgements

I am indebted to my DPhil supervisors, Prof. Ton van den Bremer and Prof. Jacques Vanneste, for their support, guidance, and encouragement throughout my DPhil. I would firstly like to acknowledge their contributions on a personal level. Over the course of my project, they have played an instrumental role in helping me to appreciate my own abilities and build self-confidence. During times of immense change or personal difficulty, such as the transfer from Edinburgh to Oxford or, more recently, the imposition of lockdown restrictions in Ireland, their support and understanding meant a great deal to me and helped me to bounce back. On an academic level, I would like to thank them particularly for their patience and enthusiasm. They encouraged my natural curiosity while also providing wisdom and guidance, so that I could poke my head into the occasional rabbit hole without falling into it, and learn something new in the process.

I'm extremely grateful to my dear friend Jorik Mol, without whom I might not have stayed the course. I would also like to thank my friends from Keble MCR for supporting me during rough times and being generally fabulous, and the 'Once Upon A...' group for the many memorable Hall meals, chats, poker and board games, pubs and parties. You all made me feel that I belong in Oxford and could thrive here. More recent thanks goes to Qu(-hear) Voices and the friends I've made there, for creating a wonderful and welcoming space in which I could share my scribbles.

In Edinburgh, special mention is reserved for my partner-in-crime Alan Price, and erstwhile housemates Fionn Ó' hÓgáin, Felix James-Kahn, and Eoin Ó'Laighléis. A special thanks goes to Gaye Cleary for tea and chat till the wee hours, and for letting me crash at her place when I was visiting for the week or between tenancies. I would like to thank my UCD friends for keeping in touch, and Prof. Frédéric Dias for sparking my interest in fluid mechanics and offering advice and references during my search for a PhD. They say that a mathematician is a machine to turn coffee into theorems, so it would also be amiss of me not to acknowledge all of my favourite coffee haunts in Edinburgh and in Oxford for keeping me caffeinated!

Of course, none of this would have been possible without the unwavering belief and support of my parents, grandparents, godmother, brothers and, during my time in Edinburgh, my friend Dara Beggan. Finally, I would like to thank Michał Pychtin: it started with a cup of tea and a summer storm.

Contents

List of Figures

Chapter 1
Introduction

1.1 Background

Though surface gravity waves are periodic, they induce higher-order mean flows which can influence the transport of tracers and particles such as plastics (Onink et al., 2019). As a fluid particle follows its periodic orbit beneath a regular periodic surface wave, it experiences a net drift in the direction of wave propagation known as the Stokes drift (Stokes, 1847). This small drift arises at second order in wave steepness $\alpha = (ak)$ with a the wave amplitude and k the wavenumber and decays rapidly with depth; for a plane periodic surface wave in deep water the Stokes drift $u_{\mathrm{S}} = c\alpha^2 \exp(2kz)$ where $c = \omega/k$ is the wave phase velocity and z the vertical coordinate measured upwards from the free surface. Despite being a nonlinear quantity, it may be computed from the linear ($O(\alpha)$) wave solutions. A suitable definition of the Stokes drift is that it is the difference between the Lagrangian and Eulerian velocities of the flow field,

$$\boldsymbol{u}_{\mathrm{L}} = \overline{\boldsymbol{u}} + \boldsymbol{u}_{\mathrm{S}}, \qquad \text{Lagrangian} = \text{Eulerian} + \text{Stokes}. \tag{1.1}$$

This quasi-Eulerian description was put on a more formal mathematical footing by Andrews and McIntyre (1978) in their work on generalised Lagrangian-mean

theory (GLM) (see Bühler (2014) for a review). The Lagrangian mean is computed as the average along the actual trajectory of a particle, such that

$$\overline{\phi}^{\mathrm{L}} = \overline{\phi\left(\boldsymbol{x}+\boldsymbol{\xi},t\right)} \approx \overline{\phi\left(\boldsymbol{x},t\right)} + \overline{\boldsymbol{\xi}\cdot\boldsymbol{\nabla}\phi\left(\boldsymbol{x},t\right)} = \overline{\phi} + \phi^{\mathrm{S}}, \tag{1.2}$$

where $\boldsymbol{x}$ is the (Eulerian) mean path of the particle and $\boldsymbol{\xi}$ represents fluctuations about this mean, with $\overline{\boldsymbol{\xi}} = \mathbf{0}$.

Though the effects of winds and currents on transport of marine litter in the open ocean are relatively well understood (see e.g. Onink et al., 2019), surface wave effects have only recently been incorporated into these studies. Stokes drift is important in the accurate prediction of near-surface drifter and buoy trajectories (see Röhrs et al., 2012) and indeed in the study of upper-ocean dynamics in general. Waves have been shown by Christensen and Terrile (2009) to play a significant role in the transport and spatial deformation of oil slicks and other surface contaminants, and the wave environment must be taken into account in search and rescue operations, such as in the MH370 plane crash in the Indian Ocean (Trinanes et al., 2016). More recently, there has been a growing interest in the influence of waves on floating marine litter, in particular plastics. Including the Stokes drift in such studies may help to capture seasonal variation in transport of floating litter: Iwasaki et al. (2017) found that in the Sea of Japan Stokes drift moves mesoplastics towards the Japanese coast, particularly during winter. Delandmeter and van Sebille (2019) and Onink et al. (2019) also found that Stokes drift pushed microplastics towards Arctic regions. Since concentrations of mesoplastics (5mm-25mm) and macroplastics ($>$ 25mm) drop off sharply with depth, but microplastics ($<$ 5mm) are found throughout the water column (Reisser et al., 2015), near-surface wind- and wave-induced flows will play a predominant role in the transport of these larger plastic fragments. In this way, waves may result in size-dependent differential transport by 'sorting' and displacing particles differently based on their size and buoyancy. Such size-dependent transport is likely to be important towards the coast, where larger plastics are broken down in the surfzone into microplastics (Laxague et al., 2018). Stokes drift also fundamentally changes transport patterns in the South Indian Ocean by

shifting the convergence regions to the west, causing leakage of plastics into the South Atlantic rather than the South Pacific, as demonstrated by Dobler et al. (2019) using the tracer advection equation. Waves may also allow particles to cross strong currents and circumpolar winds (Fraser et al., 2018).

Crucially the above studies have, for the most part, simply superimposed the Stokes drift obtained from measurements of the local wave field or from the output of a third-generation wave model such as WAM (The WAMDI Group, 1988) or WaveWatch III (Tolman, 2009) onto the Eulerian current field obtained from ocean general circulation models or observations. In doing so, they have ignored the fact that Eulerian flows can be generated and modified by surface waves. Wave-induced mean flows can form due to coastal boundaries and varying bathymetry (Elgar and Guza, 1985), spatial variation and mass divergence, and viscous and geophysical effects (Craik and Leibovich, 1976). I focus specifically on deep-water conditions, in which the water depth is much greater than the wavelength of the surface waves, in this thesis. Hence I consider only the latter two types of mean flows – those driven by spatial divergence, and those driven by viscous and geophysical effects.

1.2 Divergence-driven mean flows

Though Stokes derived the drift due to a plane monochromatic wave, realistic sea states consist of a spectrum of waves possessing different frequencies and directions of propagation. Kenyon (1969) showed how the classical expression for the Stokes drift could be extended to an ensemble of random waves. Such a linear superposition of waves with different frequencies and directions may equivalently be described in terms of wavepackets (or wave groups) (e.g. Kinsman, 2002). Since the Stokes drift depends on the square of the local wave amplitude, its magnitude varies from zero at the edges of a wavepacket to a maximum at the spatial peak, causing its associated mass transport to become horizontally divergent on the packet scale. Longuet-Higgins and Stewart (1962) demonstrated that this divergence drives an Eulerian-mean flow corresponding to the second-order frequency-difference terms formed from interaction between the underlying linear wave components which make

up the packet. While the Stokes drift transports particles forward at the surface, the wave-induced Eulerian flow returns them backwards at depth, and is hence also known as the Eulerian return flow. For surface wavepackets in infinitely deep water, the Lagrangian-mean mass transport found by superimposing the Stokes transport and mass transport by the return flow is zero (e.g. McIntyre, 1981). Recently, van den Bremer, Whittaker, et al. (2019) used wavemaker-generated wavepackets and particle tracking velocimetry to observe the return flow experimentally in a wave flume for the first time. Further details on Stokes drift and its interrelated phenomena, including return flows, may be found in the recent review by van den Bremer and Breivik (2017).

When the wave spectrum is sharply peaked about a single frequency/wavenumber, such that $\Delta k/k_p \ll 1$ where Δk is the characteristic width of the spectrum and k_p is its peak, it is possible to make a quasi-monochromatic (QM) approximation. Under this approximation the wavepacket may be treated as a single monochromatic wave modulated by slow envelope functions in space and time. This leads to simplified expressions for the Stokes drift — which retains its monochromatic form $c\left(|a(\boldsymbol{x},t)|k_p\right)^2\exp(2k_pz)$ — and the Eulerian return flow which depends on Δk, the small wavenumber difference. Exploiting the QM approximation, van den Bremer and Taylor (2015) and van den Bremer and Taylor (2016) applied the method of multiple scales to the return flow problem; effects such as amplitude dispersion appear at higher order in the multiple-scales bandwidth parameter $\varepsilon = \Delta k/k \ll 1$ (the leading-order effects of dispersion appear at $O(\varepsilon^2)$).

Though much of the literature surrounding return flows has concentrated on irrotational wave theory, the Earth's oceans are weakly density-stratified due to variations in salinity and temperature throughout the water column. It was noted by McIntyre (1981) that oceanic stratification would likely distort the structure of the return flow due to a group of waves. The potential for surface waves to interact with internal waves is explored in Olbers and Eden (2016), who described the generation of an internal wave by a pair of surface waves as a resonant triad interaction. Recently, Haney and Young (2017) examined whether a surface wavepacket and

its induced return flow may energetically interact with internal waves. While they conclude that groups of surface waves do not act as an appreciable source/sink of energy for internal waves, they confirm that the presence of stratification significantly alters the mean flow profile. A train of internal waves are always generated in the packet's wake by directionally-spread packets (referred to hereafter as 3D), but oceanic stratification is generally too weak to excite internal waves in 2D (the case of a spanwise-infinite wavepacket).

Mean flows due to surface wavepackets have also been explored by use of the cubic Nonlinear Schrödinger Equation (NLS) and its higher-order extensions. Davey and Stewartson (1974) extended the wavepacket problem to 3D and water of arbitrary depth by deriving a nonlinear Schrödinger (NLS)-type equation, which was later extended in the seminal paper by Dysthe (1979) to a modified nonlinear Schrödinger equation (MNLS), valid in deep water, describing the coupling between the return flow and free surface in deep water. Dysthe's MNLS has since formed the basis of many studies on stability of wave groups and emergence of freak waves (e.g. Taklo et al., 2017; Steer et al., 2020).

1.3 Geophysical and viscous effects

Longuet-Higgins (1953) included the effects of thin viscous boundary layers near the bottom and the free surface, showing that these have a considerable impact on the mass transport in the interior of the fluid. Depending on the ratio a/δ where a is the wave amplitude and δ is the thickness of the boundary layer, vorticity is eventually transported from the boundary layers into the fluid interior either by conduction ($a/\delta \ll 1$) or convection with the mass transport velocity ($a/\delta \gg 1$). For typical wave periods and the molecular viscosity of seawater, $\delta \sim O(\text{mm})$. Consequently, the conduction solution arises only for extremely small waves in very shallow wave flume settings (Groeneweg and Klopman, 1998). The convection solution is of interest for most realistic surface waves. Longuet-Higgins showed that when $a/\delta \gg 1$, the shear of the wave-induced Lagrangian flow at the base of the vorticity boundary layer is *twice* that of the Stokes drift. In other words, the shear of the Eulerian current is

equal to the shear of the Stokes drift near the surface. This 'virtual wave stress' corresponds to the momentum lost to the mean flow due to viscous damping of the waves. The wave stress condition remains the same for waves maintained at constant amplitude by e.g. wind or energy transfers between different wave frequencies which constantly replace the momentum lost by the waves. This wave stress boundary condition was disputed by Huang (1970), who pointed out that in water of infinite depth the surface value of the steady mass transport velocity becomes infinite, a result that became known as the 'Longuet-Higgins paradox' (Madsen, 1978). Huang then imposed without derivation the condition that the shear of the Eulerian current vanish at the free surface, and hence obtained a finite steady mass transport at the surface. However, using Lagrangian coordinates Ünlüata and Mei (1970) verified that Longuet-Higgins' boundary condition is indeed correct, and that the infinite value of velocity at the surface comes about by requiring a steady-state solution to exist in infinite depth. The Longuet-Higgins paradox was successfully resolved by Madsen (1978), who added the Coriolis force to the equations of motion. A steady state in infinite depth is then possible, since the viscous shear of the flow can be balanced by Earth's rotation. Xu and Bowen (1994) and Seshasayanan and Gallet (2019) have since rederived Longuet-Higgins' wave stress condition in Eulerian coordinates and studied the steady wave-driven currents which result from it.

In an inviscid ocean the Lagrangian drift induced by a periodic wave train must be zero in a rotating frame, as an unopposed Stokes drift violates the conservation of circulation (Ursell, 1950). It was later shown by Hasselmann (1970) that the Coriolis force puts the horizontal and vertical velocity components out of quadrature, inducing a stress on the Eulerian flow which acts perpendicular to wave propagation. This Coriolis–Stokes forcing (as coined by Polton et al., 2005) causes the Eulerian current to rotate with the inertial frequency and cancel the Stokes drift after a quarter pendulum-day, so that the Lagrangian current becomes an inertial oscillation and there is no net transport. In other words, the Coriolis–Stokes forcing drives an 'anti-Stokes' flow which cancels the Stokes drift, up to a free inertial oscillation which is a homogeneous solution to the momentum equations. An exact solution

for Gerstner waves in the presence of rotation was derived at about the same time by Pollard (1970), who found the Gerstner dispersion relation to be only slightly modified by rotation. A novel feature of his calculation is the inclusion of the 'nontraditional' horizontal component of the Coriolis vector; he showed that particles move in closed inertial orbits in a plane slightly tilted away from the vertical. The horizontal Coriolis component is widely neglected under the 'Traditional Approximation' (TA), usually on the basis that the horizontal scales of the motion are much larger than its vertical scale. As pointed out by Gerkema, Zimmerman, et al. (2008) this may not always be valid, particularly when the traditional Coriolis frequency f is small (at low latitudes near the Equator, for instance) or when vertical velocities are non-negligible. The nontraditional component also results in a modification to hydrostatic balance. Recently Thomas et al. (2018) considered the mean-flow response to a surface wavepacket in rotating shallow water, demonstrating that it consists of a superposition of a classic return flow and a rotation-driven anticyclonic flow. With increasing rotation the anticyclonic flow dominates, eventually confining the mean flow to the 'footprint' of the wavepacket and quenching the Lagrangian transport.

Turbulence in the upper ocean boundary layer can act in conjunction with Earth's rotation to create additional Eulerian-mean flows. Assuming the turbulence could be parametrised by a constant 'eddy viscosity', Ekman explained his PhD supervisor's observations of Arctic ice drifting at an angle to the right of the wind direction as a balance between the turbulent shear and Earth's rotation (Ekman, 1905). These Ekman currents form an important part of the wind-driven ocean circulation. Many attempts have been made to improve Ekman's classical theory by changing the parametrisation of the turbulent eddy viscosity or by adding wave effects. For example, angles of deflection between the wind direction and Ekman current at the surface are generally observed to be much less than the 45° predicted by Ekman's classical theory (Price and Sundermeyer, 1999). Madsen (1977) modelled the Ekman layer using an eddy viscosity which grows linearly in depth, which more accurately captures the logarithmic current profile observed near the surface and results in

smaller deflection angles of the surface Eulerian current. When the wind stress at the surface varies spatially, this gives rise to small vertical 'Ekman pumping' velocities, which in turn create zones of convergence (downwelling) or divergence (upwelling) of water masses and marine litter. Microplastic concentrations are generally higher in regions of convergence and lower in regions of divergence (Onink et al., 2019). Other authors (Xu and Bowen, 1994; Lewis and Belcher, 2004; Polton et al., 2005) have added the Coriolis-Stokes forcing to Ekman calculations, finding that it influences the current profile and mass transport throughout the Ekman depth $\propto \sqrt{\nu/f}$. The induced current contains an 'anti-Stokes' flow which only partially cancels the Stokes drift, in contrast with the inviscid case in which exact cancellation occurs (Polton et al., 2005). Although the Coriolis-Stokes forcing is increasingly included in Ekman calculations and circulation models, the wave stress at the surface has received less attention. Authors such as Madsen (1978), Xu and Bowen (1994), and Seshasayanan and Gallet (2019) have pointed out that the wave stress is often comparable in magnitude to the wind stress and can drive 'Ekman-Stokes' spirals.

Waves also affect upper-ocean dynamics through the so-called Stokes forces (Craik and Leibovich, 1976; Suzuki and Fox-Kemper, 2016). The Stokes drift velocity profile interacts with the wave-induced and background (non-wave) Eulerian-mean flow through shear and vortex forces to give rise to Langmuir circulations through the so-called Craik-Leibovich instabilities (Craik and Leibovich, 1976; Huang, 1979). In this way, surface waves play a potentially important role in upper-ocean mixing, and indirectly influence the value of turbulent eddy viscosity through the high-frequency portion of the wave spectrum.

1.4 Synopsis

The main body of this thesis consists of three main parts: the influence of directional spread and stratification on the mean flow by surface wavepackets (chapter 2), wave-driven Ekman-Stokes dynamics (chapter 3), and Ekman-Stokes pumping (chapter 4). Chapter 2 is subdivided into two sections, the first examining the influence of wave directional spread and the second examining the influence of density stratification.

Throughout, I make use of perturbation methods and asymptotic techniques to simplify the nonlinear governing equations and boundary conditions. I assume that the waves are of limited (small) steepness, so that we may use a Stokes expansion to separate the linear motions from the mean flow.

My aim is to develop a better understanding of the significance of wave-induced mean flows in both wave and circulation models, and hence their importance in particle transport. I neglect surface tension since our interest is in surface gravity waves typical of fully-developed wind seas or swell.

Nonlinear effects (in amplitude) which are above the order of the wave-induced mean flow are neglected, and so this thesis does not consider the instability of the wave train through interaction with the induced mean flow. The Craik–Leibovich instabilities which rely on the vorticity of the Stokes drift are important in some conditions (Craik and Leibovich, 1976), but do not arise in the scenarios we consider.

1.4.1 Chapter 2

This chapter is based on a paper entitled 'Lagrangian transport by surface gravity wavepackets: effects of directional spread and stratification' co-authored by T. S. van den Bremer and J. Vanneste, and published in the Journal of Fluid Mechanics (Higgins, van den Bremer, et al., 2020)

This chapter deals with the Eulerian-mean return flow driven by the divergence of the Stokes mass transport caused by idealised wavepackets, and the net displacements associated with this return flow. The return flow and its associated displacements are examined for the case of an isolated wavepacket, first on an unstratified ocean and then on a stratified ocean. Considering the net displacement over long times yields some surprising results: the Eulerian-mean displacement vanishes for a 3D wavepacket (directionally-spread, hence finite in the cross-wave direction) but it is negative and constant in depth for a 2D packet (unidirectional or spanwise-infinite, hence periodic in the cross-wave direction). However, the 3D displacement over finite time intervals is finite and nonzero: initially, the displacement behaves as in the 2D case, but ultimately decreases to zero as the flow

becomes 3D and begins to return around the directionally-spread packet as well as beneath it. In the stratified case, the Fourier-integral approach I use is an alternative to the mode expansions of Haney and Young (2017). Net displacements are again zero in 3D, but oscillatory with depth in 2D. The behaviour and development of the 3D displacement over time depends on the strength of the stratification and the width of the packet.

I also examine the leading-order ($O(\varepsilon^2)$) effects of amplitude dispersion on the displacement, and the influence of the set-down of the mean surface on the net displacement.

1.4.2 Chapter 3

*This chapter is based on a paper published in Geophysical Research Letters entitled '**Unsteady Ekman–Stokes dynamics: implications for surface-wave induced drift of floating marine litter**' co-authored by J. Vanneste and T. S. van den Bremer (Higgins, Vanneste, et al., 2020)*

In this chapter I examine the surface gravity wave-induced Eulerian-mean 'Ekman–Stokes' flow which arises due to two main geophysical effects: the rotation of the Earth and the turbulence in the upper-ocean boundary layer, the latter of which can be related to the shear of the Eulerian-mean flow via an eddy viscosity. As demonstrated by Longuet-Higgins (1953) and recent laboratory experiments by Grue and Kolaas (2017), the O(mm)-thick viscous boundary near the free surface gives rise to a wave stress, which is related to the vertical shear of the Stokes drift. In turn this wave stress drives an Eulerian-mean Ekman–Stokes flow, which is affected by Earth's rotation, the Coriolis–Stokes forcing, and the upper-layer eddy viscosity. I show that the Ekman–Stokes flow is given by a convolution between the time-varying surface Stokes drift field and an 'Ekman–Stokes kernel' which encodes the development of the Ekman–Stokes flow with depth. Using the convolution, I compute the Eulerian-mean response to an idealised storm, and then to the Stokes drift field computed from CDIP buoy data. Accounting for the Ekman–Stokes flow

leads to differences in both magnitude and direction of the wave-induced Lagrangian current, and to predictions of wave-induced drift of floating marine litter.

1.4.3 Chapter 4

Chapter 4 incorporates the previous two chapters into a model which examines and links both the divergence-driven return flow and geophysically-driven Ekman–Stokes effects. When the wave field is spatially-varying, the Ekman–Stokes dynamics in the upper layer give rise to a weak vertical velocity. Analogously to how spatially-varying wind stress gives rise to regions of Ekman upwelling and downwelling, the weak wave-induced vertical velocity resulting from a spatially-varying wave field gives rise to Ekman–Stokes pumping. At the base of the upper layer the pumping velocity is given by the horizontal divergence of the leading-order wave-induced Lagrangian mass transport, and provides a modified boundary condition on the divergence-driven deep return flow. I examine the behaviour of the return flow in several physical limits.

Chapter 2
Directional spread and stratification

Abstract

The Lagrangian mass transport by non-dissipating surface gravity wavepackets consists of the Stokes drift and the wave-induced return flow. We examine how directional spreading and density stratification affect this mass transport for an isolated nondissipating wavepacket in deep water using a perturbation expansion. For an unstratified ocean, we show that the net displacement by the return flow is finite, negative, the same at all vertical levels and inversely proportional to the depth for spanwise-infinite packets representing unidirectional (2D) seas, but zero for spanwise-localised packets representing directionally-spread seas (3D). We resolve this 2D-3D difference by demonstrating that a transition between 2D-like (finite) and 3D-like (zero) displacement occurs on a time scale inversely proportional to the degree of directional spreading. For a stratified ocean, we show that in 2D the net displacement profile by the return flow oscillates slowly with depth, with a wavelength dependent on the ratio of buoyancy frequency to the surface wave group velocity, and infinite displacements are predicted when the surface wavepacket resonantly excites internal waves. In 3D, the net displacement remains zero in the presence of stratification, but finite-time displacements may be appreciably altered.

2.1 Introduction

The periodic motion of particles beneath surface gravity waves is subject to a small Lagrangian-mean velocity in the direction of wave propagation, a phenomenon known as Stokes drift (Stokes, 1847). In the ocean, this net motion provides a significant contribution to the trajectories of drifters (Röhrs et al., 2012), and must be accounted for in search and recovery missions such as for the 2014 MH370 airplane crash in the Indian Ocean (Trinanes et al., 2016). Stokes drift can be key in the local modelling of oil spills (Christensen and Terrile, 2009; Drivdal et al., 2014; Jones et al., 2016) and plays a potentially important yet largely unexplored role in the near-surface mass transport and dispersion of plastic pollution (e.g. Lebreton, Slat, et al., 2018).

Realistic sea states do not consist of regular waves but are made up from wavepackets (Longuet-Higgins, 1984), a feature which is equivalent to a linear superposition of waves with different wavenumbers and frequencies. Since Stokes drift depends on the square of the local wave amplitude, its associated mass transport becomes horizontally divergent on the packet scale. Longuet-Higgins and Stewart (1962) demonstrated that a deep return flow forms in response to this divergence. The total Lagrangian velocity is given by the sum of the Stokes drift and the induced return flow ($\boldsymbol{u}_{\mathrm{L}} = \boldsymbol{u}_2 + \boldsymbol{u}_{\mathrm{S}}$, e.g. Bühler, 2014). For surface wavepackets in infinitely deep water, the Lagrangian-mean mass transport is zero (e.g. McIntyre, 1980). The Stokes drift is localised near the surface while the return flow is more persistent with depth, so that packets induce a depth-dependent mass transport (e.g. van den Bremer and Taylor, 2016). Due to directional spreading of the underlying wave spectrum about a peak wavenumber, wavepackets frequently exhibit localisation in the spanwise direction, which may considerably reduce the magnitude of the return flow and its associated displacement (e.g. van den Bremer and Taylor, 2015). Recently, Haney and Young (2017) examined the propagation of a wavepacket on a stratified ocean, showing that density stratification significantly distorts the return flow.

In this paper, we investigate the Lagrangian transport associated with an isolated spanwise-localised (or 3D) non-dissipating surface gravity wavepacket, considering unstratified and stratified oceans in turn, and focussing on the net displacements induced by the return flow. We emphasise that the model of an isolated wavepacket we consider is mainly of theoretical interest and not directly applicable to the real ocean. It is intended to provide general insight into subtle features of the displacements and potentially provide a benchmark against which to test the codes of more realistic sea-state models.

We assume throughout that directional spreading is relatively weak, so that the packet's width is greater than or equal to its length in the direction of propagation. We examine wavetrains which are quasi-monochromatic, that is, with narrow-banded spectra. We also assume the surface waves have wavelengths much smaller than the water depth (i.e. are deep-water waves). We do not place such a restriction on the packet's characteristic length scale relative to the depth, and thus on the scale of the return flow. For an unstratified ocean, we use perturbation methods to demonstrate that the net displacement of particles by the return flow is finite and depth-independent for a spanwise-infinite wavepacket (2D), but vanishes altogether for a spanwise-localised (3D) packet. In doing so, we correct erroneous numerical predictions by van den Bremer and Taylor (2016) of more complex 2D displacement profiles and by van den Bremer and Taylor (2015) of small yet non-zero displacements in 3D. We resolve this contrast between 2D and 3D by exploring displacements over finite time intervals. While displacement underneath a 3D wavepacket is initially 2D-like (increasing in magnitude), an opposing part of the return flow brings a particle back to its original position at later times. This opposing part of the flow forms only in 3D, when the flow may return around as well as beneath the packet. Reversal of the particle displacement occurs at a time that is proportional to the packet's width, hence much later for almost-2D packets.

For a stratified ocean, we show that the net displacement profile by the return flow is a slowly oscillatory function of depth in 2D, with a wavelength depending on the ratio of buoyancy frequency N to the surface wave group velocity c_g.

Large net displacements are predicted when the wavenumber N/c_g is close to an integer multiple of π/d (where d is the ocean depth), corresponding to an exact resonance between c_g and the phase velocity of an internal wave with zero horizontal wavenumber. In 3D, the net displacement remains zero even in the presence of stratification.

This paper is laid out as follows. First, §2.2 examines the unstratified case, distinguishing net displacement in 2D (§2.2.2), 3D (§2.2.3), and studying the transition between them over finite times (§2.2.4). Second, §2.3 addresses the stratified case. We examine the implications of our results in §2.4 and draw conclusions. Appendix .1 explores the influence of the second-order set-down of the free surface on net displacement, and appendix .2 considers the otherwise neglected impact of leading-order wave dispersion.

2.2 Unstratified flow

2.2.1 Governing equations

We begin by considering the unstratified case. A three-dimensional body of water of depth d and infinite lateral extent is assumed, with Cartesian coordinates (x,y,z), where x and y are the horizontal coordinates, and z the vertical coordinate measured from the undisturbed water level upwards. Inviscid, incompressible and irrotational flow is assumed; hence the velocity can be written as the gradient of the velocity potential $\boldsymbol{u} = \boldsymbol{\nabla}\phi$. In addition to the no-flow condition at the bottom ($\partial_z\phi = 0$ at $z = -d$), the governing equation in the fluid interior (Laplace) and the kinematic and dynamic boundary conditions are

$$\left(\partial_x^2 + \partial_y^2 + \partial_z^2\right)\phi = 0, \quad \partial_z\phi\,|_{z=h} = \partial_t h + \boldsymbol{\nabla}_{\mathrm{H}}\phi|_{z=h}\cdot\boldsymbol{\nabla}_{\mathrm{H}}h, \quad \partial_t\phi|_{z=h} + gh + \frac{1}{2}|\boldsymbol{\nabla}\phi|^2\,|_{z=h} = 0, \tag{2.1a,b,c}$$

where the free surface elevation is denoted by $z = h(x, y, t)$, g is acceleration due to gravity, and $\boldsymbol{\nabla}_{\mathrm{H}} \equiv (\partial_x, \partial_y, 0)$ is the horizontal gradient.

The wave amplitude is assumed small: $\alpha \equiv a_0 k_0 \ll 1$, where a_0 is the peak amplitude of the surface elevation and k_0 the wavenumber of the carrier wave. We

solve the set (2.1) using a Stokes expansion and consider the first two orders, so that $\phi = \phi_1 + \phi_2 + ...$ and $h = h_1 + h_2 + ...$, with the subscript denoting the order in α.

First-order solutions: $O(\alpha)$

We assume that the ocean is deep with respect to the waves ($k_0 d \gg 1$), and that the packet is quasi-monochromatic, weakly localised in the x and y directions, and propagates along the x-axis, so that the first-order solution takes the form

$$h_1 = \mathrm{Re}\left[A_0(\varepsilon\tilde{x}, \varepsilon R y, \varepsilon^2 t) e^{i\theta(x,t)}\right] + O(\alpha\varepsilon), \tag{2.2a}$$

$$\phi_1 = \mathrm{Re}\left[-\frac{i\omega_0}{k_0} A_0(\varepsilon\tilde{x}, \varepsilon R y, \varepsilon^2 t) e^{i\theta(x,t)} e^{k_0 z}\right] + O(\alpha\varepsilon), \tag{2.2b}$$

where $\theta = k_0 x - \omega_0 t$ with $\omega_0 = \sqrt{g k_0}$ the angular frequency, and $\tilde{x} \equiv x - c_g t$ is the coordinate in a frame moving at the group velocity $c_g = \omega_0/(2k_0)$. The amplitude scale a_0 is taken as the envelope maximum, $\sup|A_0|$. Wavepacket scales are captured by the bandwidth parameter $\varepsilon \equiv (2k_0\sigma_x)^{-1} \ll 1$ and aspect ratio $R \equiv \sigma_x/\sigma_y$, where σ_x and σ_y are the characteristic packet scales in x (length) and in y (width), respectively. The limit $\varepsilon \to 0$ at fixed R recovers the case of a periodic wave. Throughout this paper, we consider only $0 \leq R \leq 1$, so that packets are never longer than they are wide; a 2D packet corresponds to $R = 0$ and a round packet to $R = 1$. The $O(\alpha\varepsilon)$ terms in (2.2a,b) are not needed to compute the leading-order wave-induced forcing, but must be examined when assessing effects of wave dispersion arising on a timescale $\varepsilon^2 t = O(1)$ (see appendix .2).

The Stokes drift is a wave property in the standard sense that it can be calculated directly from the linear solutions (2.2) as

$$\boldsymbol{u}_\mathrm{S} = \overline{\boldsymbol{\Delta x}_1 \cdot \boldsymbol{\nabla} \boldsymbol{u}_1} = k_0 \left(\omega_0 |A_0|^2, 0, -\frac{3}{2}\varepsilon c_g \partial_{\tilde{x}} |A_0|^2\right) e^{2k_0 z} + O(\alpha^2\varepsilon^2), \tag{2.3}$$

where the overbar represents an average over the wave phase, and $\boldsymbol{\Delta x}_1 = \int \boldsymbol{u}_1 dt$.

Second-order solutions: $O(\alpha^2)$

The return flow is found by solving the wave-averaged governing equations at second order in steepness. Expanding (2.1b,c) about the undisturbed level $z = 0$

up to quadratic terms and wave-averaging yields forcing equations for the Eulerian-mean flow and wave-averaged free surface (cf. Longuet-Higgins and Stewart, 1962; McAllister et al., 2018),

$$\left(\frac{1}{g}\partial_t^2+\partial_z\right)\phi_2=\boldsymbol{\nabla}_{\mathrm{H}}\cdot\overline{(\boldsymbol{u}_1h_1)}-\overline{\frac{1}{g}\partial_t\left(h_1\partial_{tz}\phi_1+\frac{1}{2}|\boldsymbol{\nabla}\phi_1|^2\right)}\quad\Big|_{z=0}, \tag{2.4}$$

$$h_2=-\frac{1}{g}\left(\partial_t\phi_2+\overline{\left(h_1\partial_{tz}\phi_1+\frac{1}{2}|\boldsymbol{\nabla}\phi_1|^2\right)}\right)\quad\Big|_{z=0}, \tag{2.5}$$

where we focus on mean quantities only. The $\partial_t h_2$ term in (2.1b) has been eliminated using ∂_t(2.1c). The first term on the right of (2.4) is the forcing due to the horizontal divergence of the transport associated with the waves. In the Eulerian-mean description used here, the transport is confined to the layer $-h\le z\le h$ spanning from the troughs to the crests of the waves, and is given by $\overline{\boldsymbol{u}_1h_1}=\boldsymbol{M}$, say, to leading order. In the Lagrangian-mean description it is distributed over a deeper layer of depth $\sim k_0^{-1}$ as the Stokes drift, again to leading order. Thus

$$\boldsymbol{M}\equiv\overline{(\boldsymbol{u}_1h_1)}=\int_{-d}^{0}\boldsymbol{u}_{\mathrm{S}}dz. \tag{2.6}$$

We refer to $\boldsymbol{M}$ in this paper as the Stokes transport. The second term on the right-hand side of (2.4) can be understood as the effect of the set-down of the wave-averaged free surface h_2 on the return flow. In deep water ($k_0d\gg1$), this set-down does not contribute to the forcing of the return flow to leading order, because the linear polarisation relationships for deep-water waves imply that

$$\overline{\left(h_1\partial_{tz}\phi_1+\frac{1}{2}|\boldsymbol{\nabla}\phi_1|^2\right)}=0\qquad\text{at } z=0, \tag{2.7}$$

to leading order, as can be seen by substitution from (2.2) after setting $\varepsilon=0$. Furthermore, the double time-derivative on the left of (2.4) can be ignored when $k_0d\gg1$, so the return flow arises solely from the divergence of the Stokes transport (a rigid-lid approximation, see also the discussion in appendix .1). Equation (2.4) then simplifies to

$$\partial_z\phi_2\left(\tilde{x},y,0\right)=\partial_{\tilde{x}}M+O\left(\alpha^2\varepsilon^2\right), \tag{2.8}$$

where M is the x-component of $\boldsymbol{M}$.

2.2.2 Unstratified flow in 2D

For two-dimensional flows induced by spanwise-infinite wavepackets, we make use of the streamfunction ψ_2, implicitly defined by $\boldsymbol{u}_2 = \boldsymbol{\nabla} \times (\psi_2 \hat{\boldsymbol{y}})$ and satisfying a Laplace boundary-value problem. The surface value of the streamfunction is the Stokes transport, and the ocean floor is a streamline:

$$\left(\partial_{\tilde{x}}^2 + \partial_z^2\right) \psi_2 = 0, \qquad \psi_2\left(\tilde{x}, 0\right) = M, \qquad \psi_2\left(\tilde{x}, -d\right) = 0. \tag{2.9a,b,c}$$

We are interested in the net (or long-time) displacement by the return flow, defined at any fixed value of x by

$$\Delta x = \int_{-\infty}^{\infty} u_2 dt = \frac{1}{c_g} \int_{-\infty}^{\infty} u_2 d\tilde{x}, \tag{2.10}$$

where the second equality makes use of the translating reference frame of the packet. We can compute the net displacement (2.10) without explicitly evaluating ψ_2. First, we integrate (2.9) over all $\tilde{x}$, noting that the vertical velocity $\partial_{\tilde{x}}\psi_2$ is zero at infinity, which reduces (2.9a) to the ordinary differential equation

$$\frac{d^2}{dz^2} \int_{-\infty}^{\infty} \psi_2 d\tilde{x} = 0, \quad \text{with} \quad \int_{-\infty}^{\infty} \psi_2 d\tilde{x} \bigg|_{z=0} = \int_{-\infty}^{\infty} M d\tilde{x}, \qquad \int_{-\infty}^{\infty} \psi_2 d\tilde{x} \bigg|_{z=-d} = 0, \tag{2.11a,b,c}$$

as boundary conditions. The solution is

$$\int_{-\infty}^{\infty} \psi_2\left(\tilde{x}, z\right) d\tilde{x} = \left(\frac{z+d}{d}\right) \int_{-\infty}^{\infty} M d\tilde{x}, \tag{2.12}$$

and the net displacement is deduced by dividing by c_g and taking the negative z-derivative (using (2.10) and $u_2 = -\partial_z \psi_2$),

$$\Delta x = -\frac{1}{c_g} \partial_z \int_{-\infty}^{\infty} \psi_2\left(\tilde{x}, z\right) d\tilde{x} = -\frac{1}{c_g d} \int_{-\infty}^{\infty} M d\tilde{x}. \tag{2.13}$$

We thus obtain the perhaps surprising result that the net displacement by the return flow is independent of depth. The displacement is finite and negative, unless the ocean depth is truly infinite (not just $k_0 d \gg 1$), when it goes to zero. Note that (2.13) is valid for any narrow-banded, unidirectional Stokes transport M.

The net Lagrangian displacement $\Delta x_{\mathrm{L}} \equiv \Delta x + \Delta x_{\mathrm{S}}$ *is* depth-dependent, and is obtained by integrating (2.3) with respect to time and adding to (2.13),

$$\Delta x_{\mathrm{L}} = \frac{\alpha^2\sqrt{\pi}}{k_0}\left(2k_0\sigma_x e^{2k_0 z} - \frac{\sigma_x}{d}\right), \tag{2.14}$$

where we have assumed a Gaussian packet $A_0 = a_0 \exp\left(-\tilde{x}^2/(2\sigma_x^2)\right)$, resulting in the Stokes transport $M = \omega_0 a_0^2 \exp\left(-\tilde{x}^2/\sigma_x^2\right)/2$, and $\alpha = a_0 k_0$ denotes wave steepness, as before. Lagrangian particles are displaced forwards above a certain depth and rearwards beneath it. Depth-integrating (2.14) from $-d$ to 0 gives the total volume transported by the Lagrangian flow, which vanishes in the limit $k_0 d \gg 1$ considered here. Whenever we assume Gaussian packets, displacements scaled by $\alpha^2\sqrt{\pi}/k_0$ will be denoted by a star,

$$\Delta x^* \equiv k_0\Delta x/(\alpha^2\sqrt{\pi}), \qquad \Delta x_{\mathrm{S}}^* \equiv k_0\Delta x_{\mathrm{S}}/(\alpha^2\sqrt{\pi}), \qquad \Delta x_{\mathrm{L}}^* \equiv k_0\Delta x_{\mathrm{L}}/(\alpha^2\sqrt{\pi}), \tag{2.15a,b,c}$$

so that $\Delta x^* = -1/d^*$ with $d^* = d/\sigma_x$.

2.2.3 Unstratified flow in 3D

In 3D, we evaluate the net displacement in two different ways. First, we use a double Fourier transform in $\tilde{x}$ and y to obtain the potential

$$\phi_2(\tilde{x}, y, z) = \frac{1}{4\pi^2}\,\mathrm{Re}\iint_{\mathbb{R}^2} \frac{ik\hat{M}}{\sqrt{k^2+l^2}} \frac{\cosh((z+d)\sqrt{k^2+l^2})}{\sinh(d\sqrt{k^2+l^2})} e^{ik\tilde{x}} e^{ily}\,dk\,dl, \tag{2.16}$$

where $\hat{M}(k,l)$ is the Fourier transform of $M(\tilde{x}, y)$. To find the net displacement, we take the x-derivative of (2.16) to obtain u_2 and integrate over all time (here $\tilde{x}$), resulting in a delta-function in k. This forces the integral to evaluate to zero (unless $l = 0$):

$$\Delta x = -\frac{1}{2\pi c_g}\,\mathrm{Re}\iint_{\mathbb{R}^2} \delta(k) \frac{k^2\hat{M}}{\sqrt{k^2+l^2}} \frac{\cosh((z+d)\sqrt{k^2+l^2})}{\sinh(d\sqrt{k^2+l^2})} e^{ily}\,dk\,dl = 0. \tag{2.17}$$

This result is in stark contrast with the negative, depth-independent net displacement in 2D (2.13). Second, we can also obtain this result from irrotationality of the return flow,

$$\partial_y w_2 = \partial_z v_2, \qquad \partial_z u_2 = \partial_x w_2, \qquad \partial_y u_2 = \partial_x v_2. \tag{2.18a,b,c}$$

Integrating (2.18b,c) over all time (equivalently, $\tilde{x}$), and assuming the velocity components v_2 and w_2 decay far from the packet ($|\tilde{x}| \to \infty$), we obtain the conditions

$$\partial_z \Delta x = 0, \qquad \partial_y \Delta x = 0, \tag{2.19a,b}$$

which together imply the net displacement Δx is at most a constant. As we also require the flow to decay as $|y| \to \infty$, we immediately obtain the result that $\Delta x = 0$.

Physical insight into this 2D-3D contrast may be obtained from mass balance arguments. Depth-integrating the incompressibility condition ($\boldsymbol{\nabla} \cdot \boldsymbol{u}_2 = 0$), and using (2.6) and (2.8), we obtain in 3D

$$\partial_{\tilde{x}} \int_{-d}^{0} (u_2 + u_{\mathrm{S}})\, dz = -\partial_y \int_{-d}^{0} v_2 dz, \tag{2.20}$$

where we have also used the boundary condition for w_2 at the bottom and rewritten M as the vertical integral of the Stokes drift, as in (2.6). Thus at each time t, the divergence of the Lagrangian transport in the propagation direction is counterbalanced by a gradient of transport in the y direction. In fact, the yz-area integral of the Lagrangian velocity is zero at each t, which may be seen by y-integrating (2.20) and again noting the decay at large $|\tilde{x}|$ and $|y|$. Despite the net return-flow displacement Δx being zero at any point, its yz-area integral must balance the yz-area integral of the Stokes drift displacement, which is nonzero since the Stokes drift is depth-limited and inherits the envelope decay of the packet, decaying rapidly in both y and z. Mathematically, the time and area integrals do not commute – to put it more starkly, $\int\int \Delta x dy dz$ is essentially zero times infinity, hence undefined. This result is independent of the functional form of M. We will now explore displacements over finite time intervals.

2.2.4 Finite-time displacement and the 2D-3D transition

We define the symmetric finite-time return-flow displacement (finite-time displacement, for brevity) as the following symmetric time integral evaluated at $x = y = 0$ over the time interval $[-t_{\mathrm{I}}, t_{\mathrm{I}}]$:

$$\Delta x\,(t_{\mathrm{I}}, z, d) = \int_{-t_{\mathrm{I}}}^{t_{\mathrm{I}}} u_2 dt = \frac{1}{c_g} \int_{-c_g t_{\mathrm{I}}}^{c_g t_{\mathrm{I}}} u_2 d\tilde{x}, \tag{2.21}$$

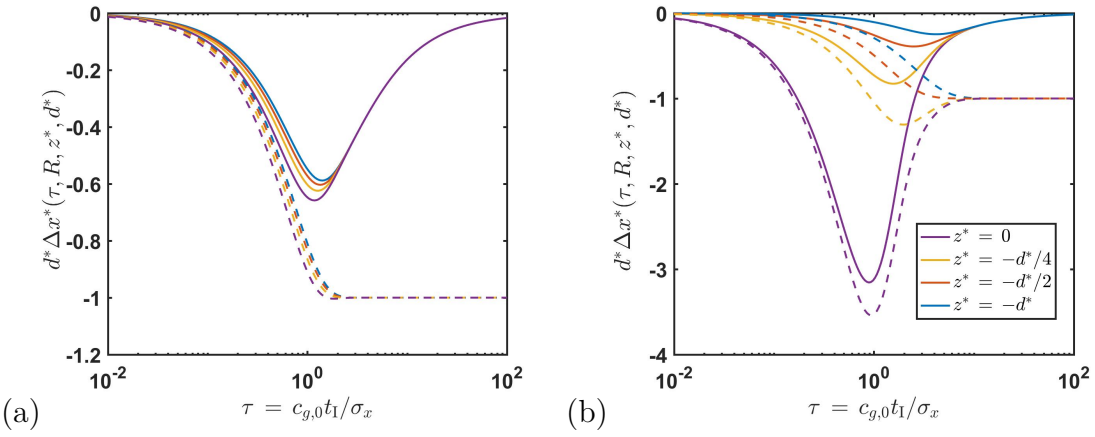

Figure 2.1: Scaled finite-time displacement at various depths, obtained from numerical integration of (2.23). Solid lines correspond to a 3D flow with $R = \sigma_x/\sigma_y = 1/3$, and the dashed lines to a 2D flow ($R = 0$). Panel (a) shows the displacement for a shallower return flow ($d^* = 0.5$, on the left), and panel (b) for a deeper return flow ($d^* = 5$, on the right).

thereby examining a particle underneath the centre of the packet at $t = 0$. We display the arguments (t_I, z, d) on the left of (2.21) to distinguish the finite-time displacement from its long-time limit, denoted as before by Δx without arguments. Recall that the long-time limit Δx has no z-dependence, either in 3D when it is zero at each (y, z), or in 2D when it is a nonzero constant. In this section we choose the Stokes transport M, and thereby its Fourier transform $\hat{M}$, to be Gaussian,

$$M = \frac{\omega_0 a_0^2}{2} e^{-\tilde{x}^2/\sigma_x^2} e^{-y^2/\sigma_y^2}, \qquad \hat{M} = \frac{\omega_0 a_0^2 \sigma_x \sigma_y \pi}{2} e^{-k^2\sigma_x^2/4} e^{-l^2\sigma_y^2/4}. \tag{2.22a,b}$$

Differentiating (2.16) with respect to $\tilde{x}$ to obtain u_2 and integrating as in (2.21), we obtain after moving to the nondimensional variables $\mu \equiv kc_g t_\mathrm{I}$ and $\lambda \equiv l\sigma_y$,

$$\Delta x^*(\tau, z^*, R, d^*) = \frac{-1}{2\pi^{3/2}\tau} \operatorname{Re} \iint_{\mathbb{R}^2} \frac{\mu \sin(\mu)}{\sqrt{\mu^2 + (R\tau)^2\lambda^2}} e^{-\mu^2/(4\tau^2)} e^{-\lambda^2/4} \times \frac{\cosh\left((z^* + d^*)\sqrt{\mu^2 + (R\tau)^2\lambda^2}/\tau\right)}{\sinh\left(d^*\sqrt{\mu^2 + (R\tau)^2\lambda^2}/\tau\right)} d\mu d\lambda, \tag{2.23}$$

where we have replaced z by $z^* \equiv z/\sigma_x$, d by $d^* \equiv d/\sigma_x$, and t_I by $\tau \equiv c_g t_\mathrm{I}/\sigma_x$, i.e., the half-interval t_I scaled by the packet translation time σ_x/c_g. As before, the aspect ratio $R \equiv \sigma_x/\sigma_y$ so that $R \to 0$ corresponds to 2D; and Δx^* is scaled as in (2.15a).

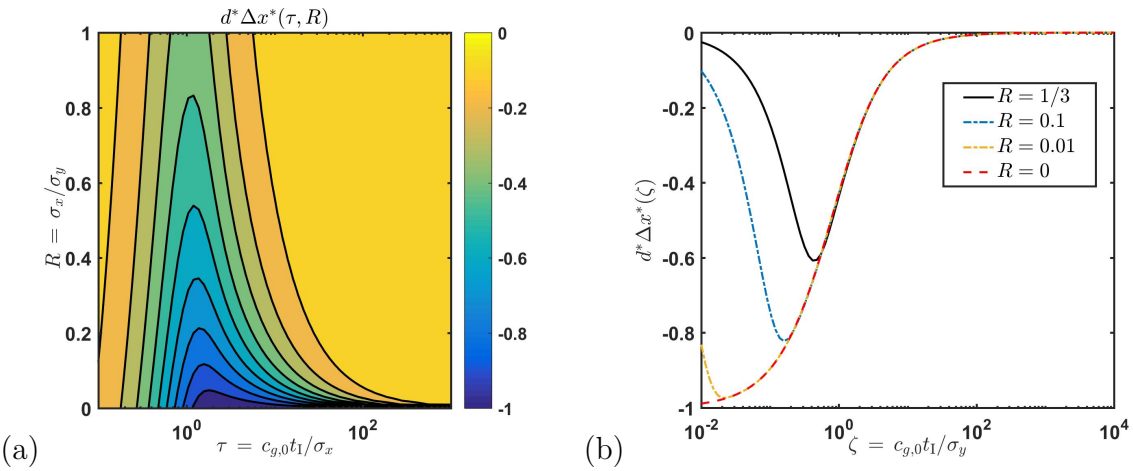

Figure 2.2: Scaled finite-time displacement by shallow unstratified flow: contour plot as a function of aspect ratio R and half-interval τ, obtained by numerically integrating (2.25) (panel (a)), and displacement obtained by numerical integration of (2.25) for three aspect ratios (continuous black and dash-dotted blue and yellow lines, respectively) and (2.28) (red dashed line) as a function of $\zeta = R\tau$ (panel (b)).

Figure 2.1 shows results obtained by numerical integration of (2.23) for particles at various depths in a 3D flow ($R = 1/3$), and in a 2D flow ($R = 0$). We plot the scaled finite-time return flow displacement $d^*\Delta x^*(\tau, R, z^*, d^*)$ (for brevity, we refer to this as the scaled finite-time displacement). The τ-axis is logarithmic to show the behaviour for very small and very large τ. Behaviour for small τ is 2D-like, while for large τ the continuous lines (3D) tend towards zero and the dashed lines (2D) to -1, as previously discussed in (2.17) and (2.15a). The two panels compare a shallower return flow ($d^* = 0.5$) and a deeper return flow ($d^* = 5$). Whereas the 2D finite-time displacement is very nearly monotonic for shallower return flows, it can overshoot near the surface for deeper return flows, reflecting strong negative displacement underneath the centre of the packet being partly cancelled, subsequently, by positive displacement near the surface at the packet's leading and trailing edges. We have been unable to convert (2.23) into a more insightful form, so we consider the limiting case of a shallow return flow, corresponding to $d^* = d/\sigma_x \ll 1$. In this limit, the return flow's vertical variation is negligible, and (2.23) takes the form

$$\Delta x^*(\tau, R) = -\frac{2}{d^*\pi^{3/2}} \int_0^\infty \int_0^\infty \frac{\mu \sin(\mu)}{\mu^2 + (R\tau)^2\lambda^2} e^{-\mu^2/(4\tau^2)} e^{-\lambda^2/4} d\mu d\lambda. \tag{2.24}$$

The integral over λ may be performed analytically, yielding a single integral over μ,

$$\Delta x^*(\tau, R) = -\frac{2}{d^*\sqrt{\pi}} \int_0^\infty \frac{\sin\mu}{\mu} e^{-\mu^2/(4\tau^2)} f\left(\mu/\left(2R\tau\right)\right) d\mu, \tag{2.25}$$

where the function $f(\xi) \equiv \xi \exp(\xi^2)\operatorname{erfc}(\xi)$ for an arbitrary argument ξ captures how the finite-time displacement varies with R; its relevant small and large $R\tau$ limits are

$$\lim_{R\tau\to 0} f\left(\frac{\mu}{2R\tau}\right) = \frac{1}{\sqrt{\pi}}, \qquad \lim_{R\tau\to\infty} f\left(\frac{\mu}{2R\tau}\right) = 0. \tag{2.26a,b}$$

We can split (2.25) into the sum of two integrals

$$\begin{aligned}\Delta x^*(\tau, R) = &-\frac{2}{d^*\sqrt{\pi}} \int_0^\infty e^{-\mu^2/(4\tau^2)} \frac{\sin\mu}{\mu} \left(f\left(\frac{\mu}{2R\tau}\right) - \frac{1}{\sqrt{\pi}} \right) d\mu \\ &- \frac{2}{d^*\pi} \int_0^\infty e^{-\mu^2/(4\tau^2)} \frac{\sin\mu}{\mu} d\mu,\end{aligned} \tag{2.27}$$

the latter of which equals the 2D finite-time shallow return flow displacement. To examine the long-time behaviour we take $\tau \gg 1$, so that the second term approaches $-1/d^*$ (cf. (2.15a)), and the Gaussian in the first can be set to 1. We examine the regime $R \ll 1$, $\tau \gg 1$, when the displacement becomes a function of a single, $O(1)$ parameter, $\zeta \equiv R\tau = c_g t_\mathrm{I}/\sigma_y$, corresponding to the half-interval t_I scaled on the packet width σ_y rather than its length σ_x. We obtain

$$\Delta x^*(\zeta) = -\frac{2}{d^*\sqrt{\pi}} \int_0^\infty \frac{\sin\mu}{\mu} \left(f\left(\frac{\mu}{2\zeta}\right) - \frac{1}{\sqrt{\pi}} \right) d\mu - \frac{1}{d^*}. \tag{2.28}$$

Figure 2.2(a) shows contours plots of the scaled finite-time displacement by a shallow return flow obtained by numerically integrating (2.21), demonstrating that the maximum negative displacement occurs for $\tau \sim 1$. From (2.28) and (2.26), it is clear that a transition between 2D-like behaviour ($\zeta \ll 1$) and 3D-like behaviour ($\zeta \gg 1$) occurs when $\zeta \sim 1$ ($t_\mathrm{I} \sim \sigma_y/c_g$). 2D-like behaviour can thus persist for arbitrarily large τ, given arbitrarily small amounts of localisation in y (small R, or nearly-unidirectional packets). Figure 2.2(b) compares numerical integration of (2.24) with numerical integration of its large-τ limit (2.28).

We note in passing that incorrect non-zero values of net return-flow displacements obtained from numerical integration in van den Bremer and Taylor (2016) (2D, infinite depth) and van den Bremer and Taylor (2015) (3D) resulted from insufficiently large limits on the integrals; these limits may need to be as large as $\tau \sim 10^2 - 10^3$ for the small R values used therein.

2.3 Stratified flow

2.3.1 Governing equations

In this section, we consider propagation of surface waves on a stratified fluid. To include density stratification effects, we decompose the varying density as (Phillips, 1977)

$$\rho = \rho_0 \left(1 + \frac{1}{g}\int_z^0 N^2(z')dz' - \frac{b}{g}\right), \tag{2.29}$$

where $b(x, y, z, t) = -g\Delta\rho/\rho_0$ is the buoyancy perturbation, and N is the buoyancy frequency, which we assume to be constant. Invoking the Boussinesq approximation by neglecting density differences unless they result in a body force through multiplication by g, the governing equations are e.g. Haney and Young, 2017

$$\boldsymbol{\nabla}\cdot\boldsymbol{u} = 0, \qquad \partial_t\boldsymbol{u} + \boldsymbol{u}\cdot\boldsymbol{\nabla}\boldsymbol{u} = -\boldsymbol{\nabla}p + b\hat{\boldsymbol{z}}, \qquad \partial_t b + \boldsymbol{u}\cdot\boldsymbol{\nabla}b + wN^2 = 0, \tag{2.30a,b,c}$$

where p is the departure from hydrostatic pressure. The system (2.30) must be solved subject to dynamic and kinematic boundary conditions at the surface. Only the dynamic boundary condition ($p_{\text{tot}} = 0$ at $z = h(x, y, t)$, where p_{tot} is the total pressure) is modified by density stratification, and we have, correct to second order (Haney and Young, 2017),

$$w = \partial_t h + \boldsymbol{u}_{\text{H}}\cdot\boldsymbol{\nabla}_{\text{H}}h\Big|_{z=0}, \qquad p + h\partial_z p = gh - N^2h^2/2\Big|_{z=0}. \tag{2.31a,b}$$

We solve the set (2.30)-(2.31) using a Stokes expansion as before and consider directly the 3D case.

First-order solutions: $O(\alpha)$

Following Haney and Young (2017), we neglect the buoyancy force and the vorticity it generates in the first-order equations. From the linearised equation (2.30c) and boundary condition (2.31a), we have $b_1 \sim -N^2h_1$. Taking the curl of the linearised (2.30b), we thus obtain for the non-dimensional vorticity

$$\frac{|\boldsymbol{\nabla}\times\boldsymbol{u}_1|}{k_0a_0\omega_0} \sim \frac{|\left(\hat{\boldsymbol{z}}\times\boldsymbol{\nabla}_{\text{H}}\right)b_1|}{k_0a_0\omega_0^2} \sim \frac{N^2}{\omega_0^2}, \tag{2.32}$$

from which it is evident that vorticity is small provided $(N/\omega_0)^2$ is small. For surface gravity waves in the ocean, $(N/\omega_0)^2$ is at most $O(10^{-3})$, and so the linear waves may be treated as irrotational by ignoring the small b_1 (see table 2.1 for typical parameter values).

Second-order solutions: $O(\alpha^2)$

At second order we retain the wave-averaged buoyancy, and so the Eulerian-mean flow is not irrotational. Wave-averaging the set (2.30), and defining the appropriate Bernoulli function to be $\varpi_2 \equiv p_2 + \overline{|\mathbf{u}_1|^2}/2$, the Eulerian-mean flow equations are (Haney and Young, 2017)

$$\boldsymbol{\nabla}\cdot\boldsymbol{u}_2 = 0, \qquad \partial_t \boldsymbol{u}_2 = -\boldsymbol{\nabla}\varpi_2 + b_2\hat{\boldsymbol{z}}, \qquad \partial_t b_2 = -w_2 N^2. \tag{2.33a,b,c}$$

We have neglected $\overline{\boldsymbol{u}_1\cdot\boldsymbol{\nabla}b_1}$ in (2.33c); by (2.32) this is $O((N/\omega_0)^2)$ smaller than the other terms. Taking propagation along the x-axis, and using (2.7) with p_1 in place of $-\partial_t\phi_1$ since the waves are irrotational, we may rewrite (2.31b) using the Bernoulli function as

$$w_2|_{z=0} = \partial_t h_2 + \partial_x M, \qquad \varpi_2|_{z=0} = g h_2 - N^2\overline{h_1^{\,2}}/2, \tag{2.34a,b}$$

where M is the x-component of $\boldsymbol{M}$ defined in (2.6). We eliminate all variables in favour of the vertical velocity w_2, and make the rigid-lid approximation in (2.34a) (as in (2.8)). The original problem (2.33) reduces to solving an evolution equation for w_2 subject to the surface forcing and no-flow bottom boundary condition,

$$\left((\partial_{\tilde{x}}-\eta)^2\left(\partial_x^2+\partial_y^2+\partial_z^2\right)+q^2\left(\partial_x^2+\partial_y^2\right)\right)w_2 = 0, \qquad w_2|_{z=0} = \partial_{\tilde{x}}M, \qquad w|_{z=-d} = 0, \tag{2.35a,b,c}$$

where $c_g\eta$ is a small, positive growth rate which we take to zero from above, ensuring that any radiated internal waves appear in the packet's wake, and $q \equiv N/c_g$ is the buoyancy wavenumber. By assuming the packet amplitude has been slowly growing from $t=-\infty$ (i.e $A_0(\tilde{x},y)e^{c_g\eta t}$), in the packet's reference frame we have

$\partial_t = -c_g(\partial_{\tilde{x}} + \eta)$. Throughout, we take q (hence N) to be constant. The vertical velocity w_2 is obtained from (2.35) as the Fourier transform

$$w_2\left(\tilde{x}, y, z, d, q\right) = \frac{1}{4\pi^2} \lim_{\eta \to 0^+} \iint_{\mathbb{R}^2} ik\hat{M} \frac{\sinh\left((z+d)|\boldsymbol{k}|\beta_{\eta,q}(k)\right)}{\sinh\left(d|\boldsymbol{k}|\beta_{\eta,q}(k)\right)} e^{ik\tilde{x}} e^{ily} dk dl, \quad (2.36)$$

where we have adopted the compact notation

$$|\boldsymbol{k}| \equiv \sqrt{k^2 + l^2}, \qquad \beta_{\eta,q}(k) \equiv \sqrt{\frac{(k+i\eta)^2 - q^2}{(k+i\eta)^2}}. \quad (2.37a,b)$$

To obtain the horizontal component u_2 from w_2 we first link vorticity generation to the rotated gradient of buoyancy by taking the curl of momentum equation (2.33b),

$$\partial_t \left(\boldsymbol{\nabla} \times \boldsymbol{u}_2\right) = -\left(\hat{\boldsymbol{z}} \times \boldsymbol{\nabla}_{\mathrm{H}}\right) b_2 = \left(\partial_y b_2, -\partial_x b_2, 0\right), \quad (2.38)$$

from which it immediately follows that the vertical vorticity component is time-independent. Assuming this vanishes, $\partial_y u_2 - \partial_{\tilde{x}} v_2 = 0$; combining this with the incompressibility condition (2.33a) leads to a Poisson-like equation relating u_2 to w_2,

$$-\left(\partial_{\tilde{x}}^2 + \partial_y^2\right) u_2 = \partial_{\tilde{x}} \partial_z w_2. \quad (2.39)$$

This equation is vacuously true in unstratified flow when it reduces to Laplace (since $u_2 = \partial_x \phi_2$ and $w_2 = \partial_z \phi_2$), but nontrivial for a stratified flow. The transform $\hat{u}$ of u_2 may be found from $\hat{w}$ using (2.39) as $\hat{u} = ik\partial_z \hat{w}/(k^2 + l^2)$. In physical space,

$$u_2\left(\tilde{x}, y, z, d, q\right) = -\frac{1}{4\pi^2} \lim_{\eta \to 0^+} \iint_{\mathbb{R}^2} \frac{k^2 \hat{M}}{|\boldsymbol{k}|} \beta_{\eta,q}(k) \frac{\cosh\left((z+d)\,|\boldsymbol{k}|\beta_{\eta,q}(k)\right)}{\sinh\left(d|\boldsymbol{k}|\beta_{\eta,q}(k)\right)} e^{ik\tilde{x}} e^{ily} dk dl. \quad (2.40)$$

Setting q to zero recovers ∂_x(2.16). As $\eta \to 0^+$, the integral in equation (2.40) is dominated by the region in wavenumber space where the denominator vanishes, corresponding to 'resonant curves' see Haney and Young, 2017, eq. 3.12. These do not lead to meaningful simplifications of (2.40); to find finite-time displacements we integrate (2.40) numerically with η small but nonzero.

Due to the stratification-dependent square root $\beta_{\eta,q}(k)$ defined in (2.37b), delta-function arguments for finding the net displacement, e.g.(2.17), become problematic: it is unclear that $\hat{u}$ is well-defined at $k = 0$. Instead, time-integrating the z-component of vorticity in (2.39) gives $\partial_y \Delta x = 0$, so that the 3D net displacement

is at most a function of z. Considering the subsequent limit $|y| \to \infty$ forces Δx to be globally zero, which is borne out in figure 2.4, where we show contour plots of finite-time displacements evaluated by numerical time-integration of (2.40). As incompressibility holds, (2.20) indicates that the mass-balance argument is not fundamentally altered by the presence of an internal wave wake in 3D. Nor is the fact that the time and area integrals do not commute altered, so that the above again depends on taking the time limit before the limit $|y| \to \infty$, as explained below (2.20). The special case of a 2D wavepacket is obtained by setting $\hat{M}(k,l) = 2\pi\hat{M}(k)\delta(l)$ in (2.40) and performing the l-integral. For net displacements, the l-integral must be performed before the time integral, as discussed in §2.2.4 (the integrals over $\delta(k)$ and $\delta(l)$ do not commute). This gives $|\boldsymbol{k}|\beta_{\eta,q}(k) = |k/(k+i\eta)|\sqrt{(k+i\eta)^2 - q^2}$, and the velocity integral becomes, following some small-η approximations,

$$u_2 = -\frac{1}{2\pi}\lim_{\eta\to 0^+}\int_{-\infty}^{\infty}\hat{M}(k)\sqrt{(k+i\eta)^2-q^2}\frac{\cosh\left((z+d)\sqrt{(k+i\eta)^2-q^2}\right)}{\sinh\left(d\sqrt{(k+i\eta)^2-q^2}\right)}e^{ik\tilde{x}}dk. \tag{2.41}$$

Integrating over time results in a delta-function at $k = 0$, so for a Gaussian packet, the net displacement is then given by

$$d^*\Delta x^*\left(z/d, qd, d^*\right) = -qd\frac{\cos\left(qd(1+z/d)\right)}{\sin\left(qd\right)}. \tag{2.42}$$

Unlike in the unstratified case, the net displacement is now a function of z and the parameter $qd = Nd/c_g$, which measures the ratio of ocean depth d to the vertical scale (c_g/N) of the $k_1 = \sqrt{q^2 - \pi^2/d^2} = 0$ internal wave which would be forced were the ocean deep enough. Depth-profiles of (2.42) are shown in figure 2.3 for different qd-values. We now explore the role of the stratification measure qd. As $qd \to 0$, a Taylor expansion of (2.42) gives the dependence of net displacement on weak stratification

$$\Delta x^* = -\frac{1}{d^*}\left(1 + \frac{q^2d^2}{6} - \frac{q^2d^2}{2}(1+z/d)^2 + O\left((qd)^3\right)\right), \tag{2.43}$$

which recovers the unstratified result $\Delta x = -1/d^*$ upon neglecting terms $O((qd)^2)$. To leading order, the magnitude of net displacement is predicted to decrease above a depth $z/d = -(1-1/\sqrt{3}) \approx -0.42$, and increase below, as shown in figure 2.3(a)-(b).

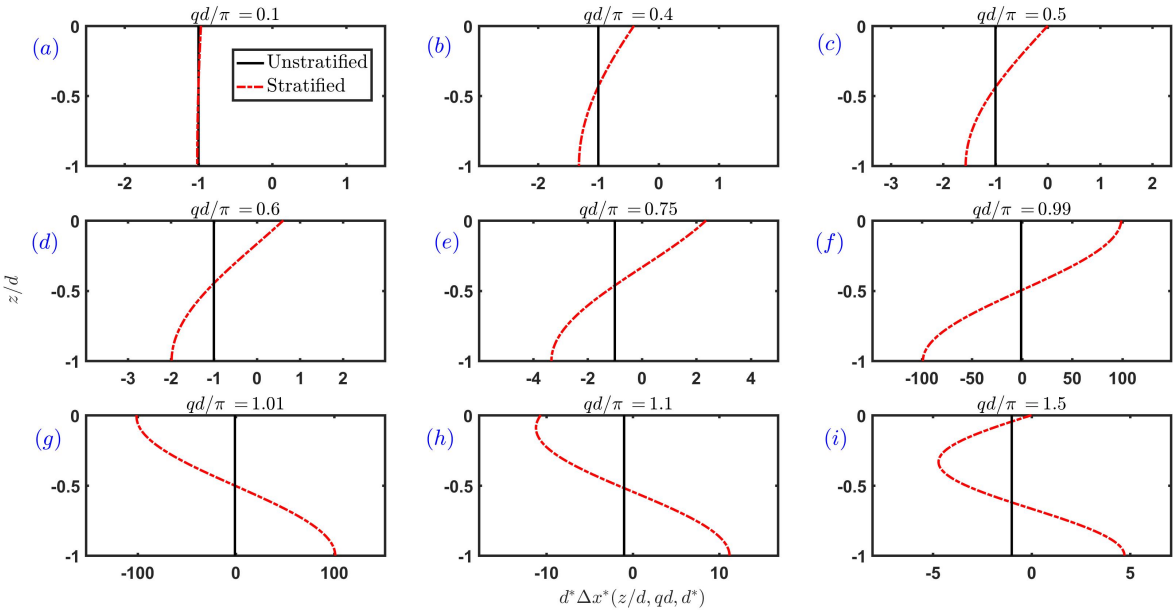

Figure 2.3: Scaled net displacement $d^*\Delta x$ by the return flow of a 2D packet in stratified flow from (2.42) as a function of depth z/d for various values of the stratification measure $qd = Nd/c_{g,0}$.

If $qd = \pi/2$, the net return-flow displacement remains negative and monotonic throughout the entire depth, but is zero at the surface,

$$d^*\Delta x^* = -\frac{\pi}{2}\sin\left(\frac{\pi}{2}\frac{|z|}{d}\right). \tag{2.44}$$

This is illustrated in figure 2.3(c). The stratification is not yet strong enough to support a wake of internal waves with phase speeds $\geq c_g$, but is sufficiently strong to bring the near-surface displacement to zero. For somewhat greater stratification $\pi > qd > \pi/2$, the net displacement becomes positive near the surface, as illustrated in figures 2.3(d)-(f).

Only when $qd > \pi$ are free internal waves generated in the wake of a 2D packet (figure 2.3(g)-(i)). This corresponds to $N > \pi c_g/d$. As qd traverses π (more generally $n\pi$), the displacement profile undergoes a sign change (cf. figure 2.3(f)-(g)). When $qd \to n\pi$, with n a positive integer, the displacement becomes singular (and very large in close proximity, cf. figure 2.3(f)-(g)), corresponding to a resonance in which c_g matches the x-phase speed of a long internal wave with $k_n = \sqrt{q^2 - n^2\pi^2/d^2} = 0$.

The Stokes drift is unaltered by stratification when the waves are treated as irrotational, so the net Lagrangian displacement in 2D is obtained as the expression

$$\Delta x_{\mathrm{L}}^{*} = \left(2k_0 \sigma_x e^{2k_0 z} - \frac{1}{d^*} (qd) \frac{\cos\left(qd\left(1+z/d\right)\right)}{\sin\left(qd\right)} \right). \tag{2.45}$$

The depth integral of (2.45) from $-d$ to 0 remains zero, so the return flow still balances the transport M: density stratification alters the manner in which the return flow transports mass without changing the vertically-integrated mass balance.

Finally, figure 2.4 summarises the combined effect of directional spread and stratification by showing contours of scaled finite-time displacement as a function of the stratification measure qd/π and aspect ratio R at different $\tau = 1, 10, 100$. To focus on what is realistic for the ocean, we take $0 \leq qd/\pi \leq 0.6$ (see table 2.1), so stratification generally reduces the magnitude of the displacement near the surface and enhances it to become more negative at depth (cf. figure 2.3(a)-(d)). At small $\tau = 1$ (figure 2.4(a) and (d)), stratification does not have an impact at the surface where the displacements reach their peak values, but its effects can be observed at depth, despite the very small displacements here. At intermediate $\tau \sim 10$ (figure 2.4(b) and (e)), negative displacement near the surface is mainly reduced by the influence of spanwise localisation, and only weakly by stratification. The contours at depth resemble those at smaller $\tau \sim 1$ albeit with larger magnitudes, as particles at the bottom begin to experience the flow but have not yet been affected by R. At large $\tau \sim 100$, displacements have practically vanished for all but very small aspect ratios, recovering the 2D long-time limit (2.42) as $R \to 0$ (cf. figure 2.3(a)-(d)).

2.4 Conclusions

We have examined the Lagrangian displacement induced by isolated non-dissipating surface gravity wavepackets and, in particular, the displacement associated with the wave-induced return flow, focussing on the effects of localisation in the spanwise coordinate y (as a proxy for weak directional spreading) and density stratification. For spanwise-infinite wavepackets (2D) on an unstratified flow, the net displacement associated with the return flow — where 'net' means computed over an infinite time

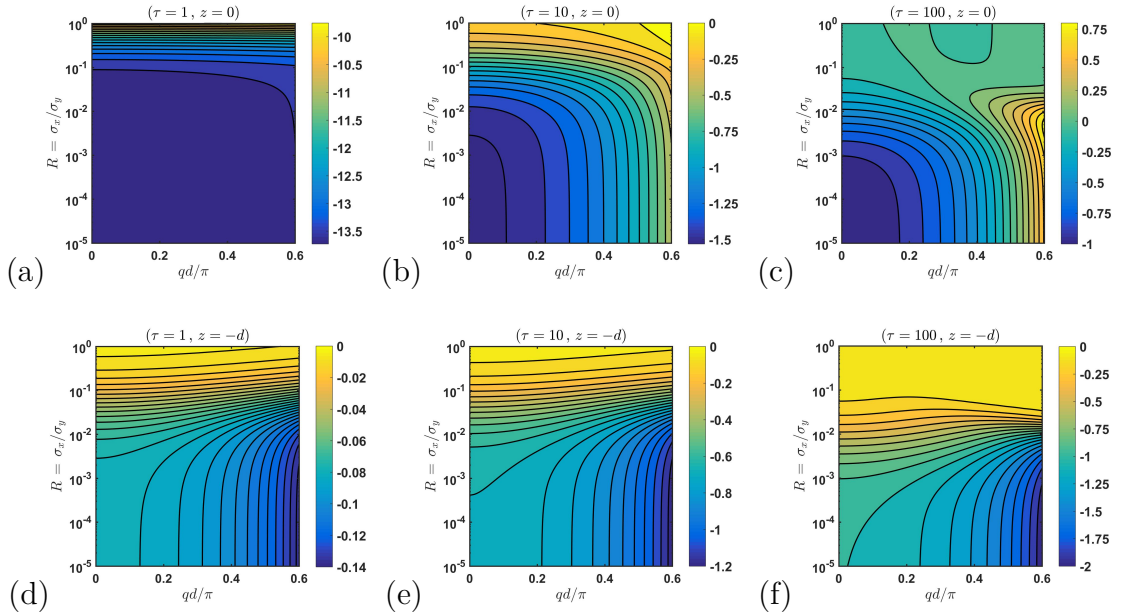

Figure 2.4: Contours of scaled finite-time displacement: panels (a)-(c) correspond to $z = 0$ and panels (d)-(f) to $z = -d$. Moving from left to right, the half-interval τ is increased sequentially by a factor of 10, from (a) and (d) plotted at $\tau = 1$, to (c) and (f) plotted at $\tau = 100$.

interval as the packet propagates from $x = -\infty$ to $x = \infty$ — is independent of the depth coordinate z. The net displacement is inversely proportional to the ocean depth d, and therefore goes to 0 when $d \to \infty$, as dictated by mass conservation. In the presence of any localisation of the packet in y, the net displacement becomes zero at each (y, z), regardless of the depth d. Over a finite, symmetric time interval, with the wavepacket starting a finite distance behind the x-origin and propagating to the same distance ahead (see (2.21)), the return flow in 3D initially displaces particles in the same manner as in 2D, but ultimately brings particles back to their original positions as the flow returns around as well as underneath the packet. This 2D-3D transition occurs on a timescale $\sim \sigma_y/c_g$, where σ_y is the packet's width (proportional to the degree of directional spreading) and c_g is the surface wave group velocity.

Density stratification alters the profile of the net displacement by the return flow of 2D packets: the net displacement becomes an oscillatory function of z with a wavelength dependent on the parameter qd, where $q \equiv N/c_g$ is the vertical buoyancy wavenumber, d is the ocean depth, and N is the (constant) buoyancy frequency. For

Parameter	Range	Typical value
α	$0 - 0.3$	0.05
d [m]	$3 \times 10^1 - 1.1 \times 10^4$	3.1×10^3
ω_0 [s^{-1}]	$2\pi/20 - 2\pi/1.0$	$2\pi/10$
ε	$0 - 0.15$	0.04
σ_θ [deg]	$0 - 30$	5.0
R	$0 - 1$	4.9×10^{-3}
N [s^{-1}]	$2\pi/(2.0 \times 10^3) - 2\pi/(1.3 \times 10^3)$	$2\pi/(1.3 \times 10^3)$
qd/π	$0 - 1$	0.6

Table 2.1: Realistic parameter ranges and typical values chosen (compiled from Haney and Young, 2017; van den Bremer and Taylor, 2015; Ewans, 2002; Toffoli and Bitner-Gregersen, 2017).

$qd < \pi$, as is typical for the ocean, stratification diminishes displacements near the surface and enhances them at depth. When $qd \to \pi$ (more generally, for $qd \to n\pi$), the net displacement becomes singular due to a resonance between c_g and the phase velocity of a long internal wave mode, while for $qd > \pi$, it is finite but of opposite sign. In the presence of any localisation of the packet in y, the net displacement again reduces to zero. Stratification may, however, appreciably alter the finite-time displacement, with the signature of the internal wave wake generally present for all times at depth, and only for larger times at the surface.

In order to obtain a quantitative estimate of magnitudes of the displacements, we recall from (2.15) the displacement scale $\alpha^2\sqrt{\pi}\sigma_x/(k_0 d)$, with $\alpha \equiv a_0 k_0$, by which we multiply the colour scale in figure 2.4 to obtain dimensional displacements. To consider how large this displacement scale can be, we take the largest possible value of $\alpha = 0.3$, the smallest value of $k_0 d = 3$ for the deep-water assumption to still hold, and $\sigma_x = (2k_0\varepsilon)^{-1} = 3.1 \times 10^2$ m, corresponding to typical values $\omega_0 = 2\pi/10$s, $d = 75$ m, $\varepsilon = 0.04$ (see table 2.1). We then obtain a displacement scale $\alpha^2\sqrt{\pi}\sigma_x/(k_0 d) = 17$ m. For a more usual depth $d = 3.1 \times 10^3$ m, this reduces to 0.41 m and even further to 0.011 m for the more typical steepness $\alpha = 0.05$. For unstratified flow in 2D, the displacement scale gives the dimensional net return-flow displacement (times -1). We will now consider typical values of qd and $R = \sigma_x/\sigma_y$.

2.4.1 Quantitative effect of directional spreading

In order to relate the value of the packet aspect ratio R to typical values of the (root-mean-square) directional spreading of the energy spectrum σ_θ reported in the literature (e.g. Ewans, 2002), we use the relationship $R \approx \sqrt{2}\varepsilon\sigma_\theta$, which is only valid in the limit of weak directional spreading. Taking a value of $\sigma_\theta = 5.0°$ typical of swell conditions (Ewans, 2002) and $\varepsilon = 0.04$, we obtain $R = 4.9 \times 10^{-3}$, increasing to $R = 1.9 \times 10^{-2}$ for a very narrow-banded packet with $\varepsilon = 0.15$, and further to $R = 0.11$ for a highly directionally-spread packet with $\sigma_\theta = 30°$. The timescale on which the transition from 2D-like to 3D-like behaviour occurs $\sim \sigma_x/(c_g R) = (R\varepsilon\omega_0)^{-1}$, can thus be as large as $8.1 \times 10^3\,\mathrm{s}$ ($R = 4.9 \times 10^{-3}, \varepsilon = 0.04$) or $3.6 \times 10^2\,\mathrm{s}$ ($R = 0.11, \varepsilon = 0.15$) for the typical $\omega_0 = 2\pi/10\,\mathrm{s}^{-1}$ considered before, with corresponding much shorter packet-translation times of $\sigma_x/c_g \approx 40\,\mathrm{s}$ and $11\,\mathrm{s}$, respectively.

2.4.2 Quantitative effect of stratification

Taking a typical ocean depth $d = 3.1 \times 10^3\,\mathrm{m}$ and a (constant) value of $N = 2\pi/1333\,\mathrm{s}^{-1}$, we obtain $qd/\pi = 0.6$. The 2D net return-flow displacement is then zero at $z = -5.0 \times 10^2\,\mathrm{m}$ (cf. panel (d) of figure 2.3). Net displacement at the surface is positive, and its maximum (negative) value occurs at the ocean floor. The behaviour predicted for larger qd values, including the resonance at $qd = n\pi$, is unlikely to arise in the real ocean, since stratification is generally too weak to satisfy this resonance. Furthermore, the depth-variability of N observed in real oceans (e.g. exponential, or piecewise-linear in a crude approximation) would likely weaken the role of stratification predicted here, and prevent exact resonances. Large displacements are also likely to be mitigated by viscous dissipation, and we expect that, near resonance, transfer of energy from the surface wavepacket to the internal wave wake may lead to disintegration of the packet.

2.4.3 Neglected effects: wave dispersion, viscosity and the earth's rotation

In this paper, in addition to considering the abstract case of an isolated wavepacket, we have ignored the effects of wave dispersion beyond leading order in ε, viscosity (resulting in a non-dissipating wavepacket) and the earth's rotation. We will explore the potential consequences of these assumptions below. In terms of wave dispersion, we have examined only leading-order solutions in the small bandwidth parameter ε; at the next order, two effects need to be accounted for. First, we used the rigid-lid approximation to neglect the set-down of the wave-averaged free surface h_2 (given by (2.5)) when calculating return flow displacements. In appendix .1, we show that including the set-down results in multiplication of the net displacement by at most a factor $(1 - \varepsilon^2\sigma_x/d)^{-1}$, with the largest correction occurring for a 2D shallow return flow. Even for larger ε, this effect is small. Second, we have assumed that the packet propagates without any change in shape. In appendix .2 we find that, to leading order, the enhancement of displacement due to wave dispersion is $(1 + \varepsilon^2/2)$, which again is small even for large ε.

Longuet-Higgins (1953) introduced viscous boundary layers, of the type studied by Rayleigh (1883), in which mean vorticity is generated and then slowly diffused into the fluid interior, eventually altering the mass transport profiles. The viscous boundary layer thickness $\delta = \sqrt{2\nu/\omega_0}$, where ν is the kinematic viscosity of seawater is generally of the order of millimetres. When $a_0^2 \gg \delta^2$, the relevant case for a wavepacket, vorticity diffuses into the fluid interior on a timescale $\sim \sigma_x/\left(a^2\omega k\right) = \alpha^{-2}\varepsilon^{-1}\omega_0^{-1}$. This process takes multiple packet translation times, so vorticity will not have had sufficient time to diffuse into the fluid interior before the packet has propagated past. Nevertheless, the long-time behaviour may be affected.

On a rotating earth, Ursell (1950) demonstrated that a steady Stokes drift would violate conservation of circulation, implying that the Lagrangian-mean velocity accompanying a regular, horizontally uniform wavetrain must be zero in the long-time average over many inertial periods. It follows that there must be a long-time-average Eulerian-mean 'anti-Stokes flow' possessing vorticity, cancelling

the Stokes drift. In an initial-value problem starting with an irrotational Stokes wave with its Stokes drift - as with swell arriving in previously calm water - the Coriolis force induces free inertial oscillations. Further aspects of this problem were explored in Hasselmann (1970). As periods associated with the Earth's rotation are much longer than the translation timescale of a narrow-banded packet (see also Herbers and T. Janssen, 2016), we anticipate that Coriolis effects can be neglected when considering net displacements by the return flow. Two dimensionless numbers may play a role: $f\sigma_x/c_g$ and $f\sigma_y/c_g$. The first ($f\sigma_x/c_g$) is only appreciably large for a long, slow-moving packet, or for strong rotation. However, the second is large for almost-unidirectional waves, leaving open the possibility that rotation affects the mean flow, which we hope to examine in future work. We also note that, when rotation and eddy viscosity are included together, the mean flow may be appreciably changed over the associated Ekman depth $\sim (2\nu/f)^{1/2}$, which in real oceans is comparable to the Stokes depth $\sim (2k_0)^{-1}$ (e.g. Xu and Bowen, 1994). We do not consider these effects herein.

Chapter 3

Ekman–Stokes dynamics

Abstract

We examine Stokes drift and wave-induced transport of floating marine litter on the surface of a rotating ocean with a turbulent mixed layer. Due to Coriolis–Stokes forcing and surface wave stress, a second-order Eulerian-mean flow forms, which must be added to the Stokes drift to obtain the correct wave-induced Lagrangian velocity. We show that this wave-driven Eulerian-mean flow can be expressed as a convolution between the unsteady Stokes drift and an 'Ekman–Stokes kernel'. Using this convolution we calculate the unsteady wave-driven contribution to particle transport. We report significant differences in both direction and magnitude of transport when the Eulerian-mean Ekman–Stokes velocity is included.

3.1 Introduction

Floating marine debris, including plastic pollution, has rapidly become one of the most pressing environmental problems (Eriksen et al., 2014), particularly for marine ecosystems (Lavender Law, 2017). Although consensus exists about the longevity of plastic in the marine environment (Andrady, 2011) and the relatively large buoyancy of a significant share of plastic produced (Geyer et al., 2017), with both factors contributing to their long-distance transport, the total plastic budget of the world's oceans is poorly understood. A significant mismatch exists between the estimated amount of land-generated plastic that enters coastal waters (5-12 million tonnes yr^{-1}, Jambeck et al. (2015)) and the estimated total amount of plastic floating at sea (less than 0.3 million tonnes, Cózar et al. (2014), Eriksen et al. (2014), and van Sebille, Wilcox, et al. (2015)). Similarly, the amount of plastics measured at sea over the last few decades (Lebreton, Egger, et al., 2019; Ostle et al., 2019; Wilcox et al., 2020) has not kept pace with growth in global plastic production (Goldstein et al., 2012; Geyer et al., 2017). To understand this mismatch, an improved understanding of the physical processes governing transport and dispersion is required (van Sebille, Aliani, et al., 2020). This letter focuses on one of these processes: surface waves.

As a particle undergoes its periodic motion beneath surface waves, it experiences a Lagrangian-mean velocity in the waves' direction known as Stokes drift (Stokes, 1847). More generally, Stokes drift is the difference between the average Lagrangian velocity of a fluid parcel and the average Eulerian velocity of the fluid measured at a fixed spatial location (e.g. Bühler, 2014; van den Bremer and Breivik, 2017). Surface gravity waves on the open ocean are mostly caused by winds. At any location and time, the wave field is a superposition of waves that have been generated by earlier winds at another location. Wave models, such as WAM (The WAMDI Group, 1988) and WaveWatch-III (Tolman, 2009), have been developed to predict wave fields and thus Stokes drift (Webb and Fox-Kemper, 2011; Breivik, P. Janssen, et al., 2014).

A recent and growing body of literature is examining the role of Stokes drift in the transport and dispersion of floating plastic pollution. Iwasaki et al. (2017) showed that in the Sea of Japan, Stokes drift pushed microplastics closer to the

coast. Delandmeter and van Sebille (2019) and Onink et al. (2019) report a similar result in Arctic regions. Dobler et al. (2019) demonstrated that Stokes drift fundamentally changes transport patterns in the South Indian Ocean by shifting the convergence regions to the west, causing leakage into the South Atlantic rather than the South Pacific. Waves may also allow particles to cross strong circumpolar winds and currents (Fraser et al., 2018).

Crucially, the above studies have simply superimposed the Stokes drift obtained from the local wave field onto the Eulerian current field obtained from ocean general circulation models or observations. In doing so, they have ignored the fact that the Eulerian flow is itself modified by surface waves: on the rotating Earth, the Coriolis force associated with the Stokes drift drives an Eulerian-mean current in the turbulent upper-ocean boundary layer (Ursell, 1950; Hasselmann, 1970; Xu and Bowen, 1994; Lewis and Belcher, 2004), as noted in Onink et al. (2019). Together with the Stokes drift and the non-wave background flow, this wave-induced Eulerian current forms the Lagrangian velocity with which marine litter is transported. It is this wave-induced Eulerian current, which we call the Ekman–Stokes flow, that this letter examines.

We derive a model for computing the unsteady Eulerian-mean Ekman–Stokes response to a time-varying Stokes drift, taking into account the correct wave stress boundary condition and the Coriolis–Stokes forcing. We do so for the case of constant eddy viscosity in the turbulent upper-ocean layer and a quasi-monochromatic (or narrow-banded) wave field, and zero initial wave-induced Eulerian-mean velocity $\overline{\boldsymbol{u}} = \mathbf{0}$. The product of this letter is an Ekman–Stokes convolution kernel, which can readily be used to predict the wave-induced Eulerian-mean flow in the turbulent upper-ocean boundary layer and hence the Lagrangian transport of floating marine debris. This kernel is a low-computational-cost alternative to fully-coupled general circulation and wave models, which include the effect of waves in both the Coriolis–Stokes forcing and the surface boundary condition (Breivik, Mogensen, et al., 2015). Using sample wave field data from buoys, we show that accounting for the

Eulerian-mean Ekman–Stokes response to a time-varying Stokes drift considerably alters the trajectories of drifting objects.

3.2 Unsteady Ekman–Stokes flow

We consider a homogeneous (constant-density), incompressible ocean of constant depth d, described by horizontal coordinates x and y, and a vertical coordinate z measured upwards from the undisturbed water level. The governing equations, divided through by the (constant) density ρ, are

$$\partial_t \boldsymbol{u} + \boldsymbol{u}\cdot\boldsymbol{\nabla}\boldsymbol{u} + \boldsymbol{f}\times\boldsymbol{u} = -\boldsymbol{\nabla}p + \nu\nabla^2\boldsymbol{u}, \qquad \boldsymbol{\nabla}\cdot\boldsymbol{u} = 0, \tag{3.1a}$$

$$w\,|_{z=\eta} = \partial_t\eta + \boldsymbol{u}_{\mathrm{H}}|_{z=\eta}\cdot\boldsymbol{\nabla}_{\mathrm{H}}\eta, \qquad \hat{\boldsymbol{n}}\cdot\overleftrightarrow{\boldsymbol{\tau}}\cdot\hat{\boldsymbol{s}}|_{z=\eta} = 0, \tag{3.1b}$$

$$w\,|_{z=-d} = 0, \tag{3.1c}$$

where $z=\eta(x,y,t)$ denotes the free surface elevation, $\boldsymbol{u}$ is the three-dimensional velocity vector, $\boldsymbol{f}$ the Coriolis vector, $\boldsymbol{A}_{\mathrm{H}} \equiv (A_x, A_y, 0)$ the horizontal component of any $\boldsymbol{A}$, and $\overleftrightarrow{\boldsymbol{\tau}}$ the stress tensor with components $\tau_{ij} = -(p-p_0)\delta_{ij} + \nu(\partial_i u_j + \partial_j u_i)$, with p_0 the atmospheric pressure divided by the (constant) density ρ and ν the turbulent eddy viscosity, taken constant. The unit vectors $\hat{\boldsymbol{n}}$ and $\hat{\boldsymbol{s}}$ are normal and tangential to the free surface respectively, so (3.1b) is a stress-free condition.

3.2.1 Wave-averaged mean-flow equations

We assume the wave steepness is small, $\alpha \equiv kA \ll 1$, where A is the peak wave amplitude of η and k the peak wavenumber, and solve (3.1) to $O(\alpha^2)$ using a Stokes expansion $\boldsymbol{u} = \boldsymbol{u}_1 + \boldsymbol{u}_2 + \cdots$, where the subscript denotes the order in α. We focus on deep-water waves ($kd \gg 1$).

Linear wave dynamics arises at $O(\alpha)$, where we ignore viscous effects, neglecting a thin vorticity boundary layer of thickness $\delta_\nu = \sqrt{2\nu/\omega}$ under the (generally satisfied) assumption $k\delta_\nu \ll 1$. Consequently, we ignore viscous damping of waves as they propagate. In contrast, the Coriolis force must be retained since, as demonstrated by Hasselmann (1970), $O(f/\omega)$ corrections put horizontal and vertical velocity components out of quadrature, with impact on the wave-averaged dynamics.

Integrating the $O(\alpha^2)$ equations over a wave period, we obtain the wave-averaged mean flow equations (e.g. Huang, 1979; Suzuki and Fox-Kemper, 2016)

$$\partial_t \overline{u} - f v_{\mathrm{L}} = -\partial_x \overline{p} + \nu \nabla^2 \overline{u}, \qquad \partial_t \overline{v} + f u_{\mathrm{L}} = -\partial_y \overline{p} + \nu \nabla^2 \overline{v}, \tag{3.2a}$$

$$\partial_t \overline{w} = -\partial_z \overline{p} + \nu \nabla^2 \overline{w}, \qquad \partial_x \overline{u} + \partial_y \overline{v} = -\partial_z \overline{w}, \tag{3.2b}$$

where the overbar denotes a time average, $\boldsymbol{u}_{\mathrm{L}} = \overline{\boldsymbol{u}} + \boldsymbol{u}_{\mathrm{S}}$ is the Lagrangian (or particle-transport) velocity associated with the waves, with $\overline{\boldsymbol{u}} = \overline{\boldsymbol{u}_2}$ the wave-induced Eulerian-mean velocity and $\boldsymbol{u}_{\mathrm{S}}$ the Stokes drift, and the horizontal component of the Coriolis vector introduces only higher-order corrections to the flow. To derive (3.2a) and (3.2b) we assumed that the non-wave background flow has small Rossby number, $|\boldsymbol{\nabla} \times \boldsymbol{u}_{\mathrm{B}}|/f \ll 1$. It follows that the corresponding Stokes vortex force $(\boldsymbol{\nabla} \times \boldsymbol{u}_{\mathrm{B}}) \times \boldsymbol{u}_{\mathrm{S}}$ is negligible compared with the Coriolis–Stokes term, while $(\boldsymbol{\nabla} \times \overline{\boldsymbol{u}}) \times \boldsymbol{u}_{\mathrm{S}}$ is $O(\alpha^4)$ since it involves only the wave-induced flow (Suzuki and Fox-Kemper, 2016). The background $\boldsymbol{u}_{\mathrm{B}}$ can then simply be superimposed on the wave-induced Lagrangian flow $\boldsymbol{u}_{\mathrm{L}}$. Where the condition $|\boldsymbol{\nabla} \times \boldsymbol{u}_{\mathrm{B}}|/f \ll 1$ does not hold – for example, in a submesoscale front – a more complete treatment of the governing equations is required (e.g. McWilliams and Fox-Kemper, 2013).

Without the shear and pressure terms, equations (3.2a) and (3.2b) reduce to those considered by Hasselmann (1970). The horizontal momentum equations include the Coriolis–Stokes forcing $-f\hat{\boldsymbol{z}} \times \boldsymbol{u}_{\mathrm{S}}$ (Hasselmann, 1970; Polton et al., 2005) which drives an Eulerian 'anti-Stokes flow', cancelling the Stokes drift and exciting inertial oscillations. The anti-Stokes flow explains Ursell (1950)'s prediction of zero net drift for periodic waves in a rotating frame.

We focus on the horizontal momentum equations (3.2a) in the Stokes layer, that is, the top $O(k^{-1})$-deep layer of the ocean where the Stokes drift and hence the Coriolis–Stokes forcing are localised. One of the boundary conditions is provided by averaging the condition of zero tangential stress in (3.1b) (Longuet-Higgins (1953), Ünlüata and Mei (1970), Xu and Bowen (1994) and Seshasayanan and Gallet (2019)); it is given by

$$\partial_z \overline{\boldsymbol{u}}_{\mathrm{H}}|_{z=0} = \partial_z \boldsymbol{u}_{\mathrm{SH}}|_{z=0}. \tag{3.3}$$

Examining the viscous but non-rotating case, Longuet-Higgins (1953) showed that vorticity is transported from the viscous boundary layers into the fluid interior, affecting the mass transport profile (Ünlüata and Mei, 1970; Xu and Bowen, 1994; Seshasayanan and Gallet, 2019). Within these boundary layers the flow is not irrotational, resulting in a viscous stress upon the Eulerian-mean flow. Upon expanding the second equation in (3.2bb) about $z = 0$, performing a momentum budget, and averaging over a wave period, this leads to condition (3.3). Additional Eulerian-mean wave-induced transport, known as boundary-layer streaming, occurs in the boundary layer (e.g. Grue and Kolaas (2017)). The contributions of Hasselmann (1970) and Longuet-Higgins (1953) (and the theory of wind-driven currents of Ekman (1905)) were unified by Xu and Bowen (1994) into a model of wave (and wind-) driven flow in finite-depth water.

In the Stokes layer, vertical gradients dominate over horizontal ones. It follows from (3.2b) that the vertical velocity component and pressure gradient can be neglected. Introducing the complex notation $\mathcal{U} = \overline{u} + i\overline{v}$ as in Huang (1979), we obtain the Ekman–Stokes equations

$$(\partial_t + if - \nu\partial_z^2)\mathcal{U} = -if\mathcal{U}_{\mathrm{S}}(\boldsymbol{x}, z, t), \quad \partial_z\mathcal{U} = \partial_z\mathcal{U}_{\mathrm{S}}(\boldsymbol{x}, z, t)\Big|_{z=0}, \quad \lim_{z\to-\infty}\mathcal{U} = 0, \tag{3.4a,b,c}$$

where the boundary conditions follow from (3.3) and the requirement that the solution be matched to a weak Eulerian flow outside the Stokes layer. The Eulerian Ekman–Stokes velocity solving (3.4) is driven by the Stokes drift in two ways, via the Coriolis–Stokes forcing in the fluid interior (Polton et al., 2005) and via the wave stress (3.4b).

Note that a wind stress could be added to (3.4b); by linearity, the wind-driven Ekman velocity would be superimposed in convolution form on the wave-driven velocity we obtain (e.g. Madsen (1978) Eq. (21) for linearly-varying $\nu(z)$). In a coupled oceanic-atmospheric model, Lewis and Belcher (2004) derive steady solutions to (3.4) for non-constant viscosity, though they do not seem to include the wave stress.

3.2.2 Solution by Laplace transform

We solve (3.4) by Laplace transform, assuming that the Stokes drift $\mathcal{U}_\mathrm{S}$ has a time-independent vertical structure $\exp(2kz)$ corresponding to a quasi-monochromatic wave field, but an otherwise arbitrary time dependence. Denoting the Laplace transform by a tilde, with

$$\tilde{g}(s) = \mathcal{L}\left\{g(t)\right\} = \int_0^\infty g(t)e^{-st}dt, \quad g(t) = \mathcal{L}^{-1}\left\{\tilde{g}(s)\right\} = \frac{1}{2\pi i}\int_{\gamma-i\infty}^{\gamma+i\infty}\tilde{g}(s)e^{st}ds, \tag{3.5a,b}$$

where γ is a real number such that the contour path of integration is in the region of convergence of $\tilde{g}(s)$, we find that when $\mathcal{U}(t=0)=0$

$$\tilde{\mathcal{U}} = 2k\left(1+\frac{if}{s+if-4k^2\nu}\right)\frac{\tilde{\mathcal{U}}_\mathrm{S}e^{z\sqrt{(s+if)/\nu}}}{\sqrt{(s+if)/\nu}} - \frac{if\tilde{\mathcal{U}}_\mathrm{S}e^{2kz}}{s+if-4k^2\nu}. \tag{3.6}$$

This is the sum of a particular solution – the second term – which can be interpreted as a partial anti-Stokes flow varying over the Stokes depth $\delta_\mathrm{S} = (2k)^{-1}$, and a homogeneous solution – the first term – varying over the Ekman depth $\delta_\mathrm{E} = \sqrt{2\nu/f}$, which includes a contribution driven by the vertical shear of the anti-Stokes flow through boundary condition (3.4b) (second term in the brackets in (3.6)).

A special case of (3.6) occurs if $\mathcal{U}_\mathrm{S}$ approaches a steady value $\overline{\mathcal{U}_\mathrm{S}}$ as $t\to\infty$. Then $\tilde{\mathcal{U}}$ tends to the time-independent solution (cf. Seshasayanan and Gallet (2019))

$$\overline{\mathcal{U}} = \frac{(1-i)D}{2}\overline{\mathcal{U}_\mathrm{S}}\left(1+\frac{1}{1+iD^2/2}\right)e^{(1+i)z/\delta_\mathrm{E}} - \frac{\overline{\mathcal{U}_\mathrm{S}}e^{2kz}}{1+iD^2/2}, \tag{3.7}$$

where $D \equiv \delta_\mathrm{E}/\delta_\mathrm{S}$ is the fixed ratio of Ekman to Stokes depths. In the limit $D\to 0^+$, equation (3.7) approaches $-\overline{\mathcal{U}_\mathrm{S}}\exp(2kz)$: up to an inertial oscillation this is the so-called 'anti-Stokes' Eulerian-mean flow, predicted by Hasselmann (1970) to be induced by periodic waves in a rotating, inviscid ocean. Viscosity acts to reduce the shear in the anti-Stokes flow, so that a nonzero Lagrangian-mean velocity remains.

3.2.3 Ekman–Stokes kernel

We now use the Laplace convolution theorem to write the unsteady solution for the Ekman–Stokes mean flow as a function of time for arbitrary Stokes drift as

$$\mathcal{U}(\boldsymbol{x},z,t) = \mathcal{U}_\mathrm{S}|_{z=0} * K(z,t), \tag{3.8}$$

Limit	Behaviour	Theory
$t \to \infty$	$2k\sqrt{\nu}e^{-ift}/\sqrt{\pi t}\,[1 - if/(4k^2\nu)\,(1 - (1+2k^2z^2)/(4k^2\nu t))]$	long-time limit
$t \to 0^+$	$8\nu k^2\delta(z/\delta_{\mathrm{S}}) - ife^{2kz}$	short-time limit
$\nu \to 0^+$	$-ife^{-ift}e^{2kz}$	Hasselmann (1970)
$f \to 0^+$	$2k\sqrt{\nu}e^{-z^2/(4\nu t)}/\sqrt{\pi t}$	Longuet-Higgins (1953)

Table 3.1: Asymptotic behaviour of the Ekman–Stokes kernel $K(z,t)$.

where $*$ denotes convolution in time and

$$K(z,t) = \mathcal{L}^{-1}\left\{\frac{2ke^z\sqrt{(s+if)/\nu}}{\sqrt{(s+if)/\nu}} + \frac{if}{s+if-4k^2\nu}\left(\frac{2ke^z\sqrt{(s+if)/\nu}}{\sqrt{(s+if)/\nu}} - e^{2kz}\right)\right\}. \quad (3.9)$$

The convolution kernel $K(z,t)$, which we will term the Ekman–Stokes kernel, can be evaluated by deforming the integration contour involved in the inverse Laplace transform to obtain

$$K(z,t) = 2k\sqrt{\nu}e^{-ift}\frac{e^{-z^2/(4\nu t)}}{\sqrt{\pi t}} - ife^{\left(4k^2\nu - if\right)t}\sum_{\pm}\frac{e^{\pm 2kz}}{2}\,\mathrm{erfc}\left(\sqrt{4k^2\nu t} \pm \frac{z}{\sqrt{4\nu t}}\right), \quad (3.10)$$

where $\sum_{\pm}$ denotes the sum of the plus and minus terms and the complementary error function $\mathrm{erfc}(x) = 1 - \mathrm{erf}(x)$. An equivalent form emphasising dependence on wave parameters uses the scaled error function $\mathrm{erfcx}(t) = e^{t^2}\,\mathrm{erfc}(t)$ and reads

$$K(z,t) = 2k\sqrt{\nu}e^{-ift}\frac{e^{-z^2/(4\nu t)}}{\sqrt{\pi t}} - ife^{-ift}\frac{e^{-z^2/(4\nu t)}}{2}\sum_{\pm}\mathrm{erfcx}\left(\sqrt{4k^2\nu t} \pm \frac{z}{\sqrt{4\nu t}}\right). \quad (3.11)$$

The Ekman–Stokes kernel K captures the (Eulerian-mean) flow response to the Stokes drift. The $1/\sqrt{t}$ describes the establishment of an Ekman spiral driven by the wave stress; the if terms describe the impact of the Coriolis–Stokes forcing. Note that the dimension of $K(z,t)$ is time^{-1}.

Several limits of the kernel are of interest; they are given in dimensional terms in Table 3.1. The limits $\nu \to 0^+$ and $f \to 0^+$ are best understood by rewriting (3.11) in terms of the dimensionless parameters $D = \delta_{\mathrm{E}}/\delta_{\mathrm{S}}$, $\zeta = 2kz$ and $\tau = ft$ to obtain

$$K(\zeta,\tau)/f = De^{-i\tau}\frac{e^{-\zeta^2/(2D^2\tau)}}{\sqrt{2\pi\tau}} - \frac{i}{2}\sum_{\pm}e^{-i\tau-\zeta^2/(2D^2\tau)}\,\mathrm{erfcx}\left(D\sqrt{\frac{\tau}{2}} \pm \frac{\zeta}{\sqrt{2D^2\tau}}\right). \quad (3.12)$$

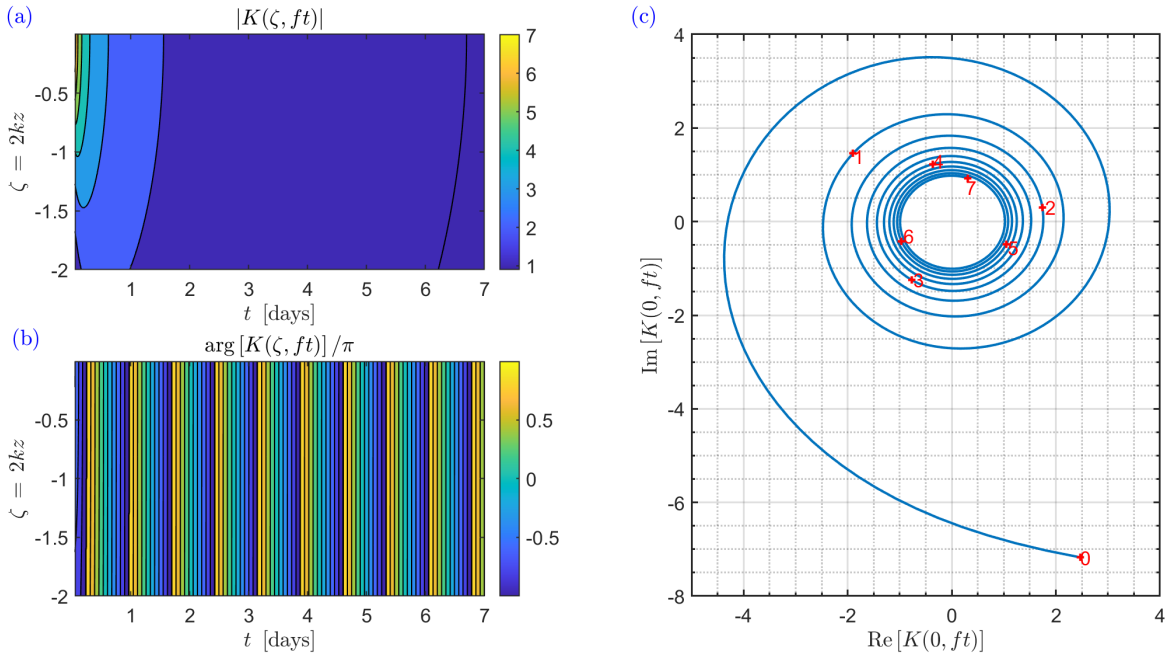

Figure 3.1: Ekman–Stokes kernel $K(\zeta, \tau)$ for $D = 1$ (with $f = 1 \times 10^{-4}\mathrm{s}^{-1}$): (a) magnitude and (b) argument as a function of depth and time, and (c) hodograph at the surface ($\zeta = 0$) with time (in days) shown in red. In panel (a) we have saturated the colour scale, as the kernel is singular at $(\zeta, \tau) = (0, 0)$.

When $D \gg 1$, e.g. because $f \to 0^+$, the Coriolis–Stokes sum term in (3.12) is negligible and the flow becomes the Longuet-Higgins (1953) response to the wave stress at the surface. In contrast, for $D \ll 1$, e.g. as $\nu \to 0^+$, the anti-Stokes result of Hasselmann (1970) is approached non-uniformly in ζ. This singular behaviour arises since for any $D \neq 0$ the shear condition at the surface cannot be met by an exact anti-Stokes flow, so in a thin layer of depth $\sim \sqrt{\nu/f}$ near the surface cancellation of the Stokes drift is imperfect (e.g. Seshasayanan and Gallet (2019)). Over long times $\tau \to \infty$, the Coriolis–Stokes terms decay on the viscous rather than the inertial timescale, despite being caused by Earth's rotation.

The magnitude and argument of the dimensionless kernel $K(\zeta, \tau)$ are shown in Figure 3.1 for $D = 1$. The magnitude is largest towards $(\tau, \zeta) = (0, 0)$ due to the singular behaviour discussed above. The kernel has the character of an amplitude-decaying inertial oscillation with period $2\pi/f$ with an orientation in the horizontal plane that oscillates with the inertial period. Equation (3.11) together

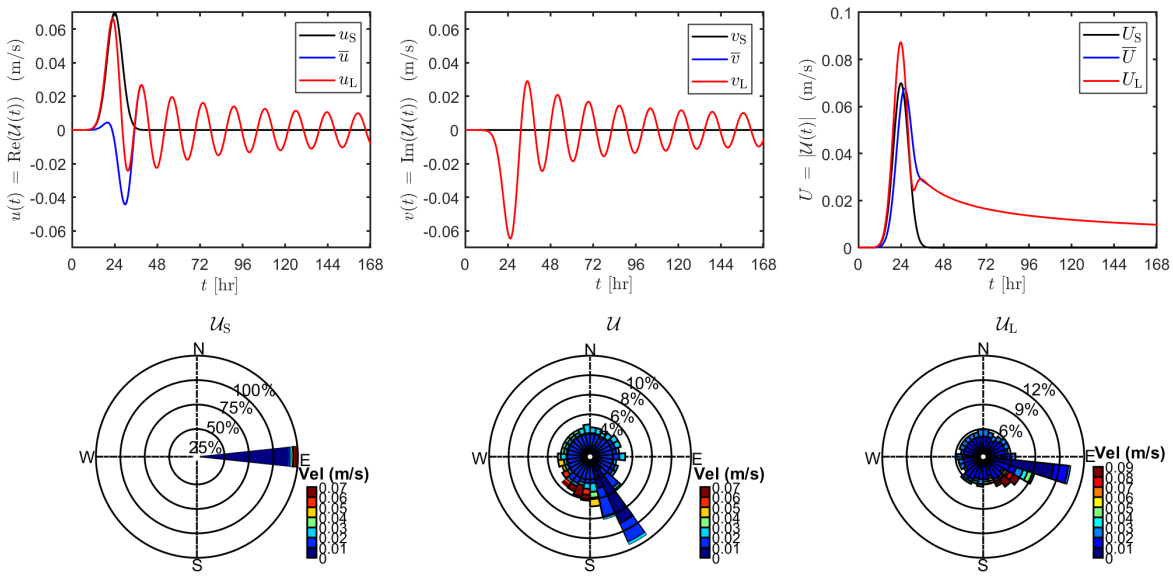

Figure 3.2: Top: Time series of wave-induced velocities formed in response to an idealised 24-hr Gaussian storm in the Northern Hemisphere showing the two components and magnitude of the Stokes drift $\mathcal{U}_S$ (black), Eulerian-mean velocity $\mathcal{U}$ (blue) and Lagrangian velocity $\mathcal{U}_L$ (red). **Bottom:** Wave roses for $\mathcal{U}_S$, $\mathcal{U}$, and $\mathcal{U}_L$, with radial distance representing the fraction of time during which the velocity has a given direction, and colour indicating magnitude in m/s.

with the convolution in time (3.8) is the key result of this letter. Taking as inputs a time series of Stokes drift and estimates of the peak wavenumber k, Coriolis parameter f and turbulent viscosity ν, these equations produce a time series of the associated (Eulerian-mean) Ekman–Stokes current at any vertical elevation z, which can simply be added to the Stokes drift time series to give the Lagrangian-mean current relevant for marine litter transport.

3.3 Sample calculations of the Ekman–Stokes flow

3.3.1 Idealised storm

To demonstrate the use of the Ekman–Stokes kernel, we calculate the Eulerian response to an idealised Gaussian storm lasting approximately 24 hours. Specifically, we set $u_S(z = 0) = u_S^* \exp(-(t - t^*)^2/(\sigma^2))$ (and $v_S = 0$) with $\sigma = 6$ hrs and magnitude $u_S^* = 0.070$ m/s being reached at $t^* = 24$ hrs. Choosing $f = 1.0 \times 10^{-4}$

s^{-1} and $\nu = 1.0 \times 10^{-2}$ $m^2 s^{-1}$ ($D = 1.1$), we set $\mathcal{U}(z = 0, t = 0) = 0$ and evaluate the response for 1 week.

In figure 3.2 we plot the u and v components and magnitudes, respectively, of the second-order currents over a week-long period. The sum of Stokes drift (black) and Ekman–Stokes flow (blue) gives the Lagrangian velocity (red). Beneath, wave roses are plotted for these second-order currents. The angular direction corresponds to the angle of propagation of the flow (separated into 30 bins), the radius of each bar represents the percentage of time during which the velocity has a given direction, and the colour scale divides the data into velocity amplitude ranges. Fig. 3.2 shows that the Stokes drift is reduced by a (delayed) partial 'anti-Stokes' flow, a transverse component arises on the same time scale, and damped inertial oscillations are formed which remain after the storm has ceased. The resulting Lagrangian current is deflected by the large transverse component of the Ekman-Stokes flow, to the right in the Northern Hemisphere (and to the left in the Southern Hemisphere).

3.3.2 Buoy data

We use half-hourly records for the San Nicolas Island buoy (33.22° N, 119.88° W) obtained from CDIP (the Coastal Data Information Project) and estimate the Stokes drift using the formula

$$\mathcal{U}_{\mathrm{s}} = g^{-1}\omega_p^3 A_p^2 \exp(2\overline{k}z)\exp\left(i\theta_p\right), \text{ where } A_p = H_{\mathrm{s}}/\left(2\sqrt{2}\right). \tag{3.13}$$

where θ_p is the peak wave direction, H_s the significant wave height, and ω_p the peak frequency calculated from the peak period T_p. By making a quasi-monochromatic approximation, we assume the wavenumber spectrum is peaked about $k = \mathrm{mean}(k_p) = \mathrm{mean}(\omega_p^2/g)$, to leading order. We integrate (3.11) using the Stokes drift (3.13) by a trapezoidal rule with time-step equal to the buoy sampling time. From the short-time limit in table 3.1, it can be seen that $\lim_{t\to 0^+}\lim_{z\to 0^-} K(z,t) = \infty - if$. To avoid this singular behaviour, we evaluate the surface value of the kernel $K(0,0)$ with the limits in the reverse order, $\lim_{z\to 0^-}\lim_{t\to 0^+} K(z,t) = -if$.

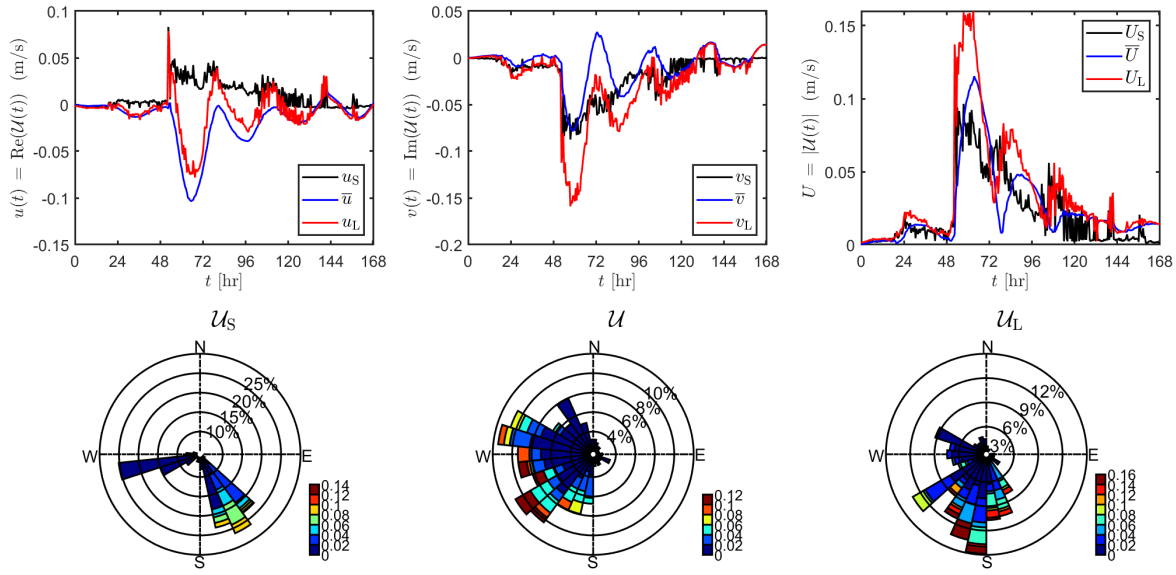

Figure 3.3: Top: Time series (14/05/00 15:41 – 22/05/00 09:41 UTC) of wave-induced velocities computed from buoy data from San Nicolas Island (33.22° N, 119.88° W), with colours as in Fig. 3.2. **Bottom:** Corresponding wave roses, as in Fig. 3.2.

As in figure 3.2, the top panels of figure 3.3 show u and v components and magnitudes of the second-order currents. The largest Stokes drift at San Nicolas Island over this time period is in a South-Southeasterly direction, though a share of very small values arising from small-amplitude waves are also seen to propagate West-Southwest (cf. bottom-left panel, figure 3.3). In contrast, the Ekman–Stokes contribution is much more directionally-spread at all velocity amplitudes due to excited inertial oscillations. Superimposing the two flows leads to a directionally-spread Lagrangian drift which veers to the right of the Stokes drift.

To find the displacement associated with the unsteady flows, we take the wavenumber and Stokes drift time series to be uniform in space, which is valid for the relatively small accumulated displacements considered. Particle displacements computed by time-integrating the velocities obtained from our Ekman–Stokes kernel are plotted in figure 3.4. Panels (a) and (c) show displacements over one week in February 2003 and (b) and (d) over a week in May 2000, with (*b*) corresponding to velocities plotted in figure 3.3. Line colours are consistent with figures 3.2 and

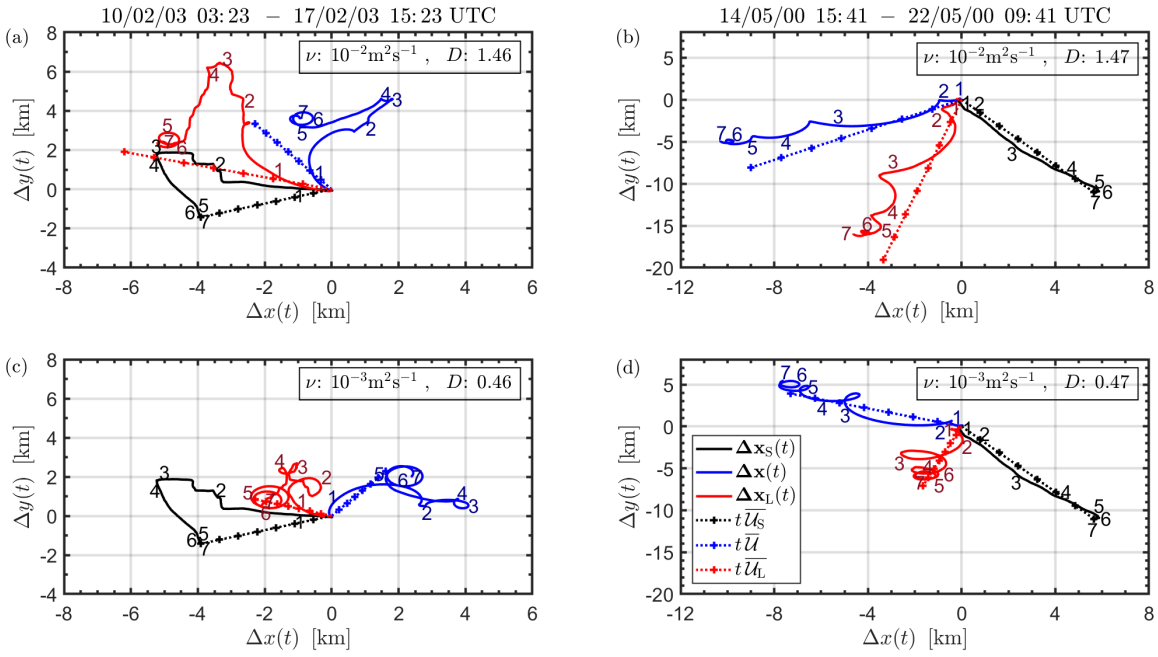

Figure 3.4: Particle paths at the surface ($z = 0$) computed for the San Nicolas Island buoy using our Ekman–Stokes convolution kernel. **Columns:** two different time samples. **Rows:** different values of turbulent viscosity. Paths shown are obtained using the Stokes drift (black), Eulerian-mean velocity (blue) and Lagrangian-mean velocity (red). Dashed lines ignore time-dependence of the Stokes drift and show the steady response to the average of the Stokes drift over the periods considered. All paths begin at $(\Delta x, \Delta y) = (0, 0)$. Numbers beside each line denote the number of days elapsed.

3.3. Straight dotted lines represent steady solutions, i.e. (3.7) multiplied by time elapsed, with $\overline{\mathcal{U}_S} = \text{mean}\,(\mathcal{U}_S)$. Evidently, the steady approximation causes errors in the prediction of net particle displacement. Instead of following the black trajectory described by the Stokes drift alone, we predict the particle will follow the red trajectory, being transported by the Lagrangian velocity, the sum of the Stokes drift and wave-induced Ekman–Stokes flow. For both time samples, the Lagrangian displacement is to the right of the Stokes displacement, as for the velocities (in the Southern Hemisphere, it will lie to the left).

We anticipate that the realistic range for eddy viscosity is $O(10^{-3})$-$O(10^{-2})$ m^2s^{-1}, estimated from the vertical mixing coefficient $S_M = 0.30$ in Mellor and Blumberg (2004) by using the law of the wall. Comparing (c) and (d) with (a) and (b), particle displacement is reduced and inertial oscillations more pronounced for the smaller viscosity $\nu = 10^{-3}\text{m}^2\text{s}^{-1}$ in (c) and (d), since the anti-Stokes flow

increases in magnitude as viscosity decreases. For the realistic range of ν the displacement is significantly altered in both magnitude and direction when the Ekman–Stokes flow is included.

3.4 Discussion and conclusions

Our analysis has demonstrated the need to add a so-called Ekman–Stokes flow to the Stokes drift to properly estimate the wave-induced Lagrangian-mean flow which transports floating marine litter. We have derived an Ekman–Stokes convolution kernel which can readily be used to predict the wave-induced Eulerian-mean flow in the turbulent upper-ocean boundary layer. It integrates three important effects: the surface wave stress, the Coriolis–Stokes forcing, and unsteadiness of the forcing and response.

We properly account for the viscous wave stress at the surface. This is often neglected (e.g. Lewis and Belcher (2004), Polton et al. (2005), and Onink et al. (2019)), though it may be of similar magnitude to the wind stress. Including the wave stress should yield more accurate predictions of the Lagrangian drift, particularly when wind and waves are misaligned. Our model also incorporates the Coriolis–Stokes forcing which induces a partial anti-Stokes flow and alters the response over the Ekman depth $\delta_{\mathrm{E}} = \sqrt{2\nu/f}$ (cf. Polton et al. (2005)). Our results demonstrate that for realistic eddy viscosities 10^{-3}–$10^{-2}\,\mathrm{m^2 s^{-1}}$ the Stokes drift is only partially cancelled by an anti-Stokes flow. Perhaps most importantly, our approach shows that unsteadiness of the Stokes drift and induced Eulerian response can be readily incorporated into models of Lagrangian drift using a simple convolution. As passage times of storms are typically $O(1/f)$, accounting for time variability is crucial for accurate predictions of drift.

Future work should improve our model in the following four ways. First, for simplicity we have assumed a constant eddy viscosity, although our kernel approach could be adapted for linearly-increasing eddy viscosity (Madsen (1977), Lewis and Belcher (2004)), which provides a more accurate representation of turbulence in the upper-ocean boundary layer. Second, Shrira and Almelah (2020) have

presented a solution method incorporating time-dependence of the eddy viscosity due to processes such as mixed-layer restratification or wave breaking (Price and Sundermeyer, 1999). Parameterisations of turbulent viscosity should thus account for both time and depth variation.

Third, while we have used a quasi-monochromatic assumption in our model, the Ekman–Stokes kernel can in principle be applied to broad-banded spectra using an additional integration over frequency. For typical broad-banded spectra, the near-surface Stokes drift is more strongly sheared than for a monochromatic wave corresponding to the peak frequency (Webb and Fox-Kemper, 2011). Therefore, the wave stress dominates the forcing of the Eulerian-mean flow whose magnitude is strengthened and whose direction becomes more aligned with that of the Stokes drift, as we have confirmed in preliminary computations. We emphasise that the wave stress is proportional to the fifth moment of the frequency spectrum and hence ill-defined for most empirical spectra, whose high-frequency tails behave like ω^{-4} or ω^{-5} (Breivik, Bidlot, et al., 2016). This indicates a high sensitivity of the wave-induced mean flow to the spectral tail, suggesting the need for a careful assessment of the form of this tail and of its impact on the Eulerian-mean dynamics. We note that Seshasayanan and Gallet (2019) recently showed that the steady Ekman–Stokes current is unstable to perturbations. Future work should consider the importance of this instability in the real ocean and how it might interact with unsteadiness of the wave-induced flow.

Fourth, ocean transport can be modelled using the tracer equation rather than Lagrangian tracking methods (Dobler et al., 2019; Wu et al., 2019). Stokes advection plays an important role in strong wind/wave conditions, and affects up/down-welling in coastal regions (Suzuki and Fox-Kemper, 2016; Wu et al., 2019). We anticipate that including the unsteady Ekman–Stokes flow will cause variations in up/down-welling velocities over timescales $\gtrsim O(1/f)$ (§4(i) Hasselmann (1970) and McWilliams and Restrepo (1999))

Chapter 4
Ekman–Stokes pumping

Abstract

In (Higgins, Vanneste, et al., 2020), published in Geophysical Research Letters, an expression was derived for the unsteady Ekman–Stokes flow driven by a time-varying surface gravity wave field in the turbulent upper layer of a rotating ocean. This wave-induced Eulerian-mean flow is given by a convolution between the surface Stokes drift and an Ekman–Stokes kernel, which encodes information about the evolution of the flow throughout the Ekman depth. Together with the Stokes drift, the Ekman–Stokes flow constitutes the leading-order Lagrangian-mean flow induced by the surface waves. In this chapter, I examine the higher-order Eulerian-mean flows which arise due to the slow spatial variation of the wave field which was neglected in Higgins, Vanneste, et al. (2020). By taking advantage of the shallowness of the Ekman–Stokes layer with respect to the ocean depth, I apply boundary-layer methods to explore these divergence-driven Eulerian-mean flows. Spatial variation of the horizontal Ekman–Stokes flow drives a weak, 'Ekman–Stokes pumping' vertical velocity in the upper layer, resulting in wave-induced downwelling (upwelling) in regions of wave convergence (divergence). By matching the pumping velocity at the base of the Ekman–Stokes layer to a weak Eulerian flow beneath it, I derive an effective boundary condition which directly links the surface Stokes drift to a divergence-driven return flow experienced at depth. The effect of rotation on an unstratified, wavepacket-driven return flow is almost negligible, but weak rotation can have a significant impact when combined with density stratification, resulting in radiation of inertia-gravity waves in the packet's wake. Though the analysis presented here focusses on a single nondissipating wavepacket, I show that the combination of Coriolis effects and spatial divergence of the wave field may be significant over synoptic scales.

4.1 Introduction

Hasselmann (1970) demonstrated that the Coriolis force puts the linear velocity components of surface waves out of quadrature, resulting in a stress perpendicular to the direction of wave propagation. This Coriolis–Stokes forcing induces an Eulerian-mean flow which cancels the Stokes drift and excites inertial oscillations. In the presence of turbulent viscosity, this anti-Stokes flow does not exactly cancel the Stokes drift, and the wave-induced Lagrangian velocity - the sum of the Stokes drift and Eulerian-mean flow - is nonzero. The steady-state Ekman–Stokes flow was recently examined in Seshasayanan and Gallet (2019) and extended to unsteady wave fields by Higgins, Vanneste, et al. (2020), who found that it significantly affects the magnitude and direction of marine litter transport by waves. The unsteady Ekman–Stokes flow is computed by convolving the time-varying surface Stokes drift with an 'Ekman–Stokes kernel', which describes the development of the flow over the depth of the turbulent upper layer of the ocean.

There is growing interest in including the effects of surface waves in general ocean circulation models, either by coupling a third-generation wave model such as WAM (The WAMDI Group, 1988) to a circulation model, or by directly including wave-induced effects such as the Coriolis–Stokes forcing in the momentum and tracer advection equations (Breivik, Mogensen, et al., 2015). A seminal paper by McWilliams and Restrepo (1999) examines how surface waves affect the basin-scale ocean circulation. The authors find that waves modify the classical Sverdrup relation, with impact on the deep circulation. However, their analysis does not account for wave-induced Eulerian-mean currents which are driven by the virtual wave stress (Seshasayanan and Gallet, 2019), and/or by the slow-scale spatial variation of the wave field (van den Bremer and Taylor, 2015). This leads McWilliams and Restrepo (1999) to conclude that waves have no influence on the Ekman pumping velocity.

By running an ocean general circulation model with sea-state dependent parameters and momentum fluxes estimated from WAM (The WAMDI Group, 1988), Wu et al. (2019) determine that including wave effects improves agreement between the model predictions of upwelling and observations in the North Sea. In particular,

advection by the Stokes drift must be included in the tracer advection equation in order to counteract unphysical coastal upwelling/downwelling by the Coriolis–Stokes forcing (Breivik, Mogensen, et al., 2015). The authors argue that the low-frequency swell is likely to have a more significant impact on upwelling than the local wind sea, since remotely-generated swell is generally not aligned with the wind.

Examining the propagation of a surface gravity wavepacket over a stratified ocean, Haney and Young (2017) find that the Eulerian return flow induced by the packet disturbs the surfaces of constant density, generating internal waves in the wake of the packet. Using Fourier modes in the vertical, Haney and Young (2017) examine the energy flux from the surface wavepacket to the internal-wave wake, finding this to be extremely small. However, extreme surface-wave forcing, such as might be generated by a strong storm, may contribute to the near-N peak in the inertia-gravity wave spectrum (Haney and Young, 2017).

In this chapter, I combine the effects of spatial variation of the surface wave field with Ekman–Stokes dynamics in order to examine the second-order in steepness flows induced by deep water surface gravity waves. In so doing, the analysis of Higgins, van den Bremer, et al. (2020) and Higgins, Vanneste, et al. (2020) is integrated into a single model which takes account of the turbulent upper layer of the ocean, the Earth's rotation, spatial variation of the wave field, and density stratification.

4.2 Governing equations

I consider an ocean locally described by a Cartesian coordinate system with x measured positive Eastwards, y positive Northwards and z the vertical coordinate measured from the free surface upwards. Incompressible flow is assumed in a rotating, density-stratified ocean with a turbulent upper layer which can be parametrised using an effective eddy viscosity. To account for stratification effects, I decompose the density as $\rho\left(x,y,z,t\right)=\rho_0\left(1+g^{-1}\int_z^0 N^2(z')dz'-g^{-1}b\right)$: that is, a constant density plus a mean z-dependent stratification profile described by the stratification

frequency N, plus a small buoyancy perturbation b. The governing equations in the interior of the fluid $-d \leq z < \zeta\,(x, y, t)$ are given by

$$\partial_t \boldsymbol{u} + \boldsymbol{u}\cdot\boldsymbol{\nabla}\boldsymbol{u} + \boldsymbol{f}\times\boldsymbol{u} + \boldsymbol{\nabla}p - \boldsymbol{\nabla}\cdot\overleftrightarrow{\boldsymbol{\tau}} - b\hat{\boldsymbol{z}} = \boldsymbol{0}, \quad \partial_t b + \boldsymbol{u}_{\rm H}\cdot\boldsymbol{\nabla}_{\rm H} b + wN^2, \quad \boldsymbol{\nabla}\cdot\boldsymbol{u} = 0 \tag{4.1a,b,c}$$

with $\overleftrightarrow{\boldsymbol{\tau}}$ the viscous stress tensor with elements $\tau_{ij} = -(p - p_0)\delta_{ij} + \nu\,(\partial_j u_i + \partial_i u_j)$ where ν is an eddy viscosity, p the pressure, and $\boldsymbol{f} = (0, \tilde{f}, f)$ the (nontraditional) Coriolis vector. These equations must be solved subject to kinematic and dynamic boundary conditions at the free surface $z = \zeta(x, y, t)$, plus a no-flow bottom boundary condition at the ocean floor

$$w|_{z=\eta} = \partial_t\zeta + \boldsymbol{u}\cdot\boldsymbol{\nabla}\zeta, \quad \hat{\boldsymbol{n}}\cdot\overleftrightarrow{\boldsymbol{\tau}}\cdot\hat{\boldsymbol{s}}|_{z=\zeta} = 0, \quad w|_{z=-d} = 0, \tag{4.2a,b,c}$$

where $\hat{\boldsymbol{n}}$ and $\hat{\boldsymbol{s}}$ are unit vectors normal and tangent to the free surface, respectively. To solve the system (4.1) subject to (4.2), I use a Stokes expansion in wave steepness $\alpha \equiv A_p k_p$, where A_p is the maximum amplitude of the free surface and k_p the peak wavenumber in the wavenumber spectrum,

$$\boldsymbol{u} = \boldsymbol{u}_1 + \boldsymbol{u}_2 + O(\alpha^3), \quad \zeta = \zeta_1 + \zeta_2 + O(\alpha^3), \quad p = p_1 + p_2 + O(\alpha^3), \quad b = b_1 + b_2 + O(\alpha^3), \tag{4.3}$$

and the subscript denotes the order in α. I first consider the linear problem.

4.2.1 Linear dynamics

Linear wave dynamics arises at $O(\alpha)$, where I ignore viscous effects, neglecting a thin vorticity boundary layer of thickness $\delta_\nu = \sqrt{2\nu/\omega}$ under the (generally satisfied) assumption $|\boldsymbol{k}_p|\delta_\nu \ll 1$ where $\boldsymbol{k}_p = (k, l)$ is the peak wavenumber. Consequently, I ignore viscous damping of waves as they propagate. I assume deep-water waves for which $|\boldsymbol{k}_p|d \gg 1$. The linear equations then read

$$\partial_t\boldsymbol{u}_1 + \boldsymbol{f}\times\boldsymbol{u}_1 + \boldsymbol{\nabla}p_1 = \boldsymbol{0}, \quad \boldsymbol{\nabla}\cdot\boldsymbol{u}_1 = 0, \quad w_1|_{z=0} = \partial_t\zeta_1, \quad p_1|_{z=0} = g\zeta_1, \tag{4.4a,b,c,d}$$

where the linear buoyancy $b_1 = O(N^2\zeta_1)$ has been neglected, which amounts to discarding $O(N^2/\omega^2)$ corrections to the dispersion relation. Since these corrections

do not alter the phase relationships between the linear variables, and hence do not affect the wave-averaged Reynolds stresses at second order in wave steepness, this is a reasonable approximation (cf. Haney and Young (2017) and Higgins, Vanneste, et al. (2020)). In contrast, the Coriolis force must be retained since, as demonstrated by Hasselmann (1970), $O(f/\omega)$ corrections put horizontal and vertical velocity components out of quadrature, with impact on the wave-averaged dynamics.

Expanding the surface boundary conditions (4.2a,b) about the undisturbed level $z = 0$ to second-order in wave steepness results in the two boundary conditions

$$w_2|_{z=0} = \partial_t \zeta_2 + \boldsymbol{\nabla}_{\mathrm{H}} \cdot \overline{(\boldsymbol{u}_1 \zeta_1)}, \qquad \nu \partial_z \mathcal{U}|_{z=0} = \nu \partial_z \mathcal{U}_{\mathrm{S}}, \tag{4.5a,b}$$

where the stress condition (4.5b) drives the horizontal Ekman–Stokes flow $\mathcal{U} = u_2 + iv_2$ with $\mathcal{U}_{\mathrm{S}} = u_{\mathrm{S}} + iv_{\mathrm{S}}$, and (4.5a) in conjunction with incompressibility governs the weaker Ekman–Stokes pumping velocity w_2. To leading order in the bandwidth-like parameter $\varepsilon \sim (2k_p\sigma_x)^{-1}$, where σ_x is the scale of horizontal variation of the wave envelope, the divergence term can be identified with the Stokes mass transport,

$$\overline{(\boldsymbol{u}_1 \zeta_1)} = \mathbf{M}_{\mathrm{S}} = \int_{-\infty}^{0} \boldsymbol{u}_{\mathrm{S}} dz. \tag{4.6}$$

I use the 'rigid-lid' approximation, which assumes the free surface appears locally flat with respect to the induced Eulerian-mean flow, to neglect $\partial_t \zeta_2$. This formally precludes any shallow-water solutions with $c = \sqrt{gd}$, which is valid for the deep-water conditions considered herein. The term $\overline{\boldsymbol{u}_1 \cdot \boldsymbol{\nabla} \boldsymbol{u}_1} = \overline{|\boldsymbol{u}_1|^2/2} - \overline{\boldsymbol{u}_1 \times (\boldsymbol{\nabla} \times \boldsymbol{u}_1)}$ may also be simplified using the linear solutions. Corrections of $O(f/\omega)$ to the linear velocity field result in a small vorticity $\boldsymbol{\omega}_1 = \boldsymbol{\nabla} \times \boldsymbol{u}_1$, which gives rise to the so-called Coriolis-Stokes forcing on the second-order mean flow,

$$\overline{\boldsymbol{u}_1 \cdot \boldsymbol{\nabla} \boldsymbol{u}_1} = \overline{|\boldsymbol{u}_1|^2/2} + \boldsymbol{f} \times \boldsymbol{u}_{\mathrm{S}}. \tag{4.7}$$

In an inviscid ocean, the Coriolis–Stokes forcing results in an Eulerian-mean flow at second order in wave steepness which cancels the Stokes drift and excites inertial oscillations (Hasselmann, 1970).

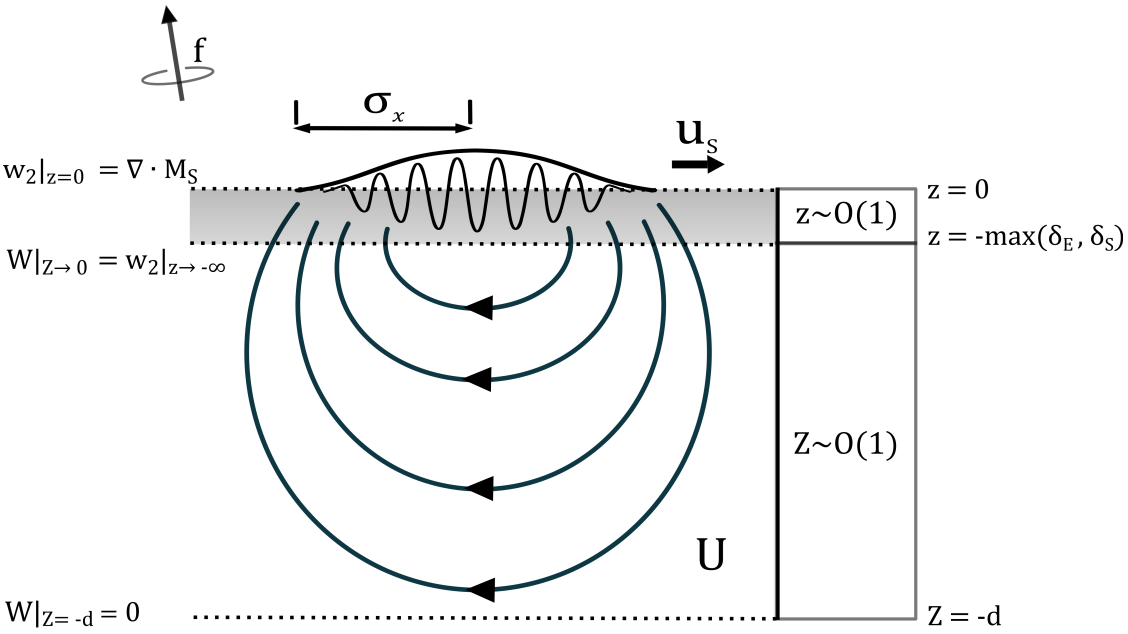

Figure 4.1: Boundary-layer method for a wavepacket: viscous effects and Coriolis–Stokes forcing are important over the Ekman depth $\delta_{\mathrm{E}} \sim \sqrt{\nu/f}$ and the Stokes depth $\delta_{\mathrm{S}} \sim k_p^{-1}$. Spatial variation of the wave field over a scale σ drives a weak Ekman–Stokes pumping velocity w_2 in this layer, varying vertically over the 'fast' vertical coordinate z. In turn, this pumping provides a boundary condition applied at the base of the boundary layer to the deep return flow $\boldsymbol{U}$ beneath, which varies over the 'slow' outer coordinate Z.

4.3 Boundary-layer method for the mean flow

In the near-surface Ekman–Stokes layer, eddy viscosity and Coriolis rotation define the Ekman lengthscale $\delta_{\mathrm{E}} \sim \sqrt{\nu/f}$, and the Coriolis-Stokes forcing is distributed over the Stokes depth $\delta_{\mathrm{S}} \sim (k_p)^{-1}$, which is deeper than the Ekman depth for quasi-monochromatic swell with $T_p > 11$ s. Large-scale variations in the wave field define another scale σ_x on which spatial variation of the wave field occurs, which is typically much larger than δ_{S} and δ_{E}. Provided $\sigma_x \gg \delta_{\mathrm{E\text{-}S}} = \max(\delta_{\mathrm{E}}, \delta_{\mathrm{S}})$ and the wave field consists of deep-water waves, a boundary-layer approach can be applied to the problem. Without loss of generality, I define an 'inner' vertical coordinate z (of scale $\delta_{\mathrm{E\text{-}S}} = \max(\delta_{\mathrm{E}}, \delta_{\mathrm{S}})$), upon which the Ekman–Stokes flow varies, and an 'outer' coordinate Z (of scale σ) upon which the divergence-driven return flow in the outer layer varies. This allows simplified equations to be solved in the upper layer, where viscosity and Coriolis–Stokes forcing are important and horizontal derivatives are negligible, and hence a modified boundary condition to be derived

which governs the deep flow beneath this layer. In the outer layer, stratification, rotation and spatial variation are important.

4.3.1 Dynamics in the upper layer

The wave-averaged Eulerian velocity $\overline{\boldsymbol{u}}$ in the upper layer obeys the Craik–Leibovich equations with buoyancy (Craik and Leibovich, 1976)

$$\partial_t\overline{\boldsymbol{u}}+(\boldsymbol{\nabla}\times\overline{\boldsymbol{u}}+\boldsymbol{f})\times\overline{\boldsymbol{u}_{\mathrm{L}}}+\boldsymbol{\nabla}\left(p+\frac{1}{2}|\overline{\boldsymbol{u}_{\mathrm{L}}}|^2\right)-\boldsymbol{\nabla}\cdot\overleftrightarrow{\boldsymbol{\tau}}=\bar{b}\hat{\boldsymbol{z}},\quad \partial_t\bar{b}=-\overline{\boldsymbol{u}_1\cdot\boldsymbol{\nabla}b_1}-\overline{w}N^2, \tag{4.8}$$

where p is the pressure divided by the constant reference density ρ_0, and an overbar denotes averaging over the wave phase. The total Eulerian-mean flow $\overline{\boldsymbol{u}}=\boldsymbol{u}_2+\boldsymbol{u}_{\mathrm{B}}$ is the sum of the wave-induced Eulerian flow $\boldsymbol{u}_2$ and the non-wave Eulerian background flow $\boldsymbol{u}_{\mathrm{B}}$. This permits the Lagrangian current $\overline{\boldsymbol{u}_{\mathrm{L}}}=\overline{\boldsymbol{u}}+\boldsymbol{u}_{\mathrm{S}}=\boldsymbol{u}_{\mathrm{L}}+\boldsymbol{u}_{\mathrm{B}}$ to be decomposed as the sum of the wave-induced Lagrangian velocity $\boldsymbol{u}_{\mathrm{L}}=\boldsymbol{u}_2+\boldsymbol{u}_{\mathrm{S}}$ and the non-wave Eulerian background flow $\boldsymbol{u}_{\mathrm{B}}$.

When the background flow has a small Rossby number, $(\boldsymbol{\nabla}\times\boldsymbol{u}_{\mathrm{B}})\times\overline{\boldsymbol{u}_{\mathrm{L}}}$ is negligible compared with the Coriolis terms. Under the small Rossby-number assumption, the background flow decouples from the wave-induced flow, and the interaction between these may be neglected. Since b_1 has been neglected in the linear calculations, $\bar{b}=-\int\overline{w}N^2dt$. The incompressibility condition implies that the vertical velocity is weaker than the horizontal Ekman–Stokes velocities by a bandwidth parameter $\varepsilon=(2k_p\sigma_x)\ll 1$, and therefore the effects of buoyancy in the Ekman–Stokes layer can be ignored. Having made this set of approximations, the governing equations are the ones solved in Chapter 3 which give rise to unsteady Ekman–Stokes dynamics (Higgins, Vanneste, et al., 2020), namely

$$\partial_t\boldsymbol{u}_2+\boldsymbol{f}\times\boldsymbol{u}_{\mathrm{L}}+\boldsymbol{\nabla}p-\boldsymbol{\nabla}\cdot\overleftrightarrow{\boldsymbol{\tau}}=\boldsymbol{0}+O(\alpha^4), \tag{4.9}$$

where the Stokes vortex force, $(\boldsymbol{\nabla}\times\boldsymbol{u}_2)\times\boldsymbol{u}_{\mathrm{L}}$, is $O(\alpha^4)$ since it involves only the wave-induced flow. The wave-induced flow may then be superimposed on the background to obtain the correct mass-transport velocity at $O(\alpha^2\varepsilon^0)$. From Higgins,

Vanneste, et al. (2020), the expression for the Eulerian-mean Ekman–Stokes velocity in convolution form is given by

$$\mathcal{U}(\boldsymbol{x}, z, t) = \int_0^t \mathcal{U}_{\mathrm{S}}\left(\boldsymbol{x}, t'\right)|_{z=0} K\left(z\,,\, t - t'\right) dt', \tag{4.10}$$

where $\mathcal{U} = u_2 + iv_2$ and $\mathcal{U}_{\mathrm{S}} = u_{\mathrm{S}} + iv_{\mathrm{S}}$, and $K(z,t)$ is the Ekman–Stokes kernel which encodes information about the development of $\mathcal{U}$ in the Ekman–Stokes layer over time. The kernel is a function of z and t only; the Eulerian flow inherits its spatial dependence parametrically from the surface Stokes drift field, via the wave stress condition (4.5b). Incompressibility of the Ekman–Stokes flow indicates that a weak vertical velocity arises when the Stokes drift varies horizontally,

$$\partial_x u_2 + \partial_y v_2 + \partial_z w_2 = 0 \quad \Leftrightarrow \quad \partial_z w_2 = -\operatorname{Re}\left[\partial_- \mathcal{U}\right] = -\boldsymbol{\nabla}_{\mathrm{H}} \cdot \boldsymbol{u}_2. \tag{4.11}$$

Here I have defined the rotary gradient $\partial_\pm = \partial_x \pm i\partial_y$ and the horizontal gradient $\boldsymbol{\nabla}_{\mathrm{H}} = (\partial_x, \partial_y, 0)$ to make a connection with the complex notation used in (4.10). This gives the vertical velocity, which is weaker than the horizontal Ekman–Stokes velocities by an aspect ratio parameter $\varepsilon = (2k_p\sigma_x)^{-1}$, where σ_x is the scale on which the wave field varies spatially and k_p is the peak wavenumber,

$$w_2(z) = \int_z^0 \left(\boldsymbol{\nabla}_{\mathrm{H}} \cdot \boldsymbol{u}_2\right) dz + \boldsymbol{\nabla}_{\mathrm{H}} \cdot \mathbf{M}_{\mathrm{S}}. \tag{4.12}$$

where the $O(\alpha^2\varepsilon^1)$ dynamic boundary condition (4.5a) was used. The rigid-lid approximation has also been made, so $\partial_t\zeta_2$ is neglected. Taking the limit $z/\delta_{\text{E-S}} \to -\infty$ results in a matching condition between the vertical components w_2 and W of the inner and outer flow, respectively,

$$\lim_{Z/\sigma_x \to 0^-} W = \lim_{z/\delta_{\text{E-S}} \to -\infty} w_2 = \int_{-\infty}^0 \left(\boldsymbol{\nabla}_{\mathrm{H}} \cdot \boldsymbol{u}_{\mathrm{L}}\right) dz = \boldsymbol{\nabla}_{\mathrm{H}} \cdot \mathbf{M}_{\mathrm{L}} \tag{4.13}$$

where $\mathbf{M}_{\mathrm{L}} = \mathbf{M} + \mathbf{M}_{\mathrm{S}}$ and $\mathbf{M} = \int_{-\infty}^0 \boldsymbol{u}_2 dz$ is the mass-transport driven by the Ekman–Stokes flow. Hence the outer flow is forced by the divergence of the Lagrangian mass transport over the upper layer. A formula for $\mathbf{M}$ in terms of $\mathcal{U}_{\mathrm{S}}$ can be obtained directly from the Ekman-Stokes equations, which read

$$\partial_t \mathcal{U} + if\mathcal{U} = -if\mathcal{U}_{\mathrm{S}} + \partial_z\left(\nu\partial_z\mathcal{U}\right), \quad \partial_z\mathcal{U}|_{z=0} = \partial_z\mathcal{U}_{\mathrm{S}}, \quad \lim_{z\to-\infty}\mathcal{U} = 0. \tag{4.14a,b,c}$$

Depth-integrating, defining the complex mass transports $\mathcal{M} = \int_{-\infty}^{0} \mathcal{U} dz$ and $\mathcal{M}_{\mathrm{S}} = \int_{-\infty}^{0} \mathcal{U}_{\mathrm{S}} dz$, and applying the boundary conditions (assuming that $\nu \partial_z \mathcal{U} \to 0$ at depth)

$$(\partial_t + if)\,\mathcal{M} = -if\mathcal{M}_{\mathrm{S}} + \nu \partial_z \mathcal{U}_{\mathrm{S}}|_{z=0}. \tag{4.15}$$

For a monochromatic Stokes drift profile, $\mathcal{M}_{\mathrm{S}} = \mathcal{U}_{\mathrm{S}}(\boldsymbol{x}, t, z)|_{z=0}/(2k_p)$. Using the integrating factor method, and assuming the Ekman–Stokes mass transport is initially zero, the (complex) Ekman–Stokes transport is given by the simple convolution integral

$$\mathcal{M} = \left(2k_p \nu|_{z=0} - \frac{if}{2k_p}\right) \int_0^t \mathcal{U}_{\mathrm{S}}(\boldsymbol{x}, t') e^{-if(t-t')} dt', \tag{4.16}$$

where $\nu|_{z=0}$ is the surface value of the eddy viscosity, which is in general a function of z. As a special case, I consider the steady solution to (4.15). In the inviscid analysis of Hasselmann (1970), a steady solution exists only in the sense of an inertial average, but Madsen (1978) showed that when viscosity is introduced into the problem, a steady-state is established as a result of balance between the Earth's rotation and viscous shear in the Ekman–Stokes layer,

$$\overline{\mathcal{M}} = -\overline{\mathcal{M}_{\mathrm{S}}} - i\frac{\nu_0}{f}\overline{\partial_z \mathcal{U}_{\mathrm{S}}}|_{z=0}, \quad \overline{w_2} = \boldsymbol{\nabla}_{\mathrm{H}} \cdot \overline{\mathbf{M}_{\mathrm{L}}} = \nu_0 \frac{(\partial_x \partial_z v_{\mathrm{S}} - \partial_y \partial_z u_{\mathrm{S}})}{f} = \frac{\hat{\boldsymbol{z}} \cdot \boldsymbol{\nabla} \times (\nu_0 \partial_z \boldsymbol{u}_{\mathrm{S}}|_{z=0})}{f}, \tag{4.17}$$

where $\nu_0 = \nu|_{z=0}$, so the steady pumping velocity at the base of the mixed layer $\overline{w_2}(-\infty)$ is proportional to the curl of the surface wave stress, entirely analogous to how classical Ekman pumping is related to the curl of the wind stress (McWilliams and Restrepo, 1999). This relationship should remain true for any quasi-monochromatic $\mathcal{U}_{\mathrm{S}}$, and is independent of the eddy viscosity depth profile (a surface roughness lengthscale is required for a linearly increasing $\nu(z)$, for example, since otherwise $\nu(0) = 0$). As with classical wind-driven Ekman pumping, there is also no need to compute $\mathcal{U}$ to obtain the Ekman-Stokes pumping velocity $\overline{w_2}$.

4.3.2 Dynamics in the outer layer

I assume that eddy viscosity is negligible in the outer layer. The mean flow is then driven by the pressure field, density stratification, Coriolis force, and the pumping boundary condition (4.13). Though there are no Stokes forces beneath the Ekman–Stokes layer, the small-Rossby number assumption must be invoked to neglect interaction between non-wave background flow and the $O(\alpha^2\varepsilon^1)$ return flow. Denoting the return flow by $\boldsymbol{U} = (U, V, W)$ and outer pressure by P,

$$\partial_t U - fV + \tilde{f}W = -\partial_x P, \quad \partial_t V + fU = -\partial_y P, \quad \partial_t W - \tilde{f}U = -\partial_Z P + b_2, \tag{4.18a,b,c}$$

$$\partial_t b_2 = -WN^2, \quad \partial_x U + \partial_y V = -\partial_Z W. \tag{4.19a,b}$$

Upon eliminating all variables other than the vertical velocity, the equation sets (4.18) and (4.19) become

$$\left[\partial_t^2 \Delta + N^2 \Delta_{\text{H}} + (\boldsymbol{f}\cdot\boldsymbol{\nabla})^2\right] W = 0, \quad \text{with b.c.s} \quad \lim_{Z\to 0^-} W = \boldsymbol{\nabla}_{\text{H}}\cdot\mathbf{M}_{\text{L}} \quad \text{and} \quad W|_{Z=-d} = 0. \tag{4.20}$$

For simplicity, vertical variation of N is neglected, while noting that (4.20) allows for more complex stratification profiles. Taking the curl yields the evolution of the Z-component of vorticity $\partial_t\left(\partial_x V - \partial_y U\right) = (\boldsymbol{f}\cdot\boldsymbol{\nabla})W$, which together with the incompressibility condition implies the horizontal velocities are related to W via a Poisson-like equation,

$$\partial_t\left(\partial_x^2 + \partial_y^2\right)\boldsymbol{U}_{\text{H}} = \left[\tilde{f}\partial_y \boldsymbol{\nabla}_{\text{H}}^{\perp} + \left(f\boldsymbol{\nabla}_{\text{H}}^{\perp} - \partial_t \boldsymbol{\nabla}_{\text{H}}\right)\partial_Z\right] W, \tag{4.21}$$

where $\boldsymbol{U}_{\text{H}} = (U, V, 0)$ and $\boldsymbol{\nabla}_{\text{H}}^{\perp} \equiv \hat{\boldsymbol{Z}} \times \boldsymbol{\nabla}_{\text{H}} = (-\partial_y, \partial_x, 0)$. Interestingly, this vector equation does not explicitly involve the buoyancy perturbation b or stratification frequency N. When rotation is ignored ($\boldsymbol{f} = \boldsymbol{0}$) (4.21) reduces to eqn. (2.39) in Chapter 2. Upon also setting $N = 0$, (4.21) is just $\partial_t \boldsymbol{\nabla}_{\text{H}}$ of the Laplace equation.

4.4 Application to a wavepacket

When the surface wavefield has packet-like structure, it is advantageous to use axes corresponding to the co-moving frame of the packet. I can locally choose the x-axis to be the direction of propagation, and define the co-moving coordinate $\tilde{x} = x - c_g t$. Equation (4.15) takes the form

$$(-c_g \partial_{\tilde{x}} + c_g \eta + if)\, \mathcal{M}(\tilde{x}, y) = \left(2k_p \nu_0 - \frac{if}{2k_p}\right) \mathcal{U}_{\mathrm{S}}|_{z=0}, \tag{4.22}$$

where $c_g \eta$ is a slow growth rate which ensures that the solution for $\mathcal{M}$ obeys the correct radiation condition. This equation can be solved by convolving the right-hand side forcing with a Green's function $\exp(ir\tilde{x})H(-\tilde{x})$, where $r = f/c_g$ is a rotational wavenumber and $H(-\tilde{x})$ is a Heaviside step function which results from the slow-growth causal limit $\eta \to 0^+$. The Heaviside function ensures that radiated inertial waves only appear in the wake of the packet. The Ekman–Stokes transport is

$$\mathcal{M}(\tilde{x}, y) = \left(\frac{2k_p \nu_0}{c_g} - \frac{ir}{2k_p}\right) \int_{\tilde{x}}^{\infty} \mathcal{U}_{\mathrm{S}}(\tilde{x}', y)\, e^{ir(\tilde{x} - \tilde{x}')} d\tilde{x}', \tag{4.23}$$

where $\tilde{x}'$ is just a dummy variable of integration. Note that taking $\mathcal{U}_{\mathrm{S}} =$ constant for $\nu_0 = 0$ results in an anti-Stokes Eulerian transport $\mathcal{M} = \mathcal{M}_{\mathrm{S}}$ plus an inertial oscillation, as found by Hasselmann (1970) for a regular wave train in an inviscid ocean. For illustrative purposes, I choose a Stokes drift which is Gaussian in the $\tilde{x}$-direction and modulated by an envelope function $G(y)$ in the y-direction, i.e. $\mathcal{U}_{\mathrm{S}} = \omega_p k_p A_p^2 \exp(-\tilde{x}^2/\sigma_x^2) G(y)$, which I also take to be Gaussian ($G(y) = \exp(-y^2/\sigma_y^2)$). The behaviour of the normalised, nondimensional Ekman–Stokes transport $\mathcal{M}^* = 2\mathcal{M}/(\omega_p |A_p|^2)$ depends on two dimensionless parameters,

$$r^* = f\sigma_x/c_g \quad \text{and} \quad \nu^* = 4k_p^2 \nu|_{z=0}\,(\sigma_x/c_g)\,. \tag{4.24a,b}$$

These parameters may be thought of as an inverse packet Rossby number ((4.24a)) and a ratio between the timescales of packet translation and viscous diffusion ((4.24b)). The integral (4.23) has a solution in terms of the Dawson function $D_+(x) = \exp(-x^2) \int_0^x \exp(t^2) dt$,

$$\mathcal{M}^*(\tilde{x}^*, y^*, R) = G(y^*, R)\,(\nu^* - ir^*) \left(\frac{\sqrt{\pi}}{2} e^{-(r^*)^2/4} e^{ir^*\tilde{x}^*} - ie^{-(\tilde{x}^*)^2} D_+\left(\frac{r^*}{2} - i\tilde{x}^*\right)\right), \tag{4.25}$$

where the narrow-bandedness parameter $\varepsilon = (2k_p\sigma_x)^{-1}$ as before, $(\tilde{x}^*, y^*) = (\tilde{x}, y)/\sigma_x$, and $R = \sigma_x/\sigma_y$ is the ratio between the characteristic packet lengthscales in $\tilde{x}$ and in y. Since (4.23) expresses $\mathcal{M}$ as a convolution between the Stokes drift and an inertial oscillation, the Lagrangian transport will contain a train of inertial oscillations for negative $\tilde{x}^*$ of spatial period $\sim 2\pi/r^*$. The amplitude of these oscillations depends strongly on r^*, and to a lesser extent on ν^*.

Table 4.1 shows parameters typical of swell seas and environmental parameters suitable for open-ocean conditions. I have chosen to examine swell with our packet approximation, rather than wind seas, for several reasons. Swell is not as directionally-spread as locally-generated wind seas (Ewans, 2002), allowing weak directional spread to be modelled using a packet aspect ratio $R = \sigma_x/\sigma_y$. An isolated swell sea can also be modelled using a narrow-banded wave spectrum (Toffoli and Bitner-Gregersen, 2017). Additionally, swell has been observed to propagate over extremely long distances without loss of energy or change in its shape (Barber et al., 1948). Finally, I anticipate that since swell is generally not aligned with the local wind, its effects will be most significant when superimposed on the wind-driven Ekman pumping.

From figure 4.2 it is clear that for small r^* and ν^*, the Lagrangian transport is almost identical to the Stokes transport, albeit with a small-amplitude train of weak inertial oscillations (most evident for the (normalised) transverse mass transport $\mathrm{Im}\,(\mathcal{M}^*_{\mathrm{L}})$). The Ekman–Stokes mass transport represents a contribution of approximately 5% to the magnitude of $\mathcal{M}^*_{\mathrm{L}}$ for the chosen value of r^* though in Chapter 3, I found that the Ekman–Stokes flow had an appreciable difference on the Lagrangian displacement. There are two main reasons for this apparent disparity. First, the buoy records used in Chapter 2 have frequencies characteristic of a wind sea, while the swell conditions considered here have lower frequencies and hence a higher group velocity $c_g = g/(2\omega_p)$. Secondly, the direction of the Ekman–Stokes flow tends to spiral with depth (Seshasayanan and Gallet, 2019), such that when it is integrated over depth the resulting Ekman–Stokes mass transport is small. When r^* is larger, as in figure 4.3 the magnitude and inertial behaviour of the

Parameter	Range for swell seas	Chosen value
ω_p [s^{-1}]	$2\pi/25 - 2\pi/10$	$2\pi/15$
A_p [m]	$0.25 - 4$	4
σ_x [m]	$1 \times 10^2 - 5 \times 10^3$	2.5×10^3
σ_y [m]	$1 \times 10^2 - 5 \times 10^4$	7.5×10^3
ν [$m^2 s^{-1}$]	$10^{-6} - 10^{-2}$	10^{-2}
N [s^{-1}]	$0 - 2\pi/900$	$2\pi/2000$
f [s^{-1}]	$0 - 1.45 \times 10^{-4}$	1.45×10^{-4}
δ_S [m]	$12.43 - 77.65$	28
δ_E [m]	$0 - 20.03$	11.75
d [m]	$75 - 1 \times 10^4$	5.25×10^3
α	$10^{-3} - 0.3$	7.1×10^{-2}
ε	$0 - 0.15$	1.1×10^{-2}
R	$0 - 1$	0.33
q^*	$0 - 2.24$	0.67
r^*	$0 - 0.1$	3.1×10^{-2}
ν^*	$0 - 4.2 \times 10^{-3}$	2.7×10^{-3}
D	$0 - 1.6$	0.42

Table 4.1: Range of values for environmental and wave parameters suitable for open-ocean swell (Toffoli and Bitner-Gregersen, 2017; van den Bremer and Taylor, 2015; Haney and Young, 2017). The lower limit of swell frequency, $2\pi/25$ s^{-1}, is taken from Norwegian Sea observations of Gjevik et al. (1988). The third column contains values selected to produce figures throughout §4.4.2, plots of the 2D return flow in §4.4.1 use $N = 2\pi/900$ s^{-1}, $\sigma = 1650$ m, and $\omega_p = 2\pi/10$ s^{-1}. Since $f \to 0$ towards the Equator, the maximum δ_E and D are defined using the value of f at 20° latitude.

Ekman–Stokes mass transport become more significant, and the spatially-periodic imprint of inertial oscillations on the Lagrangian flow becomes more prominent for negative values of $\tilde{x}^*$. Adding the normalised Stokes transport $\mathcal{M}_S^*$ to (4.25), the Lagrangian mass transport far behind the packet has the asymptotic behaviour

$$\lim_{\tilde{x}^* \to -\infty} \mathcal{M}_L^* = \sqrt{\pi}\,(\nu^* - ir^*) \left[e^{-(r^*)^2/4} e^{-ir^*|\tilde{x}^*|} - \frac{1}{2\sqrt{\pi}} \frac{e^{-(\tilde{x}^*)^2}}{|\tilde{x}^*|} \right]. \tag{4.26}$$

In the far field, the mass transport therefore reduces to a pure inertial oscillation, whose direction is set by both ν^* and r^*. Though I include an eddy viscosity ν, this is taken to be a vertical eddy viscosity, which does not cause damping in the horizontal. This is similar to Haney and Young (2017, eq. (5.9)) for the 2D wake far behind the packet. Ahead of the packet ($\tilde{x}^* \to \infty$) the mass transport is zero,

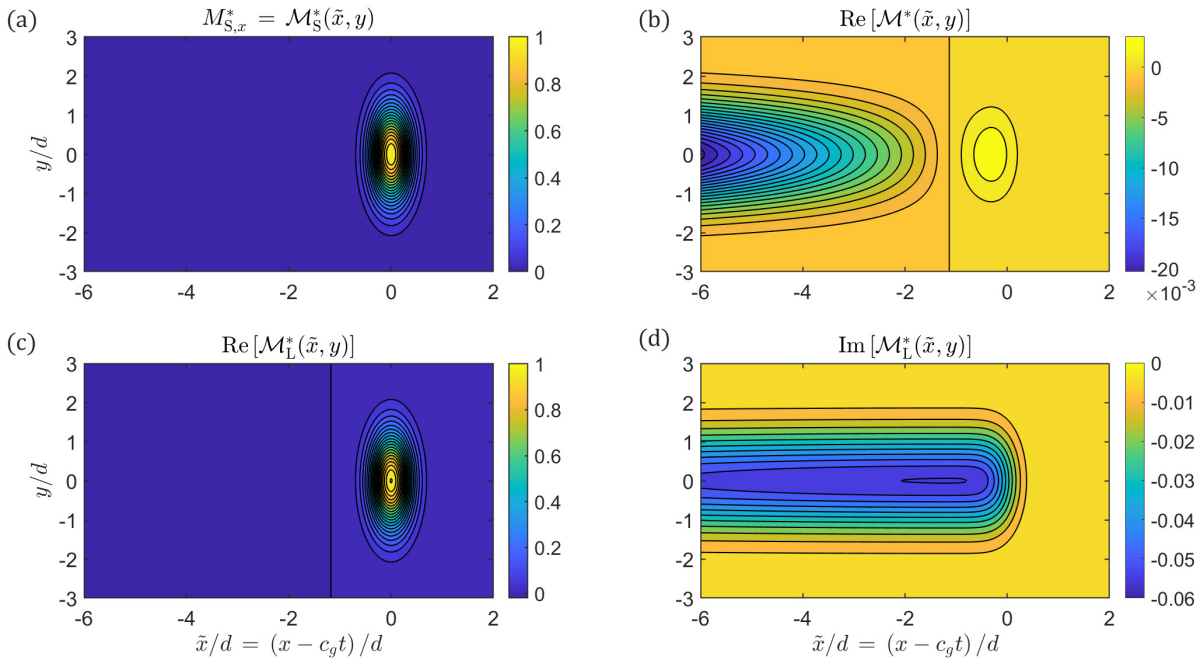

Figure 4.2: Mass transport components for rotational parameter $r^* = 3.1 \times 10^{-2}$ and timescale ratio $\nu^* = 2.7 \times 10^{-3}$, for a Gaussian packet of bandwidth $\varepsilon = 1.1 \times 10^{-2}$ and aspect ratio $R = 1/3$ (cf. third column of table 4.1). Panel (a) gives the (unidirectional) Stokes transport, (c) the real component of the Lagrangian transport, and (b) and (d) the real and imaginary components of the Ekman–Stokes transport, respectively.

as expected. The angle of the Lagrangian mass transport, as $\tilde{x} \to -\infty$, is equal to

$$\theta = \arctan\left(\frac{\mathrm{Im}\,[\mathcal{M}_L]}{\mathrm{Re}\,[\mathcal{M}_L]}\right) = \arctan\left(\frac{1 + \frac{D^2}{2}\tan(r^*|\tilde{x}^*|)}{\frac{D^2}{2} - \cot(r^*|\tilde{x}^*|)}\right), \tag{4.27}$$

where $D^2 = 2\nu^*/r^* = \delta_E^2/\delta_S^2 = 4k_p^2(2\nu/f)$ for a constant eddy viscosity ν. Though (4.26) reduces to a constant-amplitude inertial oscillation in the far-field, in real oceans this oscillation will be slowly dispersed through processes such as damping by horizontal eddy viscosity (which is not modelled here, since ν is a vertical eddy viscosity) or interaction with background ocean circulation (e.g. Kafiabad et al., 2019).

When $r^* = 0$, there is no Coriolis force to balance the shear in the mixed layer, and hence no Coriolis–Stokes forcing. The waves therefore do not experience the large eddy viscosity values within the mixed layer. Taking instead the molecular viscosity of seawater, $\nu \approx 10^{-6}$ m^{2}s^{-1}, can remedy the problem of enhanced boundary-layer streaming near the surface (Huang, 1970; Grue and Kolaas, 2017), which may not be physically realistic in the open ocean. For such a small ν, the

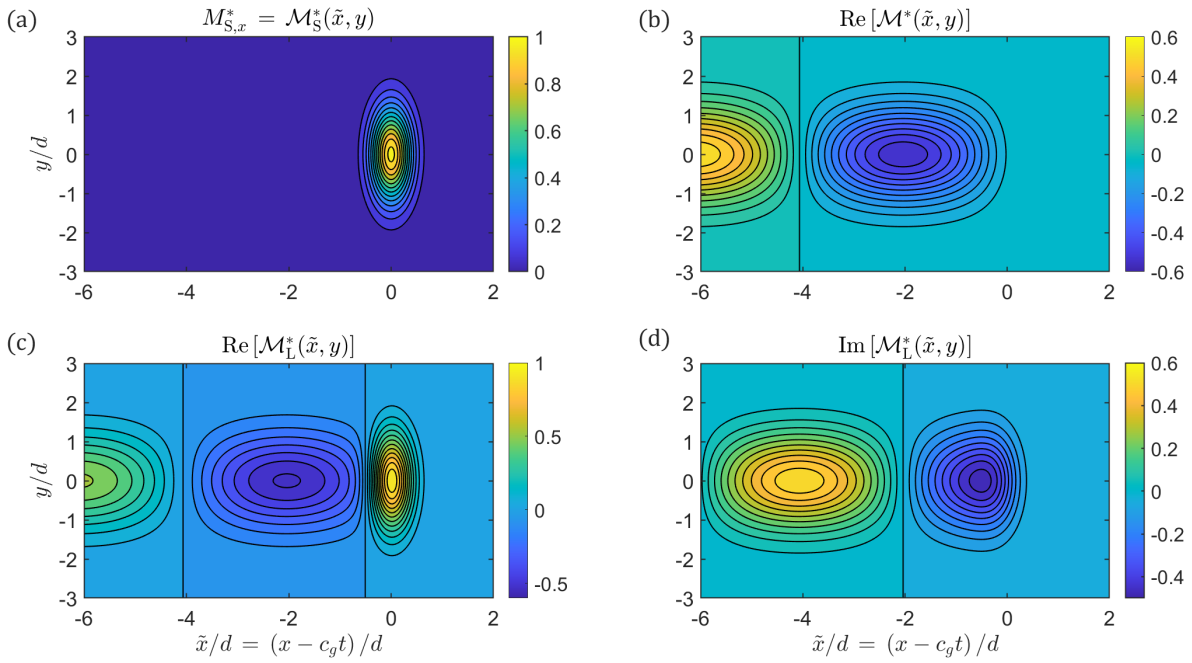

Figure 4.3: Mass transport components for strong rotation $r^* = 3.1 \times 10^{-1}$, so r^* is 10 times larger than in figure 4.2; all other parameters are identical to those in figure 4.2. The Ekman–Stokes transport $\mathcal{M}$ has an appreciable impact on the Lagrangian mass transport $\mathcal{M}_\mathrm{L}$ due to large-amplitude inertial motion behind the packet.

Ekman–Stokes transport becomes negligible and the boundary condition on the outer flow reads $W|_{Z\to 0^-} = \boldsymbol{\nabla}_\mathrm{H} \cdot \mathbf{M}_\mathrm{S}$.

I neglect nontraditional effects of the Coriolis force in the outer layer, while noting that these may be important in certain special cases. For example, the traditional Coriolis parameter becomes small near the Equator, while the nontraditional component becomes larger. For this reason, I restrict my calculations to lie outside an Equatorial band spanning the latitude range $20°\mathrm{S} - 20°\mathrm{N}$. I also ignore the variation of f with the meridional coordinate y, i.e. I do not consider β-plane effects. These assumptions should be valid for the small (w.r.t. the Rossby deformation radius c_g/f) spatial extents considered, and below the critical latitudes at which inertia-gravity waves are reflected; Gerkema and Shrira (2005) note that the nontraditional Coriolis component allows sub-inertial waves to propagate beyond these latitudes.

Under the traditional approximation in which the horizontal Coriolis component is neglected, the propagation direction can be arbitrarily aligned with the x-axis

and the packet frame defined as $\tilde{x} = x - c_g t$. To enforce causality, it is assumed that the packet has been slowly growing from $t = -\infty$ at a rate $c_g\eta$ which is later taken to zero through positive values. It follows that time derivatives may be exchanged for (causal) spatial ones, $\partial_t = -c_g\left(\partial_{\tilde{x}} - \eta\right)$, and the vertical velocity satisfies the inertia-gravity wave problem

$$\left[\partial^2_{\tilde{x},\eta}\left(\partial^2_{\tilde{x}} + \partial^2_y + \partial^2_Z\right) + q^2\left(\partial^2_{\tilde{x}} + \partial^2_y\right) + r^2\partial^2_Z\right]W = 0, \quad W|_{Z\to 0^-} = \boldsymbol{\nabla}_{\mathrm{H}}\cdot\mathbf{M}_{\mathrm{L}}, \quad W|_{Z=-d} = 0 \tag{4.28a,b,c}$$

where $c_g\partial_{\tilde{x},\eta} = -c_g\left(\partial_{\tilde{x}} - \eta\right)$ and $q = N/c_g$ and $r = f/c_g$ are the (dimensional) stratification and Coriolis wavenumbers, respectively. By transforming to Fourier space $(\tilde{x}, y) \to (k, l)$, the Fourier-space solution to the boundary-value problem (4.28) is

$$\hat{W} = i\boldsymbol{k}\cdot\widehat{\mathbf{M}}_{\mathrm{L}}\frac{\sinh\left(m\left(Z+d\right)\right)}{\sinh\left(md\right)}, \quad \text{where} \quad m = \sqrt{k^2+l^2}\sqrt{\frac{k_\eta^2 - q^2}{k_\eta^2 - r^2}}, \tag{4.29}$$

where $\boldsymbol{k} = (k, l)$ and $k_\eta = k + i\eta$. To close the problem for the outer flow, I find from (4.21) (with $\tilde{f} = 0$) that the horizontal velocity components are linked to W by the Fourier space expressions

$$\begin{pmatrix}\widehat{U}\\ \widehat{V}\end{pmatrix} = -\hat{\boldsymbol{k}}\cdot\widehat{\mathbf{M}}_{\mathrm{L}}\left[\begin{pmatrix}\hat{k}\\ \hat{l}\end{pmatrix} - \frac{ir}{k_\eta}\begin{pmatrix}-\hat{l}\\ \hat{k}\end{pmatrix}\right]\frac{m\cosh\left(m\left(Z+d\right)\right)}{\sinh\left(md\right)}, \tag{4.30}$$

where $\hat{\boldsymbol{k}} = (k, l)/\sqrt{k^2+l^2}$. In the absence of rotation ($r = 0$) m in (4.29) reduces to the depth structure given by equation (2.39) in Chapter 2, and the return flow is as described therein and in Haney and Young (2017). If N and f are both set equal to 0, the unstratified potential flow results for which $\boldsymbol{U}_{\mathrm{H}} = \boldsymbol{\nabla}_{\mathrm{H}}\phi_2$ are recovered, and (4.21) reduces to $\partial_t\boldsymbol{\nabla}_{\mathrm{H}}$ of the Laplace equation.

The velocity in real (x, y)-space is found from (4.30) by taking the inverse Fourier transform. As the causal growth rate $c_g\eta \to 0^+$, the solution is concentrated about 'singular curves' in (k, l)-space, which are given by the zeros of the function

$$\gamma_n(k,l) = k - \sqrt{\frac{q^2\left(k^2+l^2\right) + r^2m_n^2}{k^2+l^2+m_n^2}}, \tag{4.31}$$

where $m_n = n\pi/d$. By rearranging $\gamma_n(k, l) = 0$, it can be seen that the resonant curves correspond to a resonant matching condition between the x-phase speed

of an emitted inertia-gravity wave with mode number n and the group velocity associated with the surface wavepacket,

$$c_g^2 = \frac{1}{k^2}\left(\frac{N^2\left(k^2+l^2\right)+f^2m_n^2}{k^2+l^2+m_n^2}\right) = \frac{\omega_{\mathrm{IG},n}^2}{k^2}, \tag{4.32}$$

where $\omega_{\mathrm{IG},n}$ is the angular frequency of the nth inertia-gravity wave mode. For very long inertia-gravity waves in 2D, $k^2 \ll m_n^2$ and

$$c_g^2 \approx f^2/k^2 + N^2/m_n^2. \tag{4.33}$$

Haney and Young (2017) found that there was a minimum value of stratification frequency N required for radiation of internal waves by a 2D packet ($N = \pi c_g/d$, from the long-wave limit $k \to 0$ of (4.33) with $f = 0$). Rotation acts to reduce the minimum stratification frequency N required for the presence of a wake in 2D. Nonetheless, the change in radiation condition due to f is likely to be small, except perhaps for very long packets.

The wake angle is found by matching the component of surface wave group velocity to the inertia-gravity wave phase velocity perpendicular to the crest of the inertia-gravity wave. Following the argument of Haney and Young (2017),

$$\sin\theta_n = \frac{1}{\sqrt{k^2+l^2+m_n^2}}\sqrt{q^2+r^2\frac{m_n^2}{k^2+l^2}}. \tag{4.34}$$

Assuming that the second term under the large square root is much smaller than the first term, the leading-order wake angle correction due to f may be obtained,

$$\sin\theta_n = \frac{q}{\sqrt{k^2+l^2+m_n^2}}\left(1+\frac{r^2}{2q^2}\frac{m_n^2}{k^2+l^2}\right) = \frac{N}{c_g\sqrt{k^2+l^2+m_n^2}}\left(1+\frac{f^2}{2N^2}\frac{m_n^2}{k^2+l^2}\right). \tag{4.35}$$

In Haney and Young (2017), the authors obtained the maximum wake angle by maximising over wavenumbers, which amounted to setting $k = l = 0$. The inclusion of f makes this impossible, since it acts as a singular perturbation: there are in fact no stationary points of (4.34) for $f \neq 0$. Since the Coriolis correction in (4.35) is positive, f acts to slightly increase the wake angle for each mode. For $f = 0$, the wake angle decreases with an increase in the mode number n, however this is not the case when $f \neq 0$, and (4.35) implies that inertia-gravity waves with a higher mode number may be more influenced by Coriolis effects.

4.4.1 2D return flow

I first examine the 2D case, in which the velocity field is independent of the transverse y-coordinate and may be described in terms of a streamfunction, $\boldsymbol{U} = (-\partial_Z\psi, V, \partial_{\tilde{x}}\psi)$,

$$\psi = \frac{1}{2\pi}\int_{-\infty}^{\infty} \widehat{M_{\mathrm{L},x}}\frac{m\cosh\left(m\left(Z+d\right)\right)}{\sinh\left(md\right)}e^{ik\tilde{x}}dk, \quad \text{with} \quad m = k\sqrt{\frac{k_\eta^2 - q^2}{k_\eta^2 - r^2}}. \tag{4.36}$$

In figure 4.4, the (normalised) streamfunctions $\psi^* = 2\psi/\left(\omega_p|A_p|^2\sqrt{\pi}\right)$ are plotted for various values of the (dimensionless) stratification wavenumber $q^* = q\sigma_x$ and Coriolis wavenumber $r^* = r\sigma_x$. The chosen wave parameters (amplitude $A_p = 4m$, frequency $\omega_p = 2\pi/10\ \mathrm{s}^{-1}$ and packet length $\sigma_x = 1650$ m) are characteristic of storm-generated, large-amplitude, high-frequency swell. The ocean is of depth $d = 3.2\sigma_x$.

Setting $r = 0$ in (4.36) recovers the form of equation (2.37b) in Chapter 2 for a stratified return flow. As noted earlier, the nonrotating limit implies that the Ekman–Stokes transport is negligible, and the forcing on the return flow reverts to $W|_{Z\to 0^-} = \boldsymbol{\nabla}_{\mathrm{H}}\cdot\mathbf{M}_{\mathrm{S}}$. In the nonrotating case, the y-independent V component of the velocity is zero. As established in Haney and Young (2017), internal wave radiation in 2D requires $qd > \pi$, where d is the ocean depth. I choose a value of $N = 2\pi/900\ \mathrm{s}^{-1}$ which satisfies this condition ($qd/\pi = 1.19$).

The two bottom panels in 4.4 correspond to the unstratified and stratified streamlines, respectively, in the presence of realistic rotation $f = 1.4\times10^{-4}\ \mathrm{s}^{-1}$, with the Ekman–Stokes boundary condition given by $\psi|_{Z\to 0^-} = M_{\mathrm{L},x}$. As can be seen from panel (c), realistic rotation has an almost negligible influence on the unstratified return flow. By contrast, panel (d) shows that the stratified return flow ($N = 7\times10^{-3}\ s^{-1}$) is significantly impacted by Coriolis effects. Rotation induces a transverse velocity component, which are plotted in figure 4.5. The rescaled transverse velocity, $V^* = 2\sigma_x V/\left(\omega_p|A_p|^2\sqrt{\pi}\right)$, is practically negligible in unstratified flow (top panel, corresponding to 4.4(c)), but may be of considerable magnitude for a rotating, stratified 2D return flow (bottom panel, corresponding to 4.4(d)). Clearly, rotation has the greatest impact on the outer return flow when density stratification is also present. This is the result of two separate but related

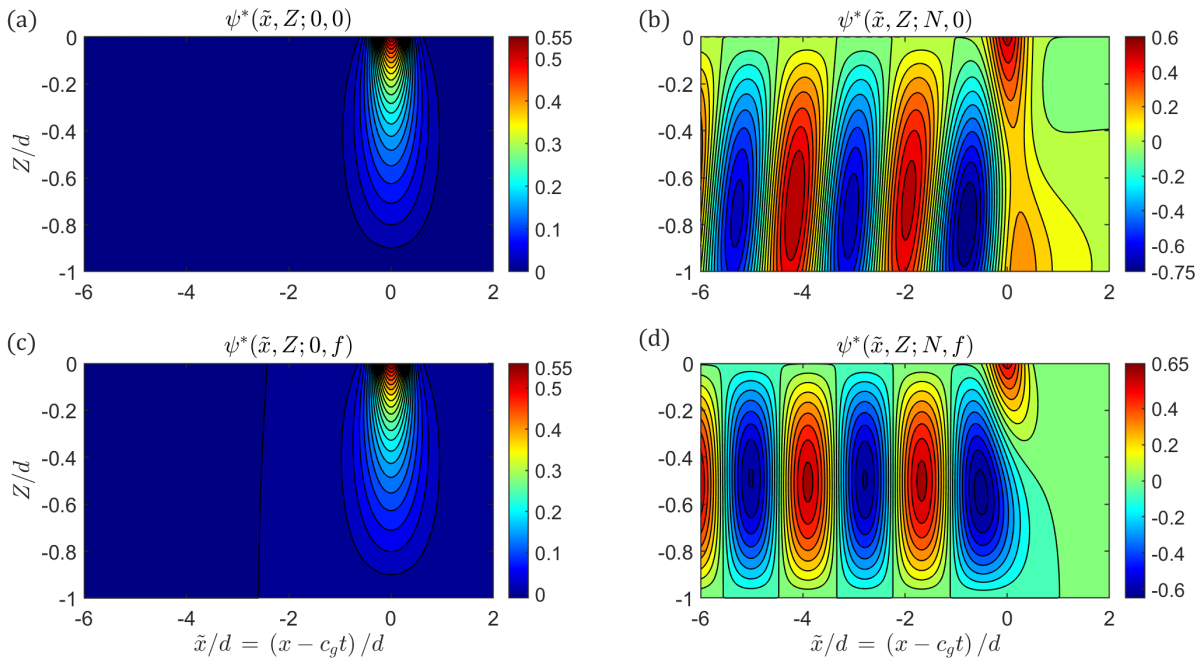

Figure 4.4: Return flow streamfunctions in the presence of different effects. **Top:** Streamfunctions without rotational effects ($r^* = 0$), and neglecting the Ekman–Stokes flow in the upper layer ($M_{\mathrm{L},,x} = M_{\mathrm{S},x}$). Panel (a) is unstratified and nonrotating, panel (b) is stratified with $q^* = 1.49$. **Bottom:** Streamfunctions with rotational effects ($r^* = 3.1 \times 10^{-2}$), for unstratified flow (panel (c)) and stratified flow (panel (d), $q^* = 1.49$). In panels (a) and (c), contours are spaced at intervals of 0.025. In (b) and (d), contours are spaced at intervals of 0.075.

effects. First, stratification distorts the return flow by squashing it vertically and elongating its scale in the $\tilde{x}$-direction. When stratification is large enough, a 2D packet also drags along a train of internal waves behind it. As the spatial extent of the return flow is increased by N, the return flow becomes more susceptible to the effects of the Coriolis force. Second, the presence of rotation changes the resonance condition between the surface wave speed and the wake of waves behind the surface wave packet. Instead of internal waves, the surface wavepacket generates inertia-gravity waves in the packet's wake (c.f. (4.32)). Coriolis effects allow inertia-gravity wave radiation in 2D for lower values of stratification frequency N than in the stratified but nonrotating case. The rotational change to the resonance condition may be seen by comparing figure 4.4(b) with 4.4(d): the train of waves behind the packet switches from internal-wave modes to inertia-gravity modes, with impact on the oscillatory form of the wake.

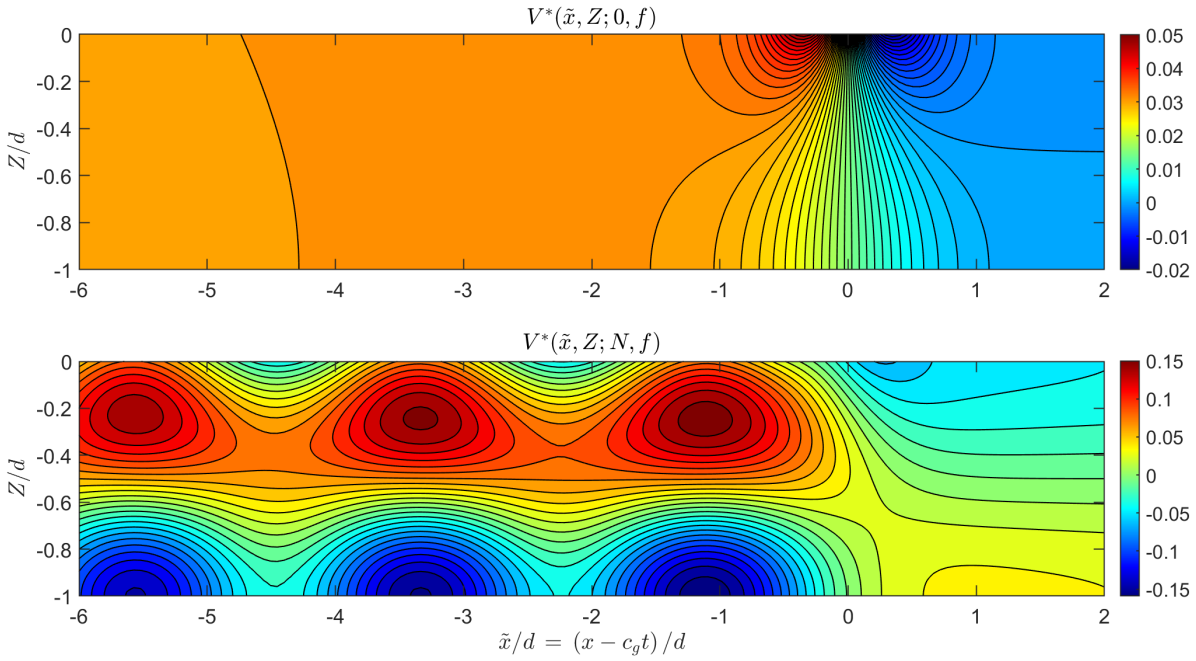

Figure 4.5: Rescaled transverse velocity components in rotating flow ($r^* = 3.1 \times 10^{-2}$). **Top:** Unstratified return flow, (contour interval 1.25×10^{-3}). **Bottom:** Stratified return flow ($q^* = 1.49$) (contour interval 1.25×10^{-2}).

For larger values of f, even the unstratified return flow is visibly distorted by rotation. The primary reason for this is the intensification of inertial motion within the surface forcing (cf. figure 4.3). In the strong-rotation limit (alternatively, the large r^* limit), the return flow becomes 'delocalised' from the packet, in the sense that strong velocities are found far from the packet. In a stratified outer layer for strong f, the train of strong inertial oscillations in the mass transport $\mathbf{M}_{\mathrm{L}}$ for negative $\tilde{x}$ also force the layer below, acting as if they were packets (for example, 4.6(c) and 4.6(d)). This forcing at regular spacing $O(2\pi c_g/f)$ can lead to a superposition of inertia-gravity wave modes in a deep ocean, resulting in complex interference patterns within the inertia-gravity wave wake, for instance in 4.6(d). In fact, the strongest velocities are found far behind the packet.

4.4.2 3D return flow

Due to directional spread of the wave components about the mean propagation direction, surface gravity wavepackets are also weakly localised perpendicular to

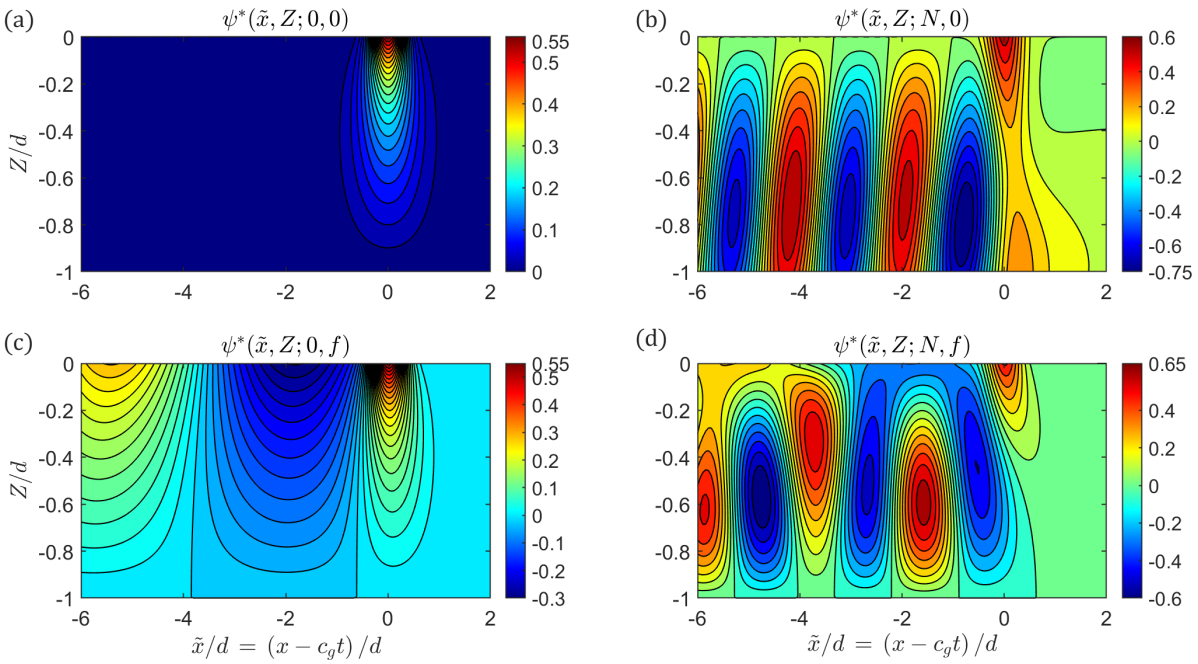

Figure 4.6: Same as figure 4.4, but with a value of r^* which is 10 times larger than in figure 4.4. Contour intervals are the same as in 4.4

the propagation direction (e.g. van den Bremer and Taylor, 2015). Haney and Young (2017) showed in a nonrotating ocean that, when the packet is 3D (i.e. it is also localised in y due to nonzero directional spread), a wake of internal waves is always present. This is because radiated inertia-gravity waves can satisfy the required resonance (4.32) between their x-phase speed and the surface wave group velocity by propagating obliquely to the packet's propagation direction. In Haney and Young (2017), the wake angle is set by the relative magnitudes of $q^* = N\sigma_x/c_g$ and $m_n^* = n\pi\sigma_x/d$. Though the influence of realistic rotation on the forcing at the base of the Ekman–Stokes layer is rather weak, its impact on the outer-layer return flow can be significant when combined with density stratification, as seen in §4.4.1. In figure 4.7, the return flow towards the base of the upper layer ($Z = -d/10$) is plotted for the choice of dimensionless parameters given in the third column of Table 4.1, and figure 4.8 shows the flow at greater depth ($Z = -3d/4$). The inertia-gravity wave wake is clearly visible at both depths, particularly for the V and W velocity components. Though the rescaled $\tilde{x}$-component of velocity U^* (panel (a) in both figures) is almost symmetric about the $\tilde{x}$-axis, the transverse component

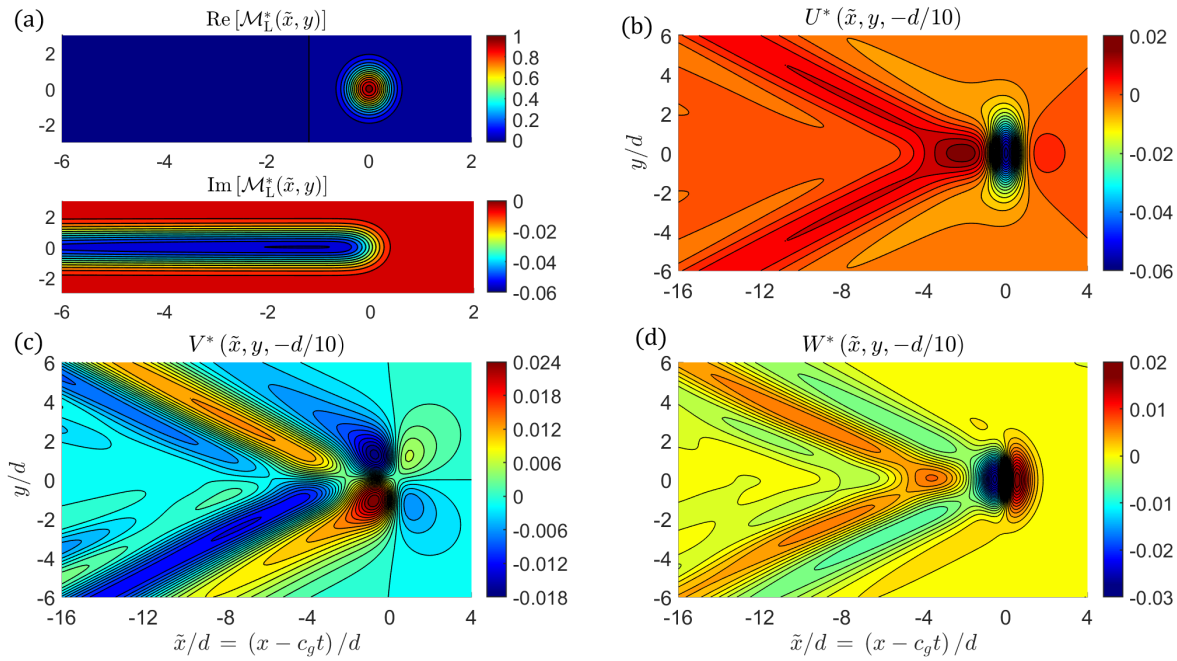

Figure 4.7: Plan view of the nondimensional forcing at $Z = 0$ (two subpanels in panel (a)) and the velocity components at a level $Z/d = -0.1$ (b,c,d). Dimensionless parameters are $q^* = 0.67$, $r^* = 3.1 \times 10^{-2}$ and $\nu^* = 2.7 \times 10^{-3}$, with the packet bandwidth $\varepsilon = 1.1 \times 10^{-2}$. The ocean depth scale $d^* = d/\sigma_x = 2.5$.

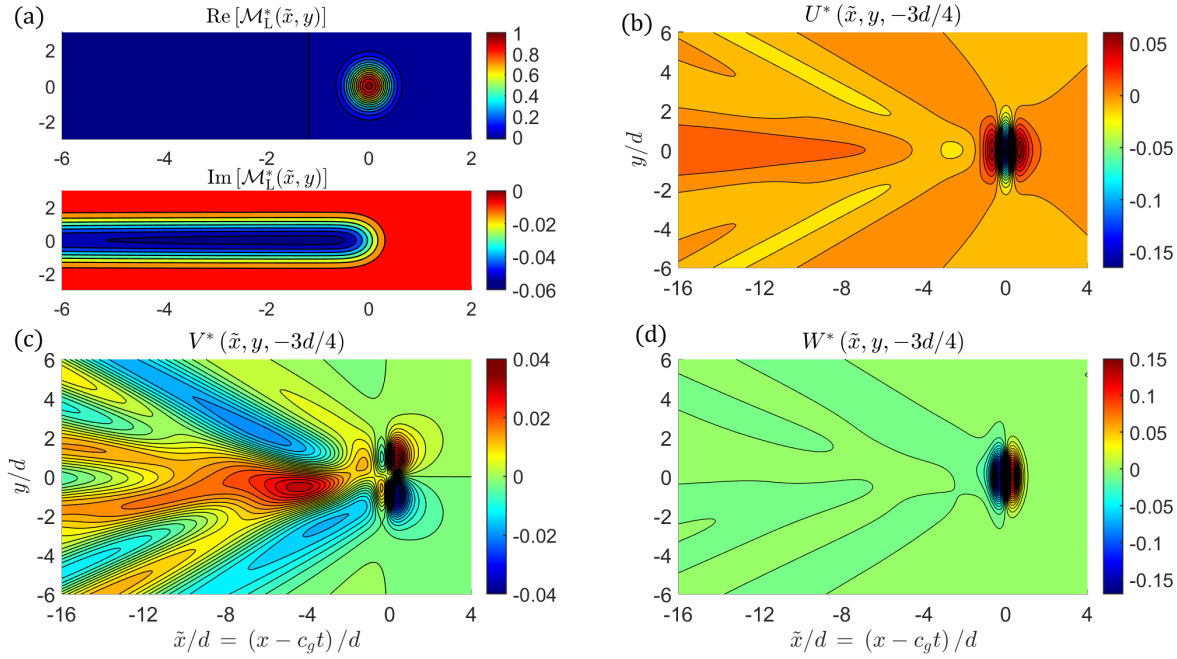

Figure 4.8: Plan view of the nondimensional forcing at $Z = 0$ (two subpanels in panel (a)) and the velocity components at a level $Z = -3d/4$ (b,c,d). Dimensionless parameters are the same as in 4.7.

V^* and vertical component W^* are noticeably affected by Earth's rotation. Though V^* is quite small at $Z = -d/10$, the Coriolis effect breaks the anti-symmetry of the inertia-gravity wake about $y = 0$.

The horizontal velocity components are stronger in figure 4.8, at depth, than they are at $Z = -d/10$, while the vertical velocity is weaker. Comparing panel (c) in figures 4.8 and 4.7 reveals a striking difference in the behaviour of the transverse velocity V^*: though the wake angle remains the same in both, the inertia-gravity wave crests are deflected to the right of the packet propagation. Hasselmann (1970) noted in his study of inertial wave generation by surface waves that the amplitudes of induced inertial oscillations are generally larger near the ocean floor. This is because, once the barotropic mode is subtracted, the oscillations (negatively) increase in amplitude with increasing depth. This may partially explain the larger magnitudes of U^* and V^* at greater depth. The different modes seem to also be affected differently by f and depth: the higher modes ($m_n = n\pi/d$ with $n = 3, 4, 5$) are stronger at $Z = -3d/4$ than at $Z = -d/10$, and appear to be more significantly distorted by rotation (cf. (4.35)).

When the ocean is very weakly stratified, it may sometimes happen that $N \approx f$ (for example, in some polar regions). The near-equality of N and f in such special cases has a profound impact on the return flow. Examining the depth structure m in (4.30), a peculiar cancellation occurs between the effects of f and N when $N \approx f$; m reduces approximately to $\sqrt{k^2 + l^2}$, which is the depth structure of an unstratified return flow. Recalling the dispersion relation for inertia-gravity waves,

$$\omega_{\mathrm{IG},n}^2 = N^2 \frac{k^2 + l^2}{k^2 + l^2 + m_n^2} + f^2 \frac{m_n^2}{k^2 + l^2 + m_n^2}. \tag{4.37}$$

Therefore, in the weak-N limit all radiated inertia-gravity modes approach a single frequency $\omega_{\mathrm{IG}} = N = f$. When $N \to f$, the effects of rotation and stratification on the return flow cancel out: that is, the return flow becomes identical to one in which f and N are neglected in the outer layer, but the updated forcing condition (4.13) with $f \neq 0$ is used. Figure 4.9 compares the potential flow velocities to those of a flow with $q^* = r^*$. By taking the gradient of $\omega_{\mathrm{IG},n}$ with respect to $\boldsymbol{k}$, it can be verified that the group velocity of the inertia-gravity waves vanishes when $N = f$.

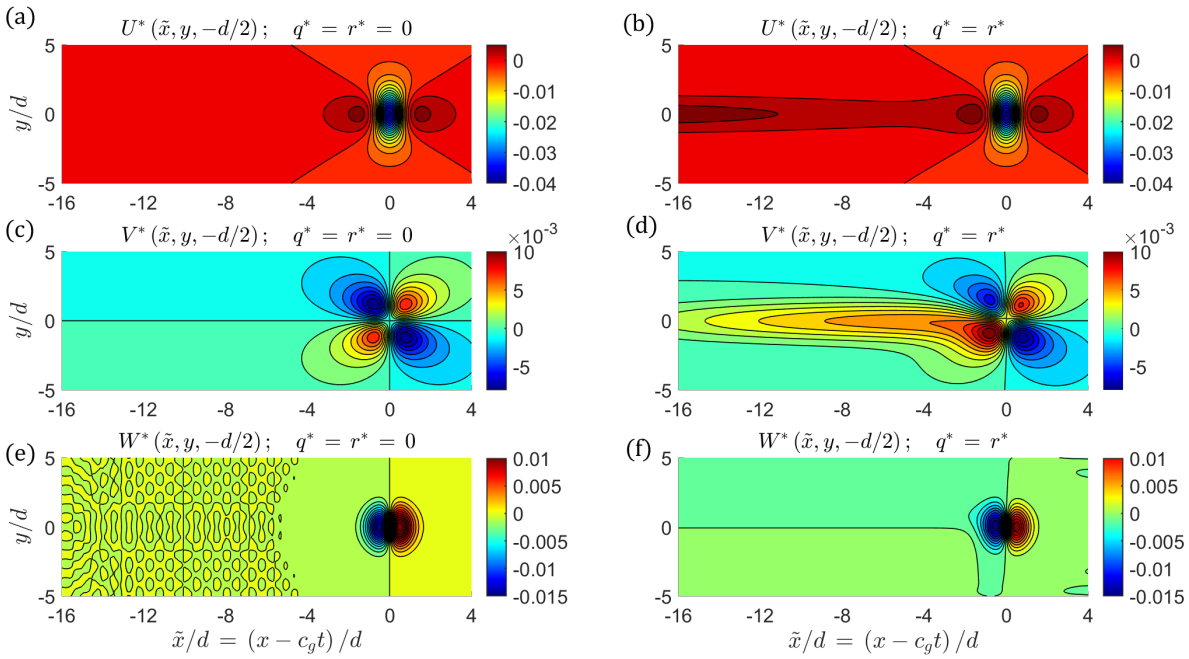

Figure 4.9: Comparison between velocity components of potential flow (left column) and rotating, stratified flow with $q^* = r^* = 3.1 \times 10^{-2}$ (right column) at a depth $Z = -d/2$. The first row is the $\tilde{x}$-component, the second row is the y-component, and the bottom row is the vertical component.

4.4.3 Synoptic-scale variation

In this chapter I have limited my analysis to packets of narrow-banded swell with lengths of a few kilometres. Over these scales the Ekman–Stokes contribution to the Lagrangian mass transport is small compared with the Stokes transport $\mathbf{M}_\mathrm{S}$ and the main impact of f is on the return flow in the outer layer. The wave field in the open ocean is also observed to vary over larger scales $\gtrsim 10$ km (Gemmrich et al., 2016) on the synoptic scale of passing storms. While a packet approximation is oversimplified, I will model a large, slowly-varying storm-generated wave field as a packet with length $\sigma_x = 10$ km, peak frequency $\omega_p = 2\pi/20$ s^{-1} and peak wave height $A_p = 16$ m. For such a long 'packet', $d/\sigma_x \ll 1$ and the return flow in the outer layer is shallow. For simplicity, I neglect density stratification in this limit rather than adopting e.g. the model of a two-layer stratified fluid. The hyperbolic functions describing the depth-dependence of the velocity components can be replaced by the leading term in their Taylor expansions and therefore U^* and V^* are independent

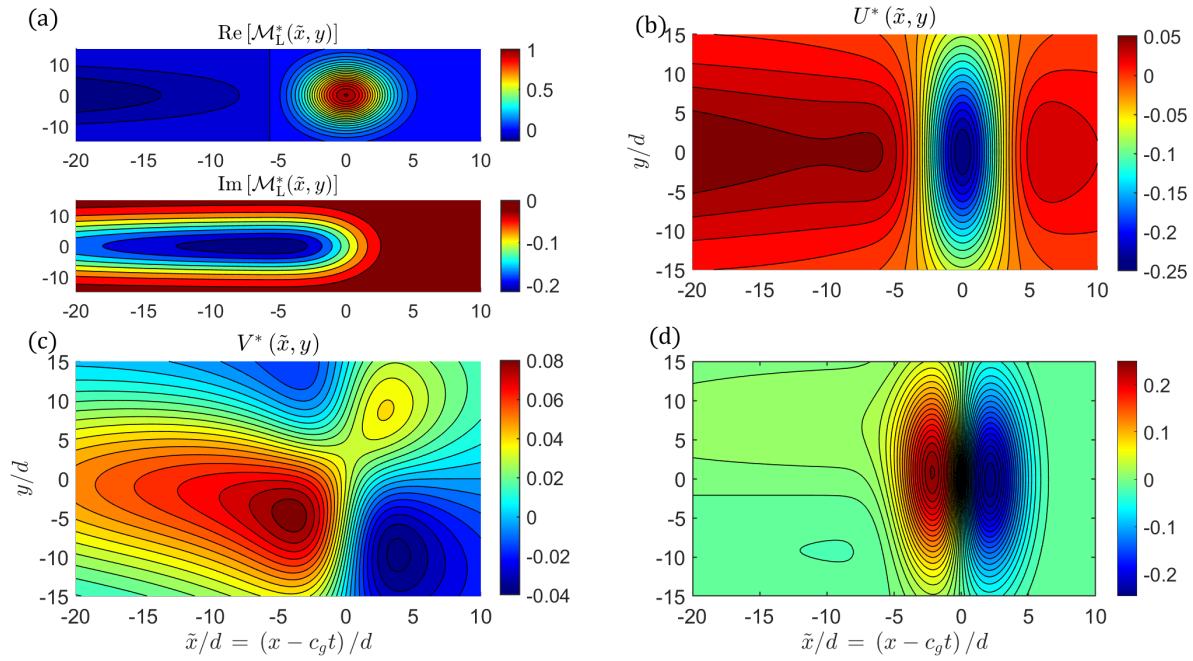

Figure 4.10: Lagrangian mass transport components (panel (a)) and velocity components (b,c,d) for a synoptic-scale 'packet' with $\sigma_x = 10$ km. Stratification is neglected since $d/\sigma_x \ll 1$, and $r^* = 0.14$. W^* is plotted at $Z = -d/10$.

of depth (while $W^* \propto (Z + d)/d$). The mass transport and velocity components are plotted in figure 4.10. Though the $\tilde{x}$-component of $\mathbf{M}_{\mathrm{L}}$ maintains the Gaussian shape of $\mathbf{M}_{\mathrm{S}}$, there is now a very long, weaker inertial oscillation for negative $\tilde{x}$. The normalised y-component is also large in magnitude, suggesting that the sea state is generating inertial oscillations as it propagates.

The velocity component W^* is largely similar to the vertical velocity of an unstratified shallow return flow. The inertial oscillation in the boundary-layer forcing does however distort the U^* velocity by strengthening its magnitude directly behind the packet. Again, the most significant differences due to rotation are seen in the transverse velocity component V^*. The lobe of positive (Northwards) velocity is shifted upward and stretched towards negative $\tilde{x}$ by rotation. As the outer flow is shallow and significantly affected by rotation, the horizontal components are more coherent and the return flow behaves increasingly like an inertial oscillation as r^* is increased. This is consistent with Hasselmann (1970), who found that a spatially-varying surface wave field induced inertial oscillations, modulated in

both amplitude and phase.

4.5 Discussion and conclusions

While the wave-induced Ekman–Stokes flow is driven by the Coriolis force and turbulent viscosity in the upper ocean boundary layer, Eulerian-mean flows may also be driven through slow-scale spatial variation in the amplitude of the surface wave field. The characteristic scale of horizontal variation of the wave amplitude, σ_x, is generally much larger than both the Stokes depth $\delta_{\mathrm{S}} = (2k_p)^{-1}$ and the Ekman depth $\delta_{\mathrm{E}} \sim \sqrt{\nu/f}$. I have taken advantage of this separation in scales, and the depth-localisation of the Coriolis–Stokes forcing and the turbulent eddy viscosity to the Ekman–Stokes layer, to pursue a boundary-layer approach to the problem. Within the Ekman–Stokes (upper) layer of depth δ_{E}, the sum of the Stokes drift and the horizontal wave-induced Ekman–Stokes velocity constitute the leading-order Lagrangian-mean flow at second order in wave steepness, $O(\alpha^2)$. A small 'Ekman–Stokes pumping' (vertical) velocity w_2 results from the spatial variation of the Ekman–Stokes flow, which is inherited parametrically through convolution with the Stokes drift (cf. Higgins, Vanneste, et al. (2020)). Regions of positive vertical velocity lead to upwelling of mass, while downwelling of mass occurs in regions of negative w_2. This 'Ekman–Stokes pumping' is given by the horizontal divergence of the Lagrangian mass transport $\mathbf{M}_{\mathrm{L}} = \mathbf{M} + \mathbf{M}_{\mathrm{S}}$, and is weaker than the Lagrangian-mean velocity in the upper layer by a small bandwidth parameter $\varepsilon = (2k_p\sigma_x)^{-1}$. An analogy with the more familiar wind-driven Ekman pumping can be drawn in the steady case, since the Ekman–Stokes pumping velocity equals the curl of the wave stress divided by f while the wind-driven Ekman pumping velocity equals the curl of the wind stress over f (McWilliams and Restrepo, 1999).

Where winds converge/diverge, the associated local wind sea represents an additional Eulerian-mean contribution to the downwelling/upwelling that is induced. Long groups of large-amplitude swell may also play a role in upper-ocean mixing over scales of a few kilometres, and their associated Ekman–Stokes pumping may influence the zones of (predominantly wind-driven) convergence and divergence

observed in marine litter studies (van Sebille, Aliani, et al., 2020). In particular, wave-induced pumping may partly account for the observed time-variability of these convergence zones and contribute to the leakage of plastic particles into/out of the so-called 'garbage patches' (Lebreton, Greer, et al., 2012; Fraser et al., 2018). For most realistic values of packet length and frequency for a swell sea, the Ekman–Stokes pumping velocity at the base of the mixed layer is almost unaffected by rotation. The contribution to $\mathbf{M}_{\mathrm{L}}$ due to $\mathbf{M}$ is about 5% of the magnitude of $\mathbf{M}_{\mathrm{S}}$ for typical swell seas. However, by crudely modelling a wave field with synoptic-scale variation $\sim O(10^5)$ m as a wavepacket, I speculate that the Ekman–Stokes transport may have a significant impact on the Lagrangian transport $\mathbf{M}_{\mathrm{L}}$ over such scales.

By using boundary-layer methods to match the inner and outer components of vertical velocity at the base of the Ekman–Stokes layer, I have shown that the divergence of the Lagrangian mass transport $\mathbf{M}_{\mathrm{L}}$ (the sum of the Stokes transport $\mathbf{M}_{\mathrm{S}}$ and Ekman–Stokes transport $\mathbf{M}$) drives an additional Eulerian return flow in the outer layer (van den Bremer and Breivik, 2017; Higgins, van den Bremer, et al., 2020). Eddy viscosity beneath the Ekman–Stokes layer is assumed to be negligible. Since the dynamics in this outer region are driven by pressure gradients, the Coriolis force, and density stratification, the equation of motion for the vertical velocity takes the form of an inertia-gravity wave equation. I solve this by taking a Fourier transform in the horizontal variables and solving the Fourier-space ordinary differential equation in the vertical coordinate Z, as in Higgins, van den Bremer, et al. (2020), though the solution may also be expressed in terms of a set of vertical modes (e.g. Haney and Young (2017)). The solution is concentrated about singular curves in Fourier space, corresponding to a resonance between the surface wave group velocity and the x-phase velocity of an inertia-gravity mode.

When stratification is ignored ($N = 0$), the effect of f on the return flow is practically negligible for all but very strong rotation rates or very long packets. The weak effect of realistic rotation on the unstratified return flow is most noticeable in 2D, where rotation induces a small transverse velocity component whose amplitude scales as $r^* = f\sigma_x/c_g$, where f is the Coriolis frequency, σ_x the group length and

c_g the group velocity of the waves (also, the translation speed of the packet). In the rapidly-rotating limit, a train of inertial oscillations may appear in the packet's wake due to resonance between the surface wave group velocity and the phase velocity of a spatially-varying inertial mode. The forcing on the return flow also contains a strong inertial signature in this limit, leading to periodic forcing of the return flow at regular intervals of approximate length $2\pi c_g/f$.

Though the influence of the Coriolis force on the unstratified return flow is practically negligible for weak rotation, it has an appreciable effect upon the stratified return flow induced by a long wavepacket ($\sigma_x \gtrsim 10^3$ m). Haney and Young (2017) found that in 2D, a wake of internal waves is generated due to a resonance between the surface wave group velocity and the x-phase speed of an internal wave mode, but only when the stratification exceeds a minimum value. Due to the influence of f in the presence of stratification, the minimum bound on N required for radiation of an inertia-gravity mode is reduced. Additionally, a 2D return flow will be accompanied by a y-independent transverse component V which has a comparable magnitude to the x-velocity, rather than scaling like $r^* = f\sigma_x/c_g$ as in the unstratified case.

Due to the extra degree of freedom, an inertia-gravity wake is always present in 3D, though when $N = 0$ but $f \neq 0$, this is of such small amplitude and long spatial period that it is negligible for realistic values of the Coriolis frequency. Realistic rotation breaks the (anti-)symmetry of the transverse and vertical velocity components V and W about the centreline of the packet. This is most noticeable in the inertia-gravity wake and particularly at depth, where the horizontal velocity components are stronger. In addition to increasing slightly the wake angle of the radiated inertia-gravity waves, the Coriolis force deflects the wave crests in the wake to the right of the packet in the Northern Hemisphere and to the left in the Southern Hemisphere.

However, if the stratification and Coriolis frequencies happen to be almost equal ($N \approx f$), a peculiar cancellation occurs in 2D and in 3D between the effects they induce. The return flow becomes almost identical in form to the return flow in an unstratified, non-rotating ocean, and no inertia-gravity waves appear in the packet's

wake. The return flow still differs from the potential flow case, as it possesses a small transverse component due to a nonzero Coriolis frequency.

4.6 Neglected effects and possible extensions

Haney and Young (2017) examined the energy transfer from the surface gravity wavepacket to the internal-wave wake. Though they find that the energy flux has a minuscule impact on the packet, they note that the forcing from extreme large-amplitude, long-period swell ($A_p = 4$ m and $\omega_p = 2\pi/20$ s^{-1}) is a significant source of energy for near-N internal waves. Though typical values of $r^* = f\sigma_x/c_g$ are small, rotation can dramatically change the behaviour of the wake. Haney and Young's calculation of the radiation integral should therefore be extended to include Coriolis effects. To make the computations as amenable as possible, it will probably be necessary to pursue a solution in modes from the outset.

The quasi-monochromatic assumption is likely to become an over-simplification for most realistic sea states. A broad-banded spectrum, or perhaps a bimodal random sea with a swell peak and a wind sea peak, would provide a more realistic representation of synoptic-scale variations in realistic sea states (Ewans et al., 2006). Even for measured narrow-banded swell spectra, Lucas and Guedes Soares (2015) found that a JONSWAP model was a better fit than a Gaussian spectrum. This is primarily because the JONSWAP spectrum provides a better fit in the high-frequency range of swell. Since the effects of f are most significant for long and slow-moving packets, relaxing the quasi-monochromatic assumption represents an important next step towards accounting for the influence of the Coriolis force on surface gravity waves.

The calculation I have presented could, in theory, be performed without making such a packet assumption. This would be equivalent to examining the flow induced by, for example, a passing weather system which creates synoptic-scale spatial variation in the wave field. An advantage of such a calculation would be that it permits both non-propagating and co-moving flows, and could be viewed as an extension to the phase-mixing analysis of Hasselmann (1970), who examined the

generation of slowly-varying inertial oscillations by surface waves. In the presence of stratification, these motions may form part of the important near-inertial peak of the oceanic inertia-gravity wave spectrum.

In this chapter, the assumption of a small background Rossby number has simplified some of the analysis but precluded investigation of possible interactions between the return flow and motions not induced by surface waves, such as geostrophic currents and submesoscale eddies. These features are of great importance in general ocean circulation models, and future work should examine how they interact with the return flow, in particular the 3D wake of inertia-gravity waves.

Chapter 5
Conclusions

In this thesis I have examined two main mechanisms through which deep-water surface waves can induce additional Eulerian-mean flows. These are spatial divergence of the wave field, which drives an Eulerian return flow (Longuet-Higgins and Stewart, 1962), and viscous and Coriolis effects, which result in a so-called Ekman–Stokes flow in the turbulent upper-ocean mixed layer, deflected to the right of the Stokes drift in the Northern Hemisphere (to the left in the Southern Hemisphere). In particular, I have considered the influence of directional spread and density stratification on the divergence-driven return flow, and the role of unsteadiness of the wave field on the Ekman–Stokes Eulerian flow in the upper layer. In combination, the driving mechanisms of spatial divergence and viscosity- and Coriolis-driven Ekman–Stokes dynamics lead to wave-induced Ekman–Stokes pumping, inducing an additional deep return flow which radiates inertia-gravity waves. These wave-induced Eulerian-mean flows must be superimposed on the Stokes drift to obtain the correct wave-induced Lagrangian velocity relevant for material transport and for ocean circulation models.

5.1 Chapter 2: Directional spread and stratification

The leading-order behaviour of the sea surface can be described as a superposition of wavepackets, which is equivalent to the linear superposition of waves possessing different frequencies and directions (Longuet-Higgins, 1984). For an isolated wavepacket, the mass transport by the Stokes drift becomes horizontally divergent due to the slow spatial variation of the wave amplitude on the scale of the packet. Longuet-Higgins and Stewart (1962) demonstrated that the divergence of the Stokes mass transport drives an Eulerian return flow, which is directed opposite to the Stokes drift and is felt throughout the ocean depth. The return flow varies horizontally and vertically on the lengthscale σ of the packet, whereas the Stokes drift is localised near the surface. In this chapter, I have explored the role that weak directional spread of the wavefield and density stratification of the ocean play in the displacement induced by an isolated, quasi-monochromatic, non-dissipating packet.

In an unstratified ocean, I have derived the result that for a 2D (unidirectional) packet, the net displacement by the return flow is negative, constant at all vertical levels z, and scales as σ_x/d, where d is the ocean depth and σ_x is the length scale of the packet. In real oceans, directional spread of the wavefield about the mean propagation direction results in a finite packet width σ_y perpendicular to propagation. The resulting wavepacket is then 3D (directionally-spread) and its induced return flow depends on both horizontal coordinates and the vertical coordinate. For a 3D packet, I have derived the perhaps surprising result that the net displacement by the return flow is in fact zero everywhere in space. Examining the displacement over finite time, for the simplified case of a shallow return flow ($d/\sigma_x \ll 1$), provides some insight into this 2D-3D transition. Initially, particles are displaced as if they were in a 2D return flow: the displacement grows from zero to a maximum (negative) value attained at a time $\approx \sigma_y/c_g$, where σ_y is the packet width and c_g is the group velocity associated with the peak wave component of the packet. After reaching this maximum value, the magnitude of the displacement eventually decreases to zero. The physical reason for this is that on a timescale

$O(\sigma_y/c_g)$ mass begins to return around the packet as well as beneath it, and the flow around the packet induces a positive displacement which undoes the initially 2D-like negative displacement by the return flow. This timescale for transition between 2D-like and 3D-like flow is inversely proportional to the degree of wave directional spreading, captured by the aspect ratio parameter $R = \sigma_x/\sigma_y$. For a 2D packet, $\sigma_y \to \infty$ ($R = 0$) and this compensating portion of the return flow never forms, resulting in a negative net displacement for 2D packets.

When a packet propagates on a stratified ocean, the return flow disturbs the surfaces of constant buoyancy and excites internal gravity waves in the packet's wake. In order for internal waves to be generated, a resonance condition between the group velocity of the surface wavepacket and the phase velocity of the radiated internal waves must be satisfied. Though realistic oceanic stratification is generally too weak to support internal waves in the wake of a 2D packet, internal waves are always generated by a 3D packet. For constant stratification, the 2D net displacement becomes an oscillatory function of depth whose behaviour depends on the parameter Nd/c_g, where N is the Brunt–Väisälä frequency (a measure of the stratification strength), d is the ocean depth, and c_g is the surface wave group velocity. For $\pi/2 < Nd/c_g < \pi$, the displacement near the surface becomes positive while the displacement at depth becomes more negative. When $Nd/c_g \to n\pi$ (with n a positive integer), the displacement becomes extremely large, which corresponds to a resonance between the surface wavepacket and an internal wave whose x-wavenumber $k_n = \sqrt{(N/c_g)^2 - (n\pi/d)^2} \to 0$.

The net displacement again vanishes for a 3D packet, despite the presence of an internal wave wake for $N \neq 0$. The behaviour of the finite-time displacement varies with the stratification strength N and the aspect ratio R. For realistic values of N, the finite-time displacement is only weakly affected by stratification before being reduced to zero by directional spread. At depth, the (small) displacement at early times exhibits oscillatory behaviour due to stratification. Over later times it intensifies in magnitude, as the flow has not yet felt the influence of R. Finally, over very long times it also reduces to zero. The smaller R is, the longer that finite-time

displacement persists, as found in the unstratified case. Though 3D packets are most representative of conditions in the open ocean, the results I have derived for 2D packets may be of use in wave tank/wave flume experiments. Indeed, van den Bremer, Whittaker, et al. (2019) investigated the return flow associated with wavemaker-generated 2D deep-water wavepackets on unstratified water in a series of particle-tracking experiments, finding good agreement with the non-dispersive 2D unstratified net displacements derived in Chapter 2.

5.2 Chapter 3: Ekman–Stokes dynamics

The divergence-driven Eulerian-mean flow examined in Chapter 2 is generally much smaller than the Stokes drift (even for $d/\sigma \lesssim 1$) and has a greater influence at depth. However, in the presence of other effects, waves can induce mean flows of comparable magnitude to the Stokes drift which are localised within the turbulent upper layer of the ocean. By considering the thin viscous boundary layers at the free surface and bottom of the fluid, Longuet-Higgins (1953) showed that vorticity can be slowly advected or diffused into the fluid interior, and the mass transport profile is altered. Just below the $O(\text{mm})$-thick viscous layer at the free surface the wave-induced Eulerian-mean flow experiences a wave stress, such that the shear of the Eulerian flow matches the shear of the Stokes drift (Seshasayanan and Gallet, 2019). In an inviscid, rotating ocean, Hasselmann (1970) demonstrated that rotation drives a cross-wave 'Coriolis–Stokes forcing' (Polton et al., 2005), resulting in a so-called anti-Stokes Eulerian-mean flow which cancels the Stokes drift and excites inertial oscillations. By combining these models with an eddy-viscosity parametrisation for the turbulent upper-ocean layer (e.g. Ekman (1905)), I have examined the Ekman–Stokes Eulerian-mean flow driven by the Longuet-Higgins wave stress and the Coriolis-Stokes forcing (Polton et al., 2005). Using the Laplace transform to solve the Ekman–Stokes equation, I have shown that the solution for the Ekman–Stokes flow is expressed as a convolution between the time-varying surface Stokes drift and an 'Ekman–Stokes kernel'. The Ekman–Stokes kernel has the character of an amplitude-decaying inertial oscillation, and it encodes the development in depth

of the Ekman–Stokes flow over time. This convolution is a low-computational-cost alternative to running a coupled wave-circulation model and may be adapted for linearly-varying eddy viscosity or for broad-banded spectra (see Appendix II).

The Ekman–Stokes flow is found to depend on a non-dimensional parameter D, which is the ratio of the Ekman depth $\delta_{\mathrm{E}} \sim \sqrt{\nu/f}$ to the Stokes depth $\delta_{\mathrm{S}} \sim k_p^{-1}$, where ν is the eddy viscosity, f is the Coriolis frequency, and k_p the peak wavenumber of the wave spectrum. For small $D \ll 1$, the Eulerian dynamics is governed by a (partial) anti-Stokes flow, which reduces the magnitude of the Stokes drift and excites inertial oscillations along the path of a fluid particle. For larger $D \gg 1$, the Ekman–Stokes flow intensifies in magnitude and its direction is more closely aligned with the Stokes drift. Though Stokes drift is increasingly included in studies of marine litter transport, these studies ignore the wave-driven Ekman–Stokes flow (Iwasaki et al., 2017; Onink et al., 2019; van Sebille, Aliani, et al., 2020). By evaluating the unsteady Ekman–Stokes flow for an idealised storm, and then for buoy data obtained from CDIP (https://cdip.ucsd.edu), I have demonstrated that for realistic values of eddy viscosity ($\nu \sim 10^{-3} - 10^{-2}\mathrm{m^2s^{-1}}$), the wave-induced Lagrangian-mean flow differs significantly in both magnitude and direction to the Stokes drift. As a result, the Lagrangian displacement of a floating particle is found to be significantly affected by accounting for the Ekman–Stokes flow. Due to the impact of the Ekman–Stokes flow on the wave-induced transport of floating marine litter, as demonstrated in Chapter 3, marine litter studies should take this Eulerian-mean flow into account. My calculations also show how important it is to factor in the unsteadiness of the Stokes drift, and hence unsteadiness of the Ekman–Stokes response: figure 4 of Chapter 3 shows that the assumption of a steady Lagrangian flow can lead to significant errors in the predicted displacement of floating litter. As the timescale of storms is $O(1/f)$, unsteadiness of the flow is likely to play an important role in the accurate modelling of particle drift. Including the wave-driven Ekman–Stokes flow should also lead to better agreement with observations when the wind and waves are misaligned, e.g. when a distantly-generated group of swell enters a wind-sea of locally-generated waves. The wave-driven Ekman–Stokes flow

may help to partially explain why deflection angles between the wind-driven Ekman current and the wind are observed to be much smaller than predicted by current theory (Lewis and Belcher, 2004; Polton et al., 2005).

5.3 Chapter 4: Ekman–Stokes pumping

I have combined the insights of Chapters 2 and 3 by focussing on the divergence-driven flows which form in response to spatial variation of the Lagrangian-mean flow in the upper layer. While the Ekman–Stokes flow arises at the same order of perturbation as the Stokes drift, these divergence-driven flows are weaker by a small bandwidth parameter $\varepsilon = (2k_p\sigma_x)^{-1} \ll 1$ where σ_x is the characteristic scale of horizontal variation of the wave amplitude and k_p the peak wave frequency. Using boundary-layer methods, I have separated the problem into two regions: the Ekman–Stokes (upper) layer of depth $\delta_{\mathrm{E}} \sim \sqrt{\nu/f}$, and an 'outer layer' beneath this, in which the flow varies vertically on the packet scale σ_x. In the upper layer, the divergence of the wave-induced Lagrangian-mean flow $\boldsymbol{u}_{\mathrm{L}}$ results in a weak vertical velocity, which in turn causes slow upwelling and/or downwelling of mass over the scale σ_x of wave-field variation. This 'Ekman–Stokes pumping' (vertical) velocity is given by the horizontal divergence of the Lagrangian mass transport (depth integral of $\boldsymbol{\nabla}_{\mathrm{H}} \cdot \boldsymbol{u}_{\mathrm{L}}$), and in the steady (time-independent) case is equal to the curl of the wave stress divided by the Coriolis frequency f. The steady expression is in conceptual agreement with the expression for steady wind-driven Ekman pumping, which is given by the curl of the wind stress divided by f. This implies that a large group of non-dissipating swell will induce weak downwelling as it approaches and the wave amplitude increases, followed by weak upwelling as it passes by and the wave amplitude decreases, while exciting weak inertial oscillations. Consequently, sea states which exhibit group-like spatial structure may influence mixing in the upper ocean. Where winds converge/diverge, the associated local wind sea will contribute an additional weak wave-induced downwelling/upwelling. Though it is often assumed that the wind and wave directions are closely aligned, this may not always be true, for example in the case of distantly generated swell entering a

local wind sea. Wave pumping due to swell may contribute to the unsteadiness and 'leakiness' of the plastic garbage patches, which roughly coincide with the centres of large ocean gyres (Lebreton, Greer, et al., 2012; van Sebille, Aliani, et al., 2020).

A deep Eulerian return flow of the type explored in Chapter 2 of this thesis forms in the outer layer in response to the divergence-driven Ekman–Stokes pumping velocity w_2. At the top of the outer layer, the vertical velocity component of the outer flow is given by the divergence of the Lagrangian mass transport. The Ekman–Stokes mass transport $\mathbf{M}$ is given by a convolution between the surface Stokes drift and an inertial oscillation of spatial period $2\pi c_g/f$, and its amplitude is set by two dimensionless parameters $\nu^* = 4k_p^2\nu_0\sigma_x/c_g$ and $r^* = f\sigma_x/c_g$. For realistic wave parameters typical of swell seas, the magnitude of $\mathbf{M}$ is approximately 5% of the magnitude of $\mathbf{M}_{\mathrm{S}}$, and so the Lagrangian transport $\mathbf{M}_{\mathrm{L}}$ is very weakly affected by Earth's rotation. However, when r^* is appreciably large due to a strong rotation rate or a synoptic-scale, slow-moving packet, $\mathbf{M}$ consists of a train of spatially-periodic inertial oscillations of large magnitude, so that the Lagrangian mass transport $\mathbf{M}_{\mathrm{L}} = \mathbf{M}_{\mathrm{S}} + \mathbf{M}$ is visibly affected by rotation.

Beneath the Ekman–Stokes layer the eddy viscosity is assumed to be zero, so the dynamics are driven by pressure gradients, the Coriolis force, and density stratification. When the nontraditional (horizontal) Coriolis component is neglected, the equation of motion for the vertical velocity takes the form of an inertia-gravity wave equation. This can be solved for constant stratification by taking a Fourier transform in the horizontal variables and solving the Fourier-space ordinary differential in the vertical coordinate Z. Alternatively the governing equation can be projected onto a set of vertical modes, as done in the stratified, nonrotating case by Haney and Young (2017).

When the stratification frequency $N = 0$, the impact of f on the return flow is negligible for all but very strong rotation rates. The weak effect of realistic rotation in unstratified oceans is most noticeable in 2D return flows, since rotation induces a small transverse velocity component whose amplitude scales as r^*. In the rapidly-rotating limit a train of inertial oscillations appears behind the packet,

corresponding to a resonance between the surface wave group velocity and the phase velocity of a spatially-varying inertial wave mode. Further complicating the structure of the return flow for large $r^* \gtrsim O(10^{-1})$ is the 'delocalisation' of the boundary-layer forcing: when rotation is strong, the spatially-periodic (with period $2\pi c_g/f$) inertial imprint of the Ekman–Stokes transport $\mathbf{M}$ on $\mathbf{M}_{\mathrm{L}}$ becomes larger in magnitude, and $\mathbf{M}_{\mathrm{L}}$ extends far behind the packet along the negative $\tilde{x}$-axis, where $\tilde{x}$ is the comoving frame of the packet. This effectively results in a superposition of packet-like forcing approximately regularly spaced at intervals of $2\pi c_g/f$, leading to stronger return-flow velocities far behind the packet. In an unstratified or very weakly-stratified ocean such that $0 \leq N \leq f$, rotational effects only have a meaningful impact on the 3D return flow in the strong-rotation limit $r^* \gtrsim 10^{-1}$.

The Coriolis force has the greatest impact on the return flow induced by a long packet ($\sigma_x \sim 10^3$ m) when acting in conjunction with stratification ($N \neq 0$). Instead of the group velocity matching the x-phase speed of an internal wave, as in Haney and Young (2017), a resonance occurs between the surface wave group velocity and the x-phase speed of an inertia-gravity wave mode. In a nonrotating, stratified ocean, Haney and Young (2017) found that there was a minimum value of N for which internal-wave radiation by a 2D packet can occur. The Coriolis force allows 2D packets to radiate inertia-gravity waves for slightly weaker values of stratification than the lower bound in Haney and Young (2017). Additionally, a 2D return flow will be accompanied by a y-independent transverse component of comparable magnitude to the x-velocity. A wake of inertia gravity waves is always present in 3D, since the extra degree of freedom permits inertia-gravity modes to satisfy the resonance condition by propagating obliquely to the packet's direction of propagation. For a 3D return flow, realistic rotation introduces slight asymmetry of the stratified inertia-gravity wave wake about the centreline of the packet, with the greatest impact on the transverse and vertical velocity components at depth. Rotation also slightly increases the wake angle, with the greatest impact on the inertia-gravity waves with higher mode number. In the weak-stratification limit in which $N \approx f$, a peculiar cancellation occurs between the effects which rotation and

stratification induce. The return flow becomes nearly identical in form to that of a potential return flow which is forced not by the divergence of Stokes transport condition in chapter 2, but by the Ekman–Stokes pumping condition, and no inertia-gravity waves appear in the packet's wake. This suggests that in polar regions where the ocean is very weakly stratified and $N \approx f$, the return flow can be approximated by using the potential flow expressions of Chapter 2 with $\mathbf{M}_{\mathrm{L}}$ in place of $\mathbf{M}_{\mathrm{S}}$.

5.4 Recommendations for future work

The work in this thesis should be built upon in the following six ways. First, future work should investigate possible instabilities of the wavetrain and the induced Eulerian-mean flow which are neglected herein. Second, predictions of the Ekman–Stokes flow and Ekman–Stokes pumping are sensitive to the value of the surface wave stress and the eddy-viscosity parametrisation of the turbulent mixed layer. Developing improved eddy-viscosity models, and adopting a more careful assessment of the high-frequency tail of empirical wave spectra, therefore represents important future work. Third, calculations involving the Coriolis force should aim to include the nontraditional (horizontal) Coriolis component, particularly when examining deep Eulerian return flows. Fourth, the assumptions of weak background flow should be relaxed, since doing so would permit an examination of the rich dynamics modelled by the full Craik-Leibovich equations. Fifth, though this thesis has focussed on deep-water conditions, the analysis presented herein should certainly be extended to water of arbitrary depth. Finally, the results derived herein may be applied to the case of a random sea state, which causes wave-induced dispersion of particles.

5.4.1 Instabilities

Though I have considered the leading-order effects of amplitude dispersion arising at $O(\alpha^2\varepsilon^2)$ and found these to be small in Chapter 2, dispersive effects may still play a role in the displacement induced by surface gravity wavepackets. Over time, nonlinear interactions between the wave components in the packet will also lead to the packet broadening in the cross-wave direction and contracting in the

along-wave direction, causing the narrow-banded/quasi-monochromatic assumption to break down after nonlinear focus of the packet (Adcock et al., 2015). Carrying the quasi-monochromatic mean-flow calculation to $O(\alpha^2\varepsilon^3)$, the wavepacket develops an asymmetry between its leading and trailing edges, indicative of the disintegration of the wavepacket due to linear dispersion. For wave groups of finite steepness $\alpha = A_p k_p$, the governing equations must be considered to $O(\alpha^3)$. At this order of perturbation, the wavetrain becomes unstable to nonlinear perturbations of the dispersion relationship by the Eulerian return flow, as shown by (Dysthe, 1979; Taklo et al., 2017) using a modified nonlinear Schrödinger equation.

Seshasayanan and Gallet (2019) note that the steady-state Ekman–Stokes spiral (described by equation 7 in Chapter 3) is unstable to wavelike perturbations. Shrira and Almelah (2020) report a similar instability for the transient motions induced by a suddenly-imposed constant wind or wave stress. Investigation of these instabilities and how they interact with unsteadiness of the mean flow represents a largely unexplored and important area of research.

5.4.2 Wave stress and eddy viscosity

For a broad-banded wave spectrum, the high-frequency (hence high-wavenumber) content of the spectrum leads to a Stokes drift which is much more strongly sheared near the surface and persistent at depth (Breivik, Bidlot, et al., 2016). As a result, the Stokes depth δ_S is smaller and the value of D is larger. My analysis in Chapter 3 indicates that the Ekman–Stokes response to a broad-banded wave spectrum will therefore be more closely aligned with the Stokes drift and less influenced by rotation than for a monochromatic spectrum with an equivalent peak frequency ω_p. The Ekman–Stokes response to a general broad-banded spectrum can be calculated by approximating the integral over wave frequency involved in broad-band spectra (Kenyon, 1969) by a finite sum; the contributions to the Eulerian-mean flow are calculated from the Ekman–Stokes kernel on a per-frequency basis, and these are summed to obtain the complete response. However, most empirical wave spectra have high-frequency tails that behave like ω^{-4} or ω^{-5}. Since the shear of the Stokes

drift is given by the fifth moment of the wave spectrum, it is therefore undefined at $z = 0$, as noted in Breivik, Bidlot, et al. (2016). In appendix II I adopt a high-frequency cut-off $\omega_c \gg \omega_p$ to obtain a finite Ekman–Stokes response. I also find that, for the very shallow Stokes depths which occur under broad-banded spectra, the constant eddy viscosity assumption is likely to break down and a more realistic linear viscosity model should produce more accurate results. The development of improved models for the high-frequency tails of broad-banded spectra which allow for estimation of the surface wave stress represents important future work.

Though the eddy viscosity is generally treated as constant in time, Price and Sundermeyer (1999) note that the simplifying assumption of a time-independent eddy viscosity is unjustified, since it neglects processes such as wave breaking and restratification of the mixed layer due to diurnal cycling. Shrira and Almelah (2020) have presented a solution method which can account for a time-dependent viscosity $\nu(z, t)$, which should lead to better agreement with observations. As noted in Chapter 3, unsteadiness of the flow is a crucial ingredient in accurate estimates of the effect of wind and wave driven effects on drift of floating litter. Future studies which include the wave-induced Ekman–Stokes flow should therefore also consider the time-variation and depth-dependence of the eddy viscosity.

In the Ekman–Stokes pumping calculations undertaken in Chapter 4, I have shown that the pumping velocity at the base of the mixed layer (which acts as a forcing on the return flow) is independent of the viscosity profile, other than its surface value $\nu(0)$. Accurate estimation of the eddy viscosity near the surface is therefore important. A range of viscosities can be inferred from the Mellor-Yamada 2.5-level turbulence closure model by assuming the law of the wall (Mellor and Blumberg, 2004), but improved eddy viscosity models are dependent on better parametrisation of the turbulence in the upper layer. In addition, many eddy-viscosity parametrisations often require the estimation of the sea-surface roughness length scale z_* in order to obtain a finite surface value of the induced mean flow velocity. As noted by Drennan et al. (2005), different roughness length scale parametrisations perform better in different sea states, so it may be important that

the sea state is taken into account when creating a global model of Ekman–Stokes pumping (c.f. studies such as McWilliams and Restrepo (1999)).

5.4.3 Nontraditional effects

In Chapter 4 I have derived the return flow and displacements under the Traditional Approximation (TA) by neglecting the nontraditional Coriolis component $\tilde{f}\hat{\boldsymbol{y}}$, where $\hat{\boldsymbol{y}}$ is the unit vector in the Northwards direction. The nontraditional Coriolis component couples horizontal motion to vertical motion and is often neglected using a thin-layer approximation, or by assuming that the vertical velocity is much weaker than the horizontal ones. However, when the effect of density stratification is incorporated into the return flow calculation, vertical velocities associated with the inertia-gravity wave wake may be large enough to feel the effects of $\tilde{f}$. Though $\tilde{f}$ is largely neglected in calculations of surface wave-induced flows, Ekman–Stokes pumping possibly represents a scenario in which nontraditional effects are important. The impact of $\tilde{f}$ should therefore be carefully examined, potentially by solving the fully nontraditional equations for the return flow components U, V and W which I have derived in Chapter 4. In particular, I anticipate that the depth structure and magnitude of the nontraditional deep return flow will depend on the direction of the Lagrangian mass transport $\mathbf{M}_{\mathrm{L}}$ with respect to the (Eastward) x-axis. This dependence on direction should also follow through to the net and finite-time displacements: by time-integrating the momentum equations, one may conclude that (small) nonzero displacements arise as a result of quasi-hydrostatic, geostrophic balance for typical oceanic conditions.

5.4.4 Background flow

Throughout this thesis, I have ignored interactions between the Stokes drift, wave-induced flow, and the non-wave background flow. This background flow consists of a complex mixture of wind-driven Ekman currents, geostrophic and barotropic flows, currents, turbulence, and mesoscale and submesoscale eddies. Though wave effects, for example the Coriolis–Stokes forcing, are increasingly included in general

circulation models, the interaction between the wave-induced Lagrangian-mean flow and background (non-wave) circulation is less well-studied (McWilliams and Restrepo, 1999; Onink et al., 2019).

Using perturbation methods, Craik and Leibovich (1976) derived a second-order equation which accounts for interactions between the Stokes drift and the total Eulerian-mean flow (the sum of the wave-induced and non-wave induced mean flows). The Stokes vortex force, $\boldsymbol{\nabla} \times \boldsymbol{u}_{\mathrm{s}} \times \overline{\boldsymbol{u}}$, describes how the interaction between the vorticity of the Stokes drift and the wind-driven Ekman flow leads to the so-called Craik–Leibovich instabilities, which result in the formation of Langmuir circulations - long, parallel, counterrotating rolls between which debris accumulates. When wind forcing is weak, the Ekman–Stokes flow should also drive Craik–Leibovich instabilities at fourth order in wave steepness.

Though the Ekman–Stokes pumping calculation in Chapter 4 is presented in the form of a wavepacket calculation similar to those in Chapter 2, it may be useful to approach it without making a packet assumption. This would be equivalent to examining the evolution of the mean flow within a fixed area in response to, e.g. a synoptic-scale pressure variation, or to a storm surge associated with a slowly-moving weather system. Relaxing the small-Rossby number assumption employed in Chapter 4 would also allow for interaction between the Ekman–Stokes-driven return flow and background geostrophic/barotropic motions, the latter of which which may be as large as $O(1)$ or $O(\alpha)$. The resulting calculation could be viewed as a viscous, nonlinear extension to Hasselmann (1970)'s analysis of inertial wave-generation by a periodic surface wave on a rotating ocean. I believe that such a calculation could be of use to researchers who study near-inertial wave generation in the open ocean, and could be incorporated into ocean general circulation models.

5.4.5 Finite depth

This thesis has focussed on deep-water conditions typical of the open ocean. It is generally accepted that the majority of marine plastic pollution enters the ocean from land-based sources (Andrady, 2011), though a significant share also originates

from ocean-based sources. In order to improve our understanding of the distribution of pollutants in the ocean, it is therefore crucial to accurately model the transport processes and mean flows in coastal regions and waters of finite depth. Recent studies have indicated an important role for Stokes drift in coastal upwelling/downwelling (Wu et al., 2019), and since wave crests become asymmetric and sharper as waves shoal while the troughs flatten and broaden (e.g. Elgar and Guza (1985)), the Stokes drift also intensifies towards the coast. As waves move into coastal waters and start to feel the seabed, they lose energy due to bottom friction. As Longuet-Higgins (1953) demonstrated, this leads to streaming in the viscous bottom boundary layer, which affects the mass transport profile. Work has already been done by Calvert et al. (2019) to extend the unstratified, non-rotating return flow calculation and the associated displacements to arbitrary water depth. This is a good starting point for future work, which should focus on the wave-induced mean flows which form in coastal regions, and how these affect mass transport and beaching of pollutants released from land-based sources and beaches.

The wavepacket-induced return flow was examined in rotating shallow water by Thomas et al. (2018), who used a Helmholtz decomposition to demonstrate that the Lagrangian flow consists of a potential-flow component (described by a divergent potential ϕ^{L}) and a Coriolis-induced anticyclonic component (described by a rotational streamfunction ψ^{L}). In the strong-rotation limit, the anticyclonic flow grows in magnitude, and the Lagrangian-mean flow is confined to the 'footprint' of the wavepacket. This has important implications for wave-induced particle dispersion, which I briefly discuss below.

5.4.6 Dispersion

Herterich and Hasselmann (1982) demonstrate that random surface waves, through the interaction of their associated Stokes drifts, can contribute to the random dispersion of particles, although this is generally thought to be a small effect over scales larger than a few tens of kilometres. Given a random ensemble of waves, a particle will tend to follow the random Stokes drifts of each wave component,

giving rise to a Brownian diffusion of the particle at fourth order in wave steepness. The diffusion coefficient is given by the auto-correlation of the Lagrangian drift $\boldsymbol{u}_{\mathrm{L}}$ evaluated at zero frequency, $D(\tau) = \langle \boldsymbol{u}_{\mathrm{L}}(t)\boldsymbol{u}_{\mathrm{L}}(t+\tau)\rangle$, where angle brackets denote an expectation value. For an irrotational flow, the Eulerian return flow does not contribute to the dispersion (this can be verified by taking $\omega_1 = \omega_2$ in the second-order kernels of Herbers and T. Janssen (2016)). However, Bühler and Holmes-Cerfon (2009) found that in rotating shallow water the Eulerian return flow does affect the particle dispersion. In fact, in the strong-rotation limit when f is large, the dispersion of Lagrangian particles is 'choked'. This hints to the potentially important yet largely unexplored role the Coriolis force plays in wave-induced particle dispersion. Future work should evaluate the second-order kernels for the Eulerian return flow in rotating water of arbitrary depth, and calculate the dispersion that results. I anticipate that the Eulerian return flow will affect the Lagrangian dispersion, and 'choke' it in the strong-rotation limit. Though preliminary calculations suggest that constant stratification may not affect the Lagrangian diffusivity, stratification may play a role when combined with rotation, as noted in Chapter 4 of this thesis.

Appendices

.1 Appendix: Inclusion of the set-down

In this appendix, we consider how the set-down of the wave-averaged free surface, h_2, affects the net displacement by a 2D return flow. We have previously used the rigid-lid approximation to neglect the set-down (given by (2.5)), which corresponds to ignoring $\partial_t^2\phi_2$ on the left-hand side of (2.4) when calculating the return-flow potential. Up to $O(\alpha^2\varepsilon^3)$ the overbarred term in (2.4) is zero and the Stokes transport M remains unchanged, so only the linear operator acting on ϕ_2 is altered by including the set-down,

$$\left(\frac{c_g^2}{g}\partial_{\tilde{x}}^2 + \partial_z\right)\phi_2\Big|_{z=0} = \partial_{\tilde{x}}M, \tag{1}$$

where we have moved into the group frame $\tilde{x} \equiv (x - c_g t)$. The solution to the Laplace equation which obeys (1) and a no-flow bottom boundary is

$$\phi_2 = \frac{\omega_0 a_0^2 \sigma_x \sigma_y}{8\pi} \iint_{\mathbb{R}^2} \frac{ike^{-k^2\sigma_x^2/4 - l^2\sigma_y^2/4}}{\sqrt{k^2+l^2} - \frac{\varepsilon c_g^2 k^2}{g\tanh(d\sqrt{k^2+l^2})}} \frac{\cosh((z+d)\sqrt{k^2+l^2})}{\sinh(d\sqrt{k^2+l^2})} e^{ik\tilde{x}} e^{ily} dk dl. \tag{2}$$

This is similar to (2.16), but the denominator is now modified due to the set-down term; since $k^2/\tanh\left(d\sqrt{k^2+l^2}\right)$ is always positive, the set-down enhances the return flow. As we have shown that the net displacement disappears in 3D (see (2.17)) but is 2D-like for short times (see §2.2.4, $t_{\mathrm{I}} < \sigma_y/c_g$), we will only consider the 2D displacement here. The horizontal velocity in 2D is given by

$$u_2 = -\frac{\omega a_0^2 \sigma_x}{4\sqrt{\pi}} \int_{-\infty}^{\infty} \frac{ke^{-k^2\sigma_x^2/4}}{1 - \frac{\varepsilon c_g^2 k}{g\tanh(kd)}} \frac{\cosh\left(k\left(z+d\right)\right)}{\sinh\left(kd\right)} e^{ik\tilde{x}} dk. \tag{3}$$

Integrating over all time (all $\tilde{x}/c_g$ in the co-moving packet frame) results in a delta-function at $k = 0$, so the net displacement (dimensional and scaled respectively) is

$$\Delta x = -\frac{\omega_0 a_0^2 \sqrt{\pi}}{2c_g} \frac{\sigma_x}{d} \frac{1}{\left(1 - \varepsilon c_g^2/(gd)\right)}, \qquad \Delta x^* = -\frac{1}{d^*} \frac{1}{(1 - \varepsilon^2/(2d^*))}, \tag{4a,b}$$

with $d^* \equiv d/\sigma_x$ the ocean depth scale with respect to the packet length. Inclusion of the set-down in 2D therefore results in multiplication of the net displacement by $(1 - \varepsilon c_g^2/gd)^{-1}$, which may alternatively be written as $(1 - \varepsilon^2/(2d^*))$ using

the definition $\varepsilon \equiv (2k_0\sigma_x)^{-1}$. Hence, when $k_0 d \gg 1$ and $\varepsilon \ll 1$ such that $d^* = 2\varepsilon(k_0 d) \gg 1$, it is justified to make the rigid-lid approximation by neglecting $\partial_t h_2$ in (2.1b) when calculating the leading-order return flow in deep water. We note from (4b) that the effect of the set-down is largest when the return flow is 2D ($R = 0$) and shallow ($d^* \equiv d/\sigma_x \ll 1$); for a large bandwidth $\varepsilon = 0.125$ and a depth scale $d^* = 1/2$, the correction is about 3%.

.2 The leading-order effect of wave dispersion

In this appendix, we explore the effect of wave dispersion on the net Lagrangian displacement in unstratified flow, over times t satisfying $\varepsilon^2 t = O(1)$. To do so, we update the linear quantities (2.2) to include dependence on a slow timescale $T = \varepsilon^2 t$ in §.2.1 (see also e.g. Kinsman, 2002), and in §.2.2 we determine the mean-flow forcing equation (2.4) at $O(\alpha^2\varepsilon^2)$ accordingly, examining the full 3D case.

.2.1 First-order solutions $O(\alpha)$

From the combined linear boundary condition $(\partial_t^2 + g\partial_z)\phi_1|_{z=0} = 0$, we obtain an evolution equation for A_0 in terms of the $O(\varepsilon^2)$ timescale and its Fourier-space solution,

$$\partial_T A_0 = i\frac{c_g^2}{2\omega_0}\partial_{\tilde{x}\tilde{x}} A_0, \qquad \hat{A}_0(k,l,T) = \hat{A}_0(k,l)e^{ik^2\gamma_0 T/2}, \tag{5a,b}$$

where $\gamma_0 \equiv \partial^2\omega_0/\partial k_0^2 = -\sqrt{g/k_0^3}/4$ is the dispersive parameter. Assuming the surface profile is Gaussian, inverting the transform (5b) shows that the surface maintains its Gaussian shape, but now evolves on the slow, dispersive timescale,

$$A_0\left(x,y,T\right) = a_0^{\text{Disp}} e^{-\tilde{x}^2/\left(2\left(\sigma_x^{\text{Disp}}\right)^2\right)} e^{-y^2/\left(2\sigma_y^2\right)}, \tag{6}$$

where the 'Disp' superscript denotes inclusion of leading-order dispersion, and slowly-varying parameters are

$$a_0^{\text{Disp}} = \frac{a_0}{\sqrt[4]{1+\gamma_0^2 t^2/\sigma_x^4}}, \qquad \sigma_x^{\text{Disp}} = \sigma_x\sqrt{1+\gamma_0^2 t^2/\sigma_x^4}. \tag{7a,b}$$

Dispersion is hence important for times $\gtrsim \sigma_x^2/|\gamma_0|$. Over time, the packet decreases in amplitude and widens as it translates at the group velocity c_g. It is therefore no longer steady in its own reference frame.

.2.2 Second-order solutions $O(\alpha^2)$

From appendix .1 the set-down contribution is $O(\varepsilon^2/d^*)$, so we include the ∂_t^2 term on the left-hand side of (2.4), whilst emphasising that this term is due to the

set-down rather than wave dispersion. It is found that $O(\alpha^1\varepsilon^1)$ terms in (2.2a,b) do not contribute to the right-hand side of (2.4) at $O(\alpha^2\varepsilon^2)$; the wave forcing obtained by multiplying $O(\alpha^1\varepsilon^1)$ terms by $O(\alpha^1\varepsilon^0)$ terms in (2.2) disappears under wave-averaging. Consequently, we need only account for functional dependence of A_0 (see (5)) on $T = \varepsilon^2 t = O(1)$ to calculate the updated M. At $O(\alpha^2\varepsilon^2)$, the mean flow is still forced solely by the Stokes transport, which is now slowly evolving. The boundary condition for ϕ_2 is

$$\left(\frac{c_g^2}{g}\partial_{\tilde{x}}^2 + \partial_z\right)\phi_2^{\mathrm{Disp}}\bigg|_{z=0} = \partial_{\tilde{x}} M^{\mathrm{Disp}}. \tag{8}$$

Solving (8) in Fourier space, we obtain

$$\phi_2^{\mathrm{Disp}} = \frac{\omega_0 |a_0^{\mathrm{Disp}}|^2 \sigma_x^{\mathrm{Disp}} \sigma_y}{8\pi} \iint_{\mathbb{R}^2} \frac{ike^{-k^2\left(\sigma_x^{\mathrm{Disp}}\right)^2/4 - l^2\sigma_y^2/4}}{\sqrt{k^2+l^2} - \frac{\varepsilon c_g^2 k^2}{g\tanh(d\sqrt{k^2+l^2})}} \frac{\cosh((z+d)\sqrt{k^2+l^2})}{\sinh(d\sqrt{k^2+l^2})} e^{ik\tilde{x}} e^{ily} dkdl. \tag{9}$$

The finite-time 3D return flow displacement is expressed as the triple integral (with $\hat{t} = c_g t/\sigma_x$ dimensionless packet-time, $\kappa = k\sigma_x$ and $\lambda = l\sigma_y$),

$$\Delta x^{*,\mathrm{Disp}}(\tau, R, z^*) = -\frac{1}{2\pi^{3/2}} \iint_{\mathbb{R}^2} \int_0^\tau \frac{\kappa^2 e^{-\lambda^2/4} e^{-\kappa^2\left(1+\varepsilon^2\hat{t}^2\right)/4}}{\sqrt{\kappa^2+R^2\lambda^2} - \frac{\varepsilon^2\kappa^2}{\tanh\left(d^*\sqrt{\kappa^2+R^2\lambda^2}\right)}} \cos\left(\kappa\hat{t}\right) \times \frac{\cosh\left(\left(z^*+d^*\right)\sqrt{\kappa^2+R^2\lambda^2}\right)}{\sinh\left(d^*\sqrt{\kappa^2+R^2\lambda^2}\right)} d\kappa d\lambda d\hat{t}. \tag{10}$$

Using complex exponentials, we can first exactly evaluate the finite-time integral

$$\int_0^\tau e^{-\frac{\varepsilon^2\kappa^2\hat{t}^2}{4}} \cos\left(\kappa\hat{t}\right) d\hat{t} = \frac{\sqrt{\pi}}{2\kappa} \frac{e^{-\frac{1}{\varepsilon^2}}}{\varepsilon} \mathrm{Re}\left\{\mathrm{erf}\left(\frac{\varepsilon\kappa\tau}{2} + \frac{i}{\varepsilon}\right)\right\}. \tag{11}$$

In the long-time limit, (11) is dominated by its behaviour near $\kappa = 0$ (e.g. the delta-function result (2.17)), and so over long times we must expand the error function for $\varepsilon\kappa\tau \ll 1/\varepsilon$ when $\tau \gg 1$. Taking $\exp(-\varepsilon^2\kappa^2\tau^2/4) \approx 1$, the dispersive correction is $O(\varepsilon^2)$:

$$\frac{\sqrt{\pi}e^{-\frac{1}{\varepsilon^2}}}{2\varepsilon} \mathrm{Re}\left\{\frac{1}{\kappa}\,\mathrm{erf}\left(\frac{\varepsilon\kappa\tau}{2} + \frac{i}{\varepsilon}\right)\right\} = \frac{\sin(\kappa\tau)}{\kappa}\left(1 + \frac{\varepsilon^2}{2} + O(\varepsilon^4)\right). \tag{12}$$

The delta function results implies the condition $\varepsilon\kappa\tau \ll 1/\varepsilon$, which suggests we must expand the error function as in (12) to be consistent with the separation of scales.

While the net displacement remains zero in 3D ($\sin(\kappa\tau)/\kappa \to \pi\delta(\kappa)$ as $\tau \to \infty$), dispersion weakly enhances the finite-time displacement.

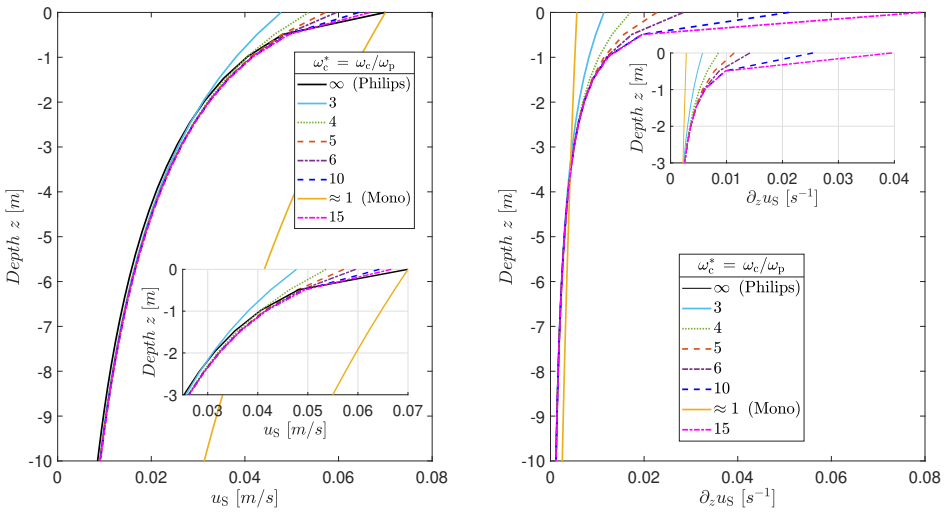

Figure 1: Approximations to the Philips Stokes drift profile (on left) and Stokes drift shear profile (on right) using a discrete number (200) of monochromatic wave components, for different cut-off frequencies ω_c^*. The small sub-panels show a zoomed-in view near $z = 0$. In the right panel, the black line stops at $z = -1$, since the shear of the Stokes drift becomes ill-defined near the surface. The black line is therefore obscured by the purple, blue, and magenta lines.

.3 Appendix: Broad-banded spectra

Results for broadbanded spectra can be approximated by calculating the per-wavenumber contributions to the Eulerian flow using the Ekman–Stokes kernel, and then summing these to obtain the full response. However, most broad-banded empirical spectra have ω^{-5} tails. Since the shear of the Stokes drift is given by the *fifth* moment of the spectrum, the surface wave stress is therefore ill-defined, as noted in Breivik, Bidlot, et al. (2016). In order to obtain a finite value, it is necessary either to choose a high-frequency spectral cut-off ω_c or to evaluate the shear at some nonzero depth $-k_p^{-1} \ll z' < 0$.

Here I have adopted the cut-off approach for the purposes of illustration. Using the idealised Gaussian storm and the same values for ν and f as in §3.1 of Chapter II with a peak frequency $\omega_p = 2\pi/10$ s^{-1}, the response to a (unidirectional) Philips spectrum is found by evaluating the per-wavenumber contributions to the Eulerian flow, and then summing up a finite number of these to approximate the complete response. This is shown in figure 1, where I have summed 200 monochromatic waves

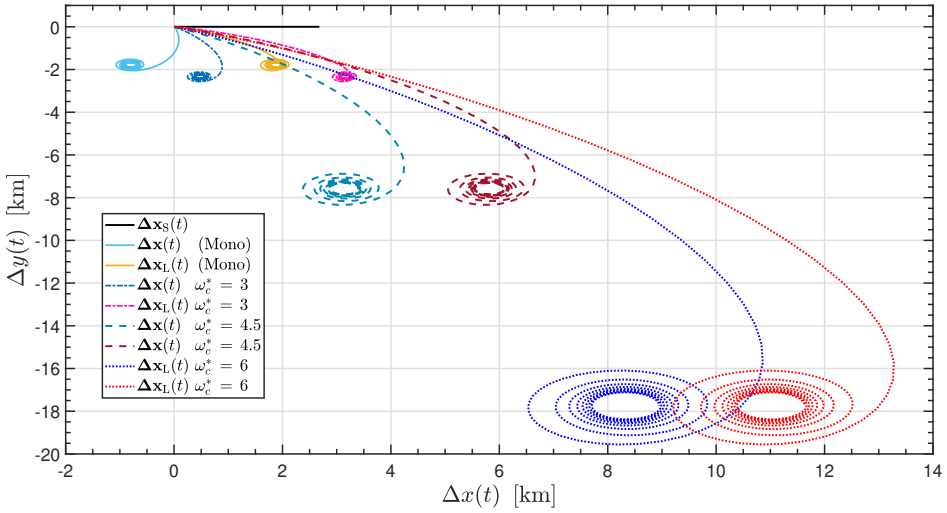

Figure 2: Second-order displacements formed in response to an idealised 24-hr Gaussian storm by waves following a Philips spectrum in the Northern Hemisphere, for a constant viscosity value $\nu = 1 \times 10^{-2}$ m^{2}s^{-1} for different high-frequency spectral cut-offs ω_c.

with frequencies between the peak frequency ω_p and the cut-off frequency $\omega_c = \omega_c^* \omega_p$ to obtain the Stokes drift for a Philips spectrum. As the cut-off is increased, the finite-sum approximation to the Philips profile clearly becomes better, particularly for the Stokes drift depth profile. Monochromatic Eulerian and Lagrangian are plotted in light blue and yellow respectively. The cut-off frequencies for the broadbanded spectra are chosen to be $3\omega_p$ (dash-dotted; dark blue, magenta), $4.5\omega_p$ (dashed; turquoise, maroon) and $6\omega_p$ (dotted; blue, red). It is clear that the Eulerian current becomes extremely large as the cut-off is increased. This is unsurprising, since the better the approximation to the Philips spectrum is, the more unphysically-large the wave stress becomes. As the Stokes depth is much shallower for a broad-banded spectrum (see e.g. Breivik, P. Janssen, et al. (2014)) the assumption of a constant eddy viscosity likely breaks down, since as the cut-off frequency is increased and the spectrum better approximates the Philips spectrum, the Stokes depth decreases. This in turn implies that the waves don't experience the larger eddy viscosity values deep within the turbulent mixed layer. Adopting the more realistic model of an eddy viscosity which linearly increases with depth would require the Ekman–Stokes kernel to be rederived. However, an average Stokes depth for the frequency range

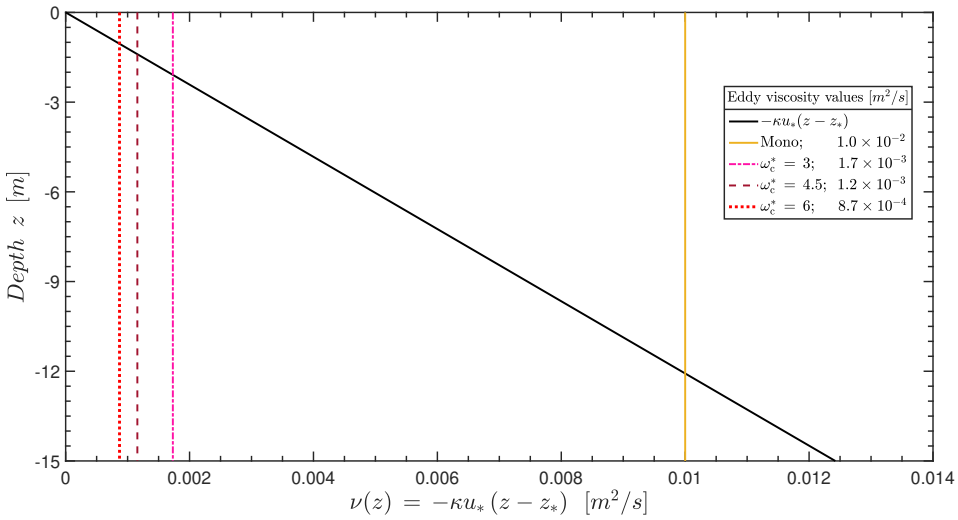

Figure 3: Constant-viscosity approximation to a full linearly-increasing viscosity model, dependent on the high-frequency spectral cut-off ω_c. The z-values of coordinates where vertical lines intersect the black line correspond to the average Stokes depth $\overline{\delta_{\mathrm{S}}}$.

$\omega \in (\omega_p, \omega_c)$ can be found by evaluating $\overline{\delta_{\mathrm{S}}} = \overline{g/(2\omega^2)}$, and a constant viscosity can be chosen which is representative of the value of a more realistic linear model at that depth. A linear viscosity model is $\nu(z) = -\kappa u_*(z - z_*)$ where $\kappa = 0.4$ is von Karman's constant, u_* is the friction velocity (linked to the wind speed at 10 m above the sea surface by $u_* \approx 0.04 U_{10}\sqrt{\rho_{air}/\rho_{water}}$) and z_* is the surface roughness lengthscale $\sim 0.04/30$ m (Madsen, 1977). Using the peak frequency of the wave spectrum ω_p to fit $\nu\left((2\omega_p^2/g)^{-1}\right) = 1\times10^{-2}$ m^{2}s^{-1} allows u_* and hence $\nu(0)$ to be determined. From this linear model, the constant viscosity value $\nu_c \equiv \nu(\overline{\delta_{\mathrm{S}}})$ can be found, where $\overline{\delta_{\mathrm{S}}}$ is the mean Stokes depth of the spectrum calculated for each choice of spectral cut-off ω_c. Evaluating the Ekman–Stokes kernel using this constant value ν_c allows some of the realism of a linear model to be captured. The resulting Eulerian current is much better-behaved, indicating that a linear eddy-viscosity model will likely perform much better for a broad-banded spectrum. Notwithstanding the improved prediction of the Ekman–Stokes flow using a linear viscosity model, lack of knowledge concerning the behaviour of the high-frequency spectral tail remains the largest obstacle to evaluating the wave-induced Eulerian-mean flow.

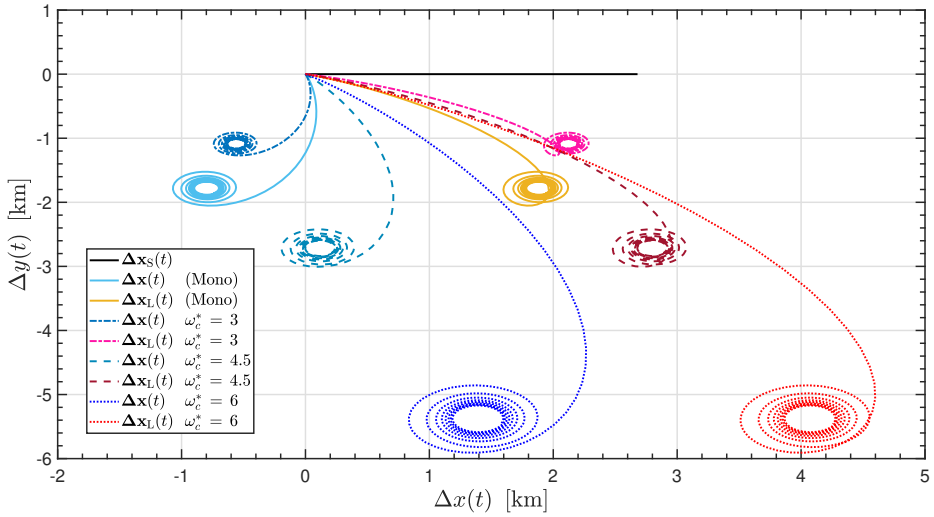

Figure 4: Top: Second-order displacements formed in response to an idealised 24-hr Gaussian storm by waves following a Philips spectrum in the Northern Hemisphere, for a constant viscosity value taken from a linear profile $\nu = -\kappa u_*(z - z_*)$ for different high-frequency spectral cut-offs ω_c.

References

Adcock, T. A. A. et al. (2015). "Nonlinear dynamics of wave-groups in random seas: unexpected walls of water in the open ocean". In: *Proceedings of the Royal Society A: Mathematical, Physical and Engineering Sciences* 471.2184, p. 20150660. DOI: 10.1098/rspa.2015.0660.

Andrady, A. L. (2011). "Microplastics in the marine environment". In: *Mar. Pollut. Bull.* 62.8, pp. 1596–1605. DOI: 10.1016/j.marpolbul.2011.05.030.

Andrews, D. G. and M. E. McIntyre (1978). "An exact theory of nonlinear waves on a Lagrangian-mean flow". In: *J. Fluid Mech.* 89.4, pp. 609–646. DOI: 10.1017/S0022112078002773.

Barber, N. F. et al. (1948). "The generation and propagation of ocean waves and swell. I. Wave periods and velocities". In: *Phil. Transac. Roy. Soc. London A* 240.824, pp. 527–560. DOI: 10.1098/rsta.1948.0005. eprint: https://royalsocietypublishing.org/doi/pdf/10.1098/rsta.1948.0005.

Breivik, Ø, J-R. Bidlot, et al. (2016). "A Stokes drift approximation based on the Phillips spectrum". In: *Ocean Modelling* 100, pp. 49–56. ISSN: 1463-5003. DOI: https://doi.org/10.1016/j.ocemod.2016.01.005.

Breivik, Ø, P. Janssen, et al. (2014). "Approximate Stokes drift profiles in deep water". In: *J. Phys. Oceanogr.* 44.9, pp. 2433–2445. DOI: 10.1175/JPO-D-14-0020.1.

Breivik, Ø, K. Mogensen, et al. (2015). "Surface wave effects in the NEMO ocean model: Forced and coupled experiments". In: *J. Geophys. Res.: Oceans* 120.4, pp. 2973–2992. DOI: 10.1002/2014JC010565.

Bühler, O. (2014). *Waves and Mean Flows*. 2nd. Cambridge University Press, Cambridge, UK.

Bühler, O. and M. Holmes-Cerfon (2009). "Particle dispersion by random waves in rotating shallow water". In: *J. Fluid Mech.* 638, pp. 5–26. DOI: 10.1017/S0022112009991091.

Calvert, R. et al. (2019). "Laboratory study of the wave-induced mean flow and set-down in unidirectional surface gravity wave packets on finite water depth". In: *Phys. Rev. Fluids* 4 (11), p. 114801. DOI: 10.1103/PhysRevFluids.4.114801.

Christensen, K. H. and E. Terrile (2009). "Drift and deformation of oil slicks due to surface waves". In: *J. Fluid Mech.* 620, pp. 313–332. DOI: 10.1017/S0022112008004606.

Cózar, A. et al. (2014). "Plastic debris in the open ocean". In: *Science* 111.28, pp. 10239–10244. DOI: 10.1073/pnas.1314705111.

Craik, A. D. D. and S. Leibovich (1976). "A rational model for Langmuir circulations". In: *J. Fluid Mech.* 73.3, pp. 401–426. DOI: 10.1017/S0022112076001420.

Davey, A. and K. Stewartson (1974). "On three-dimensional packets of surface waves". In: *Proc. Roy. Soc. A* 338.1613, pp. 101–110. ISSN: 0080-4630. DOI: 10.1098/rspa.1974.0076.

Delandmeter, P. and E. van Sebille (2019). "The Parcels v2.0 Lagrangian framework: new field interpolation schemes". In: *Geosci. Model Dev.* 12.8, pp. 3571–3584. DOI: 10.5194/gmd-12-3571-2019.

Dobler, D. et al. (2019). "Large impact of Stokes drift on the fate of surface floating debris in the South Indian Basin". In: *Marine Pollution Bulletin* 148, pp. 202–209. ISSN: 0025-326X. DOI: doi.org/10.1016/j.marpolbul.2019.07.057.

Drennan, W. M. et al. (2005). "Parameterizing the Sea Surface Roughness". In: *J. Phys. Oceanogr.* 35.5, pp. 835–848. ISSN: 0022-3670. DOI: 10.1175/JPO2704.1.

Drivdal, M. et al. (2014). "Wave-induced mixing and transport of buoyant particles: application to the Statfjord A oil spill". In: *Ocean Science* 10.6, pp. 977–991. DOI: 10.5194/os-10-977-2014.

Dysthe, K. B. (1979). "Note on a modification to the nonlinear Schrödinger equation for application to deep water waves". In: *Proc. Roy. Soc. London A* 369.1736, pp. 105–114. DOI: 10.1098/rspa.1979.0154.

Ekman, V. W. (1905). "On the influence of the Earth's rotation on ocean-currents". In: *Ark. Mat. Astron. Fys.* 2.11, pp. 1–53.

Elgar, S. and R. T. Guza (1985). "Shoaling gravity waves: comparisons between field observations, linear theory, and a nonlinear model". In: *J. Fluid Mech.* 158, pp. 47–70. DOI: 10.1017/S0022112085002543.

Eriksen, M. et al. (2014). "Plastic pollution in the world's oceans: More than 5 trillion plastic pieces weighing over 250,000 tons afloat at sea". In: *PLoS ONE* 9.12, e111913. DOI: 10.1371/journal.pone.0111913.

Ewans, K. (2002). "Directional spreading in ocean swell". In: *Fourth International Symposium on Ocean Wave Analysis and Measurement*, pp. 517–529. ISBN: 978-0-7844-0604-5. DOI: 10.1061/40604(273)54.

Ewans, K. et al. (2006). "Estimation of wind-sea and swell components in a bimodal sea state". In: *J. Offshore Mech. Arctic Eng.-transac. ASME* 128. DOI: 10.1115/1.2166655.

Fraser, C. et al. (2018). "Antarctica's ecological isolation will be broken by storm-driven dispersal and warming". In: *Nature Climate Change* 8.8. DOI: 10.1038/s41558-018-0209-7.

Gemmrich, J. et al. (2016). "Spatial characteristics of ocean waves". In: *Ocean Dynamics* 66. DOI: DO-10.1007/s10236-016-0967-6.

Gerkema, T. and V. I. Shrira (2005). "Near-inertial waves on the 'nontraditional' β plane". In: *J. Geophys. Res.* 110.C1. DOI: 10.1029/2004JC002519.

Gerkema, T., J. T. F. Zimmerman, et al. (2008). "Geophysical and astrophysical fluid dynamics beyond the traditional approximation". In: *Reviews of Geophys.* 46.2. DOI: 10.1029/2006RG000220.

Geyer, R. et al. (2017). "Production, use, and fate of all plastics ever made". In: *Sci. Adv.* 3.7, e1700782. DOI: 10.1126/sciadv.1700782.

Gjevik, B. et al. (1988). "Long period swell wave events on the Norwegian Shelf". In: *J. Phys. Oceanogr.* 18.5, pp. 724–737. ISSN: 0022-3670. DOI: 10.1175/1520-0485(1988)018<0724:LPSWEO>2.0.CO;2.

Goldstein, M. C. et al. (2012). "Increased oceanic microplastic debris enhances oviposition in an endemic pelagic insect". In: *Biol. Lett.* 8, pp. 817–20. DOI: 10.1098/rsbl.2012.0298.

Groeneweg, J. and G. Klopman (1998). "Changes of the mean velocity profiles in the combined wave–current motion described in a GLM formulation". In: *J. Fluid Mech.* 370, pp. 271–296. DOI: 10.1017/S0022112098002018.

Grue, J. and J. Kolaas (2017). "Experimental particle paths and drift velocity in steep waves at finite water depth". In: *J. Fluid Mech.* 810, R1. DOI: 10.1017/jfm.2016.726.

Haney, S. and W. R. Young (2017). "Radiation of internal waves from groups of surface gravity waves". In: *J. Fluid Mech.* 829, pp. 280–303. DOI: 10.1017/jfm.2017.536.

Hasselmann, K. (1970). "Wave-driven inertial oscillations". In: *Geophys. Fluid Dyn.* 1, pp. 463–502. DOI: 10.1080/03091927009365783.

Herbers, T. H. C. and T. Janssen (2016). "Lagrangian surface wave motion and Stokes drift fluctuations". In: *J. Phys. Oceanogr.* 46.4, pp. 1009–1021. DOI: 10.1175/JPO-D-15-0129.1.

Herterich, K. and K. Hasselmann (1982). "The horizontal diffusion of tracers by surface waves". In: *J. Phys. Oceanogr.* 12.7, pp. 704–711. DOI: 10.1175/1520-0485(1982)012<0704:THDOTB>2.0.CO;2.

Higgins, C., T. S. van den Bremer, et al. (2020). "Lagrangian transport by deep-water surface gravity wavepackets: effects of directional spreading and stratification". In: *J. Fluid Mech.* 883, A42. DOI: 10.1017/jfm.2019.877.

Higgins, C., J. Vanneste, et al. (2020). "Unsteady Ekman–Stokes dynamics: implications for surface-wave induced drift of floating marine litter". In: *Geophys. Res. Letters* 47.18, e2020GL089189. DOI: 10.1029/2020GL089189. URL: https://agupubs.onlinelibrary.wiley.com/doi/abs/10.1029/2020GL089189.

Huang, N. E. (1970). "Mass transport induced by wave motion". In: *J. Mar. Res.* 28.1, pp. 35–50.

— (1979). "On surface drift currents in the ocean". In: *J. Fluid Mech.* 91.1, pp. 191–208. DOI: 10.1017/S0022112079000112.

Iwasaki, S. et al. (2017). "Fate of microplastics and mesoplastics carried by surface currents and wind waves: A numerical model approach in the Sea of Japan". In: *Marine Pollution Bulletin* 121.1, pp. 85–96. ISSN: 0025-326X. DOI: doi.org/10.1016/j.marpolbul.2017.05.057.

Jambeck, J. R. et al. (2015). "Plastic waste inputs from land into the ocean". In: *Science* 347.6223, pp. 768–771. DOI: 10.1126/science.1260352.

Jones, C. E. et al. (2016). "Measurement and modelling of oil slick transport". In: *J. Geophys. Res.* 121.10, pp. 7759–7775. DOI: 10.1002/2016JC012113.

Kafiabad, H. A. et al. (2019). "Diffusion of inertia-gravity waves by geostrophic turbulence". In: *J. Fluid Mech.* 869, R7. DOI: 10.1017/jfm.2019.300.

Kenyon, K. E. (1969). "Stokes drift for random gravity waves". In: *J. Geophys. Res.* 74.28, pp. 6991–6994. DOI: 10.1029/JC074i028p06991.

Kinsman, B. (2002). *Wind Waves: Their Generation and Propagation on the Ocean Surface*. Dover. N.Y. ISBN: 9780486495118.

Lavender Law, K. (2017). "Plastics in the marine environment". In: *Annu. Rev. Mar. Sci.* 9, pp. 205–229. DOI: 10.1146/annurev-marine-010816-060409.

Laxague, N. J. M. et al. (2018). "Observations of near-surface current shear help describe oceanic oil and plastic transport". In: *Geophys. Res. Lett.* 45.1, pp. 245–249. DOI: 10.1002/2017GL075891.

Lebreton, L., M. Egger, et al. (2019). "A global mass budget for positively buoyant macroplastic debris in the ocean". In: *Sci. Rep.* 9, p. 12922. DOI: 10.1038/s41598-019-49413-5.

Lebreton, L., S. D. Greer, et al. (2012). "Numerical modelling of floating debris in the world's oceans". In: *Marine Pollution Bulletin* 64.3, pp. 653–661. ISSN: 0025-326X. DOI: https://doi.org/10.1016/j.marpolbul.2011.10.027.

Lebreton, L., B. Slat, et al. (2018). "Evidence that the Great Pacific Garbage Patch is rapidly accumulating plastic". In: *Scientific Reports* 8, p. 4666.

Lewis, D. M. and S. E. Belcher (2004). "Time-dependent, coupled, Ekman boundary layer solutions incorporating Stokes drift". In: *Dynam. Atmosph. and Oceans* 37.4, pp. 313–351. ISSN: 0377-0265. DOI: doi.org/10.1016/j.dynatmoce.2003.11.001.

Longuet-Higgins, M. S. (1953). "Mass transport in water waves". In: *Phil. Trans. Roy. Soc. London A* 245.903, pp. 535–581. ISSN: 0080-4614. DOI: 10.1098/rsta.1953.0006.

— (1984). "Statistical properties of wave groups in a random sea state". In: *Phil. Trans. Roy. Soc. London A* 312.1521, pp. 219–250. ISSN: 0080-4614. DOI: 10.1098/rsta.1984.0061.

Longuet-Higgins, M. S. and R. W. Stewart (1962). "Radiation stress and mass transport in gravity waves, with application to 'surf beats'". In: *J. Fluid Mech.* 13.4, pp. 481–504. DOI: 10.1017/S0022112062000877.

Lucas, C. and C. Guedes Soares (2015). "On the modelling of swell spectra". In: *Ocean Engineering* 108, pp. 749–759. ISSN: 0029-8018. DOI: https://doi.org/10.1016/j.oceaneng.2015.08.017.

Madsen, O. S. (1977). "A realistic model of the wind-induced Ekman boundary layer". In: *J. Phys. Oceanogr.* 7.2, pp. 248–255. DOI: 10.1175/1520-0485(1977)007<0248:ARMOTW>2.0.CO;2.

— (1978). "Mass transport in deep-water waves". In: *J. Phys. Oceanogr.* 8.6, pp. 1009–1015. DOI: 10.1175/1520-0485(1978)008<1009:MTIDWW>2.0.CO;2.

McAllister, M. L. et al. (2018). "The set-down and set-up of directionally spread and crossing surface gravity wave groups". In: *J. Fluid Mech.* 835, pp. 131–169. DOI: 10.1017/jfm.2017.774.

McIntyre, M. E. (1980). "An introduction to the generalized Lagrangian-mean description of wave, mean-flow interaction". In: *Pure Appl. Geophys.* 118.1, pp. 152–176. ISSN: 1420-9136. DOI: 10.1007/BF01586449.

— (1981). "On the 'wave momentum' myth". In: *J. Fluid Mech.* 106, pp. 331–347. DOI: 10.1017/S0022112081001626.

McWilliams, J. C. and B. Fox-Kemper (2013). "Oceanic wave-balanced surface fronts and filaments". In: *J. Fluid Mech.* 730, pp. 464–490. DOI: 10.1017/jfm.2013.348.

McWilliams, J. C. and J. M. Restrepo (1999). "The wave-driven ocean circulation". In: *J. Phys. Oceanogr.* 29.10, pp. 2523–2540. DOI: 10.1175/1520-0485(1999)029<2523:TWDOC>2.0.CO;2.

Mellor, G. and A. Blumberg (2004). "Wave breaking and ocean surface layer thermal response". In: *J. Phys. Oceanog.* 34.3, pp. 693–698. DOI: 10.1175/2517.1.

Olbers, D. and C. Eden (2016). "Revisiting the generation of internal waves by resonant interaction with surface waves". In: *J. Phys. Oceanogr.* 46.8, pp. 2335–2350. DOI: 10.1175/JPO-D-15-0064.1.

Onink, V. et al. (2019). "The role of Ekman currents, geostrophy, and Stokes drift in the accumulation of floating microplastic". In: *J. Geophys. Res.: Oceans* 124.3, pp. 1474–1490. DOI: 10.1029/2018JC014547.

Ostle, C. et al. (2019). "The rise in ocean plastics evidenced from a 60-year time series". In: *Nat. Commun.* 10, p. 1622. DOI: 10.1038/s41467-019-09506-1.

Phillips, O. M. (1977). *The dynamics of the upper ocean*. Cambridge University Press.

Pollard, R. T. (1970). "Surface waves with rotation: An exact solution". In: *J. Geophys. Res.* 75.30, pp. 5895–5898. ISSN: 2156-2202. DOI: 10.1029/JC075i030p05895.

Polton, J. A. et al. (2005). "The role of wave-induced Coriolis-Stokes forcing on the wind-driven mixed layer". In: *J. Phys. Oceanogr.* 35.4, pp. 444–457. DOI: 10.1175/JPO2701.1.

Price, J. F. and M. A. Sundermeyer (1999). "Stratified Ekman layers". In: *J. Geophys. Res.: Oceans* 104.C9, pp. 20467–20494. DOI: 10.1029/1999JC900164.

Rayleigh (1883). "The form of standing waves on the surface of running water". In: *Proc. London Math. Soc.* s1-15.1, pp. 69–78. DOI: 10.1112/plms/s1-15.1.69.

Reisser, J. et al. (2015). "The vertical distribution of buoyant plastics at sea: an observational study in the North Atlantic Gyre". In: *Biogeosciences* 12.4, pp. 1249–1256. DOI: 10.5194/bg-12-1249-2015.

Röhrs, J. et al. (2012). "Observation-based evaluation of surface wave effects on currents and trajectory forecasts". In: *Ocean Dynamics* 62.10, pp. 1519–1533. ISSN: 1616-7228. DOI: 10.1007/s10236-012-0576-y.

Seshasayanan, K. and B. Gallet (2019). "Surface gravity waves propagating in a rotating frame: The Ekman-Stokes instability". In: *Phys. Rev. Fluids*.

Shrira, V. I. and R. B. Almelah (2020). "Upper-ocean Ekman current dynamics: a new perspective". In: *J. Fluid Mech.* 887, A24. DOI: 10.1017/jfm.2019.1059.

Steer, J. N. et al. (2020). "Experimental study of dispersion and modulational instability of surface gravity waves on constant vorticity currents". In: *J. Fluid Mech.* 884, A40. DOI: 10.1017/jfm.2019.951.

Stokes, G.G. (1847). "On the theory of oscillatory waves". In: *Trans. Cam. Phil. Soc.* 8, pp. 441–455.

Suzuki, N. and B. Fox-Kemper (2016). "Understanding Stokes forces in the wave-averaged equations". In: *J. Geophys. Res.: Oceans* 121.5, pp. 3579–3596. DOI: 10.1002/2015JC011566.

Taklo, T. M. A. et al. (2017). "On dispersion of directional surface gravity waves". In: *J. Fluid Mech.* 812, pp. 681–697. DOI: 10.1017/jfm.2016.817.

The WAMDI Group (1988). "The WAM model-a third generation ocean wave prediction model". In: *J. Phys. Oceanogr.* 18.12, pp. 1775–1810. ISSN: 0022-3670. DOI: 10.1175/1520-0485(1988)018<1775:TWMTGO>2.0.CO;2.

Thomas, J. et al. (2018). "Wave-induced mean flows in rotating shallow water with uniform potential vorticity". In: *J. Fluid Mech.* 839, pp. 408–429. DOI: 10.1017/jfm.2018.22.

Toffoli, A. and E. M. Bitner-Gregersen (2017). "Types of ocean surface waves, wave classification". In: *Encyclopedia of Maritime and Offshore Engineering*. John Wiley & Sons, Ltd., pp. 1–8. ISBN: 9781118476406. DOI: 10.1002/9781118476406.emoe077.

Tolman, H. L. (2009). "User manual and system documentation of WAVEWATCH III TM version 3.14 Technical Note". In:

Trinanes, Joaquin A. et al. (2016). "Analysis of flight MH370 potential debris trajectories using ocean observations and numerical model results". In: *J. Operational Oceanog.* 9.2, pp. 126–138. DOI: 10.1080/1755876X.2016.1248149.

Ünlüata, Ü. and C. C. Mei (1970). "Mass transport in water waves". In: *J. Geophy. Res.* 75.36, pp. 7611–7618. DOI: 10.1029/JC075i036p07611.

Ursell, F. (1950). "On the theoretical form of ocean swell on a rotating earth". In: *Mon. Not. Roy. Astron. Soc., Geophys. Suppl.* 6.s1, pp. 1–8. DOI: 10.1111/j.1365-246X.1950.tb02968.x.

van den Bremer, T. S. and Ø Breivik (2017). "Stokes drift". In: *Phil. Trans. Roy. Soc. London A* 376.2111. ISSN: 1364-503X. DOI: 10.1098/rsta.2017.0104.

van den Bremer, T. S. and P. H. Taylor (2015). "Estimates of Lagrangian transport by surface gravity wave groups: The effects of finite depth and directionality". In: *J. Geophys. Res.* 120.4, pp. 2701–2722. DOI: 10.1002/2015JC010712.

— (2016). "Lagrangian transport for two-dimensional deep-water surface gravity wave groups". In: *Proc. Roy. Soc. London A* 472.2192. ISSN: 1364-5021. DOI: 10.1098/rspa.2016.0159.

van den Bremer, T. S., C. Whittaker, et al. (2019). "Experimental study of particle trajectories below deep-water surface gravity wave groups". In: *J.Fluid Mech.* 879, pp. 168–186. DOI: 10.1017/jfm.2019.584.

van Sebille, E., S. Aliani, et al. (2020). "The physical oceanography of the transport of floating marine debris". In: *Environ. Res. Lett.* 15.2, p. 023003. DOI: 10.1088/1748-9326/ab6d7d.

van Sebille, E., C. Wilcox, et al. (2015). "A global inventory of small floating plastic debris". In: *Environ. Res. Lett.* 10.12, p. 124006. DOI: 10.1088/1748-9326/10/12/124006.

Webb, A. and B. Fox-Kemper (2011). "Wave spectral moments and Stokes drift estimation". In: *Ocean Modelling* 40.3, pp. 273–288. ISSN: 1463-5003. DOI: doi.org/10.1016/j.ocemod.2011.08.007.

Wilcox, C. et al. (2020). "Abundance of Floating Plastic Particles Is Increasing in the Western North Atlantic Ocean". In: *Envir. Sci. Tech.* 54.2, pp. 790–796. DOI: 10.1021/acs.est.9b04812.

Wu, L. et al. (2019). "Wave effects on coastal upwelling and water level". In: *Ocean Modelling* 140, p. 101405. ISSN: 1463-5003. DOI: https://doi.org/10.1016/j.ocemod.2019.101405.

Xu, Z. and A. J. Bowen (1994). "Wave- and wind-driven flow in water of finite depth". In: *J. Phys. Oceanogr.* 24.9, pp. 1850–1866. DOI: 10.1175/1520-0485(1994)024<1850:WAWDFI>2.0.CO;2.